

ADVANCED NUMERICAL MODELING of FIBER-REINFORCED  
ELASTOMERIC ISOLATORS (FREIs)

ADVANCED NUMERICAL MODELING of FIBER-REINFORCED ELASTOMERIC  
ISOLATORS (FREIs)

By

Peyman Moghimi Osgooei

B.Sc., M.Sc.

A Thesis Submitted to the School of Graduate Studies in Partial Fulfilment of the  
Requirements for the Degree of  
Doctor of Philosophy

McMaster University

© Copyright by Peyman Moghimi Osgooei, December 2014

DOCTOR OF PHILOSOPHY  
(Civil Engineering)

McMaster University  
Hamilton, Ontario, Canada

TITLE: Advanced Numerical Modeling of Fiber- Reinforced  
Elastomeric Isolators (FREIs)

AUTHOR: Peyman Moghimi Osgooei

SUPERVISORS: Dr. Michael J. Tait  
Dr. Dimitrios Konstantinidis

NUMBER OF PAGES: xix, 208

## Abstract

Fiber-reinforced elastomeric isolators (FREIs) are relatively new type of elastomeric bearing that utilize fiber-reinforced polymer (FRP) material for the reinforcing material. FREIs have lower weight and potentially easier manufacturing process compared with conventional seismic isolators. The viability of FREIs has been investigated through a number of experimental tests studies. However, numerical modeling of FREIs is required to better understand their vertical and lateral response characteristics, and to investigate the response of isolated structures using FREIs.

In this research, 3D finite element analysis (FEA) is carried out to investigate the vertical response of FREIs with various numbers of elastomer layers and reinforcing materials. In addition, the lateral response of FREIs is studied using 3D FEA. Experimental test results from three previously tested isolators were used to evaluate FEA models and subsequently, a series of FEA were carried out to investigate the sensitivity of the lateral response of FREIs to the direction of loading.

A new computational model is proposed to enhance the time history analysis of structures seismically isolated with FREIs. The proposed Pivot-Elastic model is capable of predicting the complex lateral response of FREIs. In order to evaluate the predictions of the proposed model, nonlinear time history analyses of a two-storey steel moment frame structure seismically isolated with FREIs were carried out, and the predicted response of the structure was compared against the results from a previous shake table study.

The lateral response of rectangular FREIs, a shape suitable for shear wall structures is investigated through experimental testing and 3D FEA. A series of time history analyses, using ten earthquake ground motions are carried out on a two-storey reinforced concrete shear wall structure seismically isolated using rectangular shape FREIs. The efficiency of the isolation system composed of rectangular FREIs was evaluated by investigating the seismic response of the structure with and without the seismic isolation system.

## Acknowledgements

I would like to express my sincere gratitude to my supervisors, Dr. Michael J. Tait and Dr. Dimitrios Konstantinidis for their support, advice, encouragement and guidance during the research. I am also extremely grateful to the members of my supervisory committee, Dr. John Wilson, Dr. Dieter Stolle and Dr. Stephen Tullis for their valuable comments and suggestions throughout my research work. I would like to extend my gratitude to my colleagues for their friendship and support during my time at McMaster University.

Lastly, I would like to thank my parents for their continual love and support. This thesis is dedicated to my wife, Narges.

## Table of Contents

Abstract .....	iii
Acknowledgments .....	iv
Table of Contents .....	v
List of Tables .....	x
List of Figures .....	xii
Co-Authorship .....	xviii
Chapter 1: Overview of Study .....	1
1.2 Seismic Isolation .....	2
1.3 Elastomeric Bearings .....	3
1.4 Fiber-Reinforced Elastomeric Isolators (FREIs) .....	4
1.4.1 Vertical Stiffness .....	5
1.4.2 Lateral Stiffness .....	6
1.4.3 Rectangular FREIs .....	8
1.4.4 FREI Models .....	8
1.5 Research Objectives .....	9
1.6 Organization of the Thesis .....	9
1.7 References .....	11
Chapter 2: Three-Dimensional Finite Element Analysis of Circular Fiber-Reinforced Elastomeric Bearings under Compression .....	18
Abstract .....	18
2.1 Introduction .....	19
2.2 Review of Analytical Solutions .....	23
2.2.1 Pressure Solution ( <i>PS</i> ) .....	23
2.2.2 Pressure Approach ( <i>PA</i> ) .....	26
2.2.2.1 Monotonic Deformation .....	26
2.2.2.2 Rigid Ends .....	27
2.3 Finite Element Analysis .....	30
2.4 Results and Discussion .....	33

2.4.1	Deformed Shapes .....	33
2.4.2	Influence of Applied Vertical Stress .....	34
2.4.3	Vertical Stiffness .....	35
2.4.4	Stress and Strain in Elastomer .....	37
2.4.5	Stress in Reinforcement .....	40
2.5	Conclusion .....	41
2.6	Acknowledgments .....	43
2.7	References .....	43
Chapter 3: Finite Element Analysis of Unbonded Square Fiber-Reinforced		
Elastomeric Isolators (FREIs) under Lateral Loading in Different		
	Directions .....	63
	Abstract .....	63
3.1	Introduction .....	64
3.2	Lateral Response of Unbonded FREIs .....	67
3.3	Unbonded FREIs .....	68
3.4	FE Modeling .....	69
3.5	FE Model Validation .....	70
3.6	Lateral Response in Different Directions .....	72
3.6.1	Deformed Shapes .....	72
3.6.2	Load-Displacement Relationships .....	73
3.6.3	Stress and Strain in Elastomer Layers .....	75
3.6.4	Stress in Fiber Reinforcement Layers .....	78
3.7	Conclusions .....	79
3.8	Acknowledgments .....	82
3.9	References .....	82
Chapter 4: Computational Model for Unbonded Fiber-Reinforced Elastomeric		
	Isolators (U-FREIs) .....	96

Abstract .....	96
4.1 Introduction .....	97
4.2 Modeling U-FREIs .....	100
4.2.1 Bilinear Model .....	100
4.2.2 Bilinear Pivot Model .....	102
4.2.3 Proposed Pivot-Elastic Model .....	102
4.3 U-FREI System .....	103
4.4 Modeling U-FREI using Pivot-Elastic Model .....	104
4.5 Evaluation of the Proposed Pivot-Elastic Model .....	105
4.5.1 Base Isolated Structure .....	105
4.5.2 Nonlinear Dynamic Analyses .....	106
4.6 Results and Discussions .....	107
4.6.1 Evaluation of Model .....	107
4.6.2 Sensitivity of the Response to $K_{\text{eff}}$ and $\beta_{\text{eff}}$ .....	108
4.6.3 Bonded versus Unbonded FREI System .....	111
4.7 Summary and Conclusions .....	113
4.8 Acknowledgements .....	115
4.9 References .....	115
Chapter 5: Experimental and Finite Element Study on the Lateral Response of Modified Rectangular Fiber-Reinforced Elastomeric isolators (MR-FREIs) .....	132
Abstract .....	132
5.1 Introduction .....	132
5.2 Experimental Testing .....	136
5.2.1 Isolator Design .....	136
5.2.2 Experimental Setup and Lateral Test Procedure .....	137
5.2.3 Experimental Results .....	138
5.2.3.1 Effective Lateral Stiffness .....	138
5.2.3.2 Energy Dissipation Characteristics .....	140

5.3	Evaluation of Finite Element Models .....	140
5.4	Effect of Modification Characteristics .....	142
5.4.1	Load-Displacement Relationships .....	143
5.4.2	Stress and Strain in Elastomer Layers .....	144
5.4.3	Deformed Shapes .....	147
5.4.4	Stress in Fiber Reinforcement .....	148
5.5	Conclusions .....	148
5.6	Acknowledgments .....	150
5.7	References .....	151
Chapter 6: Seismic Isolation of a Shear Wall Structure using Rectangular Fiber-		
	Reinforced Elastomeric Isolators (FREIs) .....	169
	Abstract .....	169
6.1	Introduction .....	169
6.2	Rectangular Shape Isolators .....	172
6.3	Shear Wall Structure .....	173
6.4	Seismic Isolation System .....	174
6.5	Modeling U-FREIs .....	176
6.6	Modeling Shear Wall Structure .....	177
6.7	Earthquake Ground Motions .....	178
6.8	Time History Analyses .....	179
6.9	Results and Discussions .....	180
6.10	Summary and Conclusions .....	183
6.11	Acknowledgments .....	184
6.12	References .....	185
Chapter 7: Conclusions and Recommendations .....		
7.1	Summary and Conclusions .....	200
7.1.1	FEA on Vertical Response of FREIs .....	200
7.1.2	FEA on Lateral Response of FREIs .....	202

7.1.3	Computational Model for FREIs .....	203
7.1.4	Experimental and FEA Studies on Rectangular FREIs .....	204
7.1.5	Seismic Isolation of a Shear Wall Building with FREIs .....	204
7.2	Recommendations for Future Study .....	205
7.3	References .....	207

## List of Tables

Table 2.1. Bearing dimensions and properties .....	47
Table 2.2. Vertical stiffness values obtained from FEA and analytical solutions .....	47
Table 2.3. Comparison of $E_c^1/E_c^{\text{mid}}$ and $E_c^2/E_c^{\text{mid}}$ obtained from FEA and the pressure approach .....	48
Table 3.1. Characteristics of the bearings considered in this study .....	87
Table 3.2. Normalized displacement values $D_r$ , $D_c$ , $D_h$ and $D_f$ for the bearings loaded at $0^\circ$ .....	87
Table 3.3. Effective lateral stiffness in different loading directions .....	87
Table 4.1. Equivalent linear properties of the U-FREIs obtained from cyclic tests .....	120
Table 4.2. Parameters of the Pivot-Elastic model .....	120
Table 4.3. Effective stiffness and damping ratio values corresponding to the model ...	120
Table 4.4. Comparison of peak response quantities predicted by different models. Quantities are expressed as ratios of predicted-to-experimentally measured value .....	121
Table 4.5. Parameters of the Pivot-Elastic model considering the change in values of effective stiffness and effective damping ratio of the FREIs .....	121
Table 4.6. Normalized peak response values of the isolated structure for different cases .....	121
Table 4.7. Parameters of the Pivot-Elastic model for the bonded FREI .....	122
Table 4.8. Predicted properties for the bonded FREI .....	122
Table 4.9. Peak response values of the isolated structure considering bonded FREIs normalized with respect to the corresponding peak response values for the U-FREIS .....	122
Table 5.1. Specimen geometric characteristics .....	156
Table 5.2. Material constants for the third-order hyperelastic model (in MPa) .....	156
Table 5.3. MR-FREI geometric characteristics .....	156
Table 6.1. Effective stiffness and damping ratio of the rectangular FREIs .....	188
Table 6.2. Energy dissipation of FREIs along the $x$ and $y$ directions .....	188

Table 6.3. Parameters of the Pivot-Elastic model .....	188
Table 6.4. The ratio of the predicted response values of the FREIs using Pivot- Elastic model over the experimentally observed values .....	189
Table 6.5. The selected ground motions .....	189
Table 6.6. Summary of peak response values for the FB and BI structures .....	190

## List of Figures

Figure 1.1. Schematic view of the deformation of a structure without (a) and with (b) seismic isolation .....	16
Figure 1.2. Reduction in seismic acceleration at larger period and damping [3] .....	16
Figure 1.3. A typical SREI .....	16
Figure 1.4. Schematic deformed shapes of a (a) SREI and a (b) FREI [8] under lateral loading .....	17
Figure 1.5. A typical load-displacement relationship of FREIs obtained from cyclic testing .....	17
Figure 2.1. A circular elastomeric pad bonded to flexible reinforcements .....	49
Figure 2.2. Bearing consisting of $n$ elastic layers bonded to rigid supports .....	49
Figure 2.3. Effect of element size on the modeling error in B5-10 bearing .....	50
Figure 2.4. Deformed shape of bearing B5-10 under $\bar{p} = 2$ MPa .....	50
Figure 2.5. Deformed shapes of bearings with $K_f = 100$ kN/mm under $\bar{p} = 2$ MPa .....	51
Figure 2.6. Comparison of the deformed shapes of the first and center elastomer layers at $r/b = 1/2$ and $r/b = 5/6$ obtained from FE analysis, PA considering rigid end effects and PS under $\bar{p} = 2$ MPa .....	52
Figure 2.7. Variation of $E_c/E$ obtained from FE analysis at different load levels in bearings .....	53
Figure 2.8. $E_c/E$ as a function of $K_f/Et$ , as computed using the PA including rigid end effects and FEA .....	53
Figure 2.9. Contours of normalized $\sigma_{rr}$ stress in bearings with $K_f = 10$ kN/mm under $\bar{p} = 2$ MPa .....	54
Figure 2.10. Contours of normalized $\sigma_{rr}$ stress in bearings with $K_f = 500$ kN/mm under $\bar{p} = 2$ MPa .....	54
Figure 2.11. Variation of the normalized strains through the elastomer layers obtained from FEA at $r/b = 0$ .....	55
Figure 2.12. Variation of the normalized strains through the elastomer layers obtained from FEA at $r/b = 1/2$ .....	55

Figure 2.13. Variation of the normalized strains through the elastomer layers obtained from FEA at $r/b = 5/6$ .....	56
Figure 2.14. Variation of normalized average pressure ( $p_{ave}/\bar{p}$ ) in the centre elastomer layers obtained from FEA results .....	57
Figure 2.15. Comparison of normalized average pressure ( $p_{ave}/\bar{p}$ ) in the centre elastomer layers for bearings with $K_f = 100$ kN/mm obtained from FEA, PS and PA considering rigid end effects .....	57
Figure 2.16. Variation of normalized shear strains ( $\gamma_{rz}E/\bar{p}$ ) in the first and center elastomer layers obtained from FEA, PS and PA considering rigid end effects for bearings with $S = 5$ .....	58
Figure 2.17. Variation of normalized shear strains ( $\gamma_{rz}E/\bar{p}$ ) in the first and center elastomer layers obtained from FEA, PS and PA considering rigid end effects for bearings with $S = 30$ .....	59
Figure 2.18. Variation of normalized $\sigma_{rr}$ stress in center reinforcement layers obtained from FEA .....	60
Figure 2.19. Variation of normalized $\sigma_{\theta\theta}$ stress in center reinforcement layers obtained from FEA .....	61
Figure 2.20. Comparison of normalized $\sigma_{rr}$ and $\sigma_{\theta\theta}$ in center reinforcement layers obtained from FEA, PS and PA considering rigid end effects .....	62
Figure 3.1. Directions of lateral loading investigated in this study (shown on bearing B200X68) .....	88
Figure 3.2. Typical lateral load-displacement of a FREI bearing loaded in the $0^\circ$ direction .....	88
Figure 3.3. Finite element model of bearing B200X78 .....	88
Figure 3.4. Lateral load-displacement relationships of the bearings obtained from FEA and test results .....	89
Figure 3.5. Deformed shapes of bearing B200X78 at $0^\circ$ , obtained from FEA results .....	89
Figure 3.6. Deformed shapes of bearing B200X78 at $15^\circ$ , obtained from FEA results ...	89
Figure 3.7. Deformed shapes of bearing B200X78 at $30^\circ$ , obtained from FEA results ...	90

Figure 3.8. Deformed shapes of bearing B200X78 at 45°, obtained from FEA results ...	90
Figure 3.9. Lateral load-displacement curves of the bearings at different loading orientations obtained from FEA results .....	91
Figure 3.10. Local stresses in the undeformed configuration (left) and deformed configuration (right) .....	91
Figure 3.11. Contours of normalized $S_{11}$ stress in bearing B200X68 for the four different loading directions .....	92
Figure 3.12. Definition of A-A and B-B section lines in bearing B200X78 .....	92
Figure 3.13. Variation of normalized stress profiles along the width of the bearings at 0° and 45° .....	93
Figure 3.14. Contours of shear strain $\epsilon_{13}$ in bearings B200X68 and B200X105 loaded at 0° and 45° .....	94
Figure 3.15. Variation of normalized in-plane stresses in center fiber reinforcement layers along section line B-B in the bearings .....	95
Figure 4.1. Bilinear model .....	123
Figure 4.2. Pivot hysteresis models: (a) the general case, (b) the simplified bilinear Pivot case .....	123
Figure 4.3. Definition of the Pivot-Elastic model .....	124
Figure 4.4. Time history of the input lateral displacement in the cyclic testing on U-FREIs .....	124
Figure 4.5. Comparison of the unscrapped response of the FREIs with the prediction of the model .....	125
Figure 4.6. Schematic view of the base isolated structure considered in the shake table tests (all dimensions in mm) .....	125
Figure 4.7. Acceleration time histories (left) and acceleration response spectra (right) of the MCE-level ground motions .....	126
Figure 4.8. Comparison of the isolation displacement time histories obtained from shake table tests and time history analyses .....	127

Figure 4.9. Comparison of the response histories of superstructure base shear obtained from shake table tests and the time history analyses for MCE-level ground motions .....	128
Figure 4.10. Comparison of the hysteresis loops of the U-FREIs obtained from shake table and time history analyses for MCE-level ground motions .....	129
Figure 4.11. Normalized spectral displacement of Imperial Valley-MCE and Tabas-MCE earthquake motions for 10% damping .....	130
Figure 4.12. Force-displacement relationship of bonded FREI vs U-FREI .....	130
Figure 4.13. Comparison of the hysteresis loops of bonded FREIs and U-FREIs obtained from time history analyses for the MCE-level ground motions ..	131
Figure 5.1. Isolation system under a masonry wall using (a) square isolators and (b) rectangular (strip) isolators .....	157
Figure 5.2. Plan view of the specimens .....	157
Figure 5.3. Schematic of the test apparatus .....	158
Figure 5.4. Experimental hysteresis loops for the isolators .....	159
Figure 5.5. Comparison of the first cycle at $u/t_r = 2.50$ from specimen C1 and respective modified specimens .....	160
Figure 5.6. First cycle effective stiffness of the modified specimens normalized by the effective stiffness of the control specimen (C1) .....	161
Figure 5.7. First cycle energy dissipation of the modified specimens normalized by the energy dissipation of the control specimen (C1) .....	161
Figure 5.8. FE model of isolator C2-46I .....	162
Figure 5.9. Comparison of the lateral load-displacement relationships of isolators obtained from FEA with experimental test results .....	162
Figure 5.10. Lateral load-displacement relationships of isolators with exterior modification .....	163
Figure 5.11. Lateral load-displacement relationships of isolators with interior modification .....	163

Figure 5.12. Lateral load-displacement relationships of selected isolators with modifications .....	164
Figure 5.13. Local stresses in the undeformed (left) and deformed configuration (right) .....	164
Figure 5.14. Contours of $S_{11}$ in the center elastomer layer under pure compression ....	165
Figure 5.15. Contours of $S_{11}$ in the center elastomer layer at $u/t_r = 1.00$ .....	165
Figure 5.16. Contours of $S_{11}$ in the center elastomer layer at $u/t_r = 1.75$ .....	166
Figure 5.17. Variation of normalized stress profiles in the center elastomer layer along $x = 0$ and $y = 0$ in the unmodified isolator and isolators 58I and 58E .....	166
Figure 5.18. Contours of shear strain $\gamma_{13}$ under pure compression, $u/t_r = 1.00$ and $1.75$ .....	167
Figure 5.19. Distribution of $S_{11}$ in the center fiber reinforcement layer in isolators modified with interior modifications along $y = 0$ (top) and $x = 0$ (bottom) .....	167
Figure 5.20. Distribution of $S_{11}$ in the center fiber reinforcement layer in isolators modified with exterior modifications along $y = 0$ (top) and $x = 0$ (bottom) .....	168
Figure 6.1. Schematic view of seismic isolation of a (a) frame structure; (b) masonry structure using circular/square isolators and (c) masonry structure using rectangular strip isolators .....	191
Figure 6.2. Schematic deformed shapes of a rectangular FREI along its longer (left) and shorter (right) directions .....	191
Figure 6.3. Plan and elevation views of the shear wall structure (all dimensions shown are in mm) .....	192
Figure 6.4. Reinforcement detailing of shear walls .....	192
Figure 6.5. Distribution of the isolators under shear walls .....	193
Figure 6.6. Lateral hysteresis loops of the rectangular FREI along (a) x-axis and (b) y-axis .....	193

Figure 6.7. Definition of the Pivot-Elastic model .....	194
Figure 6.8. Comparison of the experimentally obtained response of the FREIs with the prediction of the Pivot-Elastic model along the (a) x-axis and (b) y-axis .....	194
Figure 6.9. Multilayer shell elements .....	195
Figure 6.10. Stress-strain relationship of concrete and reinforcement .....	195
Figure 6.11. Acceleration response spectrum of the selected ground motions at 5% damping .....	196
Figure 6.12. Comparison of the mean acceleration response spectrum of the selected ground motions with the design spectrum .....	196
Figure 6.13. First two modes with highest MPR along the direction of ground motions .....	197
Figure 6.14. Comparison of the mean values of the peak floor accelerations over PGA .....	197
Figure 6.15. Comparison of the mean values of the peak story shear in the FB and BI structures .....	198
Figure 6.16. Comparison of the mean values of the normalized peak overturning moment in the FB and BI structures .....	198
Figure 6.17. Comparison of the mean values of inter-story drift ratios (IDR) in the FB and BI structures .....	198
Figure 6.18. Mean floor spectra for the SLE, DBE and MCE hazard levels .....	199
Figure 6.19. Peak isolation displacement obtained at each ground motion .....	199

## Co-Authorship

This thesis has been prepared in accordance with the regulations for a “sandwich” thesis format as stipulated by the School of Graduate Studies at McMaster University. The thesis has been co-authored as:

### **Chapter 2: Three-Dimensional Finite Element Analysis of Circular Fiber-Reinforced Elastomeric Bearings under Compression**

**Authors: P. M. Osgooei, M. J. Tait, and D. Konstantinidis**

The finite element analyses were carried out by P. M. Osgooei under the supervision of Dr. M. J. Tait and Dr. D. Konstantinidis. The paper was written by P. M. Osgooei and modifications were done under the supervision of Dr. M. J. Tait and Dr. D. Konstantinidis. This chapter has been published in Composite Structures.

### **Chapter 3: Finite Element Analysis of Unbonded Square Fiber-Reinforced Elastomeric Isolators (FREIs) under Lateral Loading in Different Directions.**

**Authors: P. M. Osgooei, M. J. Tait, and D. Konstantinidis**

The finite element analyses were carried out by P. M. Osgooei under the supervision of Dr. M. J. Tait and Dr. D. Konstantinidis. The paper was written by P. M. Osgooei and modifications were done under the supervision of Dr. M. J. Tait and Dr. D. Konstantinidis. This chapter has been published in Composite Structures.

### **Chapter 4: Computational Model for Unbonded Fiber-Reinforced Elastomeric Isolators (U-FREIs)**

**Authors: P. M. Osgooei, M. J. Tait, and D. Konstantinidis**

The Pivot-Elastic model was developed by P. M. Osgooei under the supervision of Dr. M. J. Tait and Dr. D. Konstantinidis. The paper was written by P. M. Osgooei and modifications were done under the supervision of Dr. M. J. Tait and Dr. D. Konstantinidis. This chapter has been submitted for publication in the Earthquake Engineering and Structural Dynamics.

**Chapter 5: Experimental and Finite Element Study on the Lateral Response of Modified Rectangular Fiber-Reinforced Elastomeric Isolators (MR-FREIs)**

**Authors: P. M. Osgooei, N. C. Van-Engelen, D. Konstantinidis, and M. J. Tait**

Experimental testing was conducted by N. C. Van-Engelen. Development and evaluation of the finite element models and the parametric study using finite element were conducted by P. M. Osgooei. The paper was written by P. M. Osgooei and modifications were done under the supervision of Dr. M. J. Tait and Dr. D. Konstantinidis in with consultation with N. C. Van-Engelen. This chapter has been submitted for publication in Engineering Structures.

**Chapter 6: Seismic Isolation of a Shear Wall Structure using Rectangular Fiber-Reinforced Elastomeric Isolators (FREIs)**

**Authors: P. M. Osgooei, M. J. Tait, and D. Konstantinidis**

The nonlinear time history analyses were carried out P. M. Osgooei under the supervision of Dr. M. J. Tait and Dr. D. Konstantinidis. This paper was written by P. M. Osgooei and modifications were done under the supervision of Dr. M. J. Tait and Dr. D. Konstantinidis. This paper will be submitted for publication.

## **Chapter 1: Overview of Study**

### **1.1 Background**

The objective of conventional seismic design is to avoid structural collapse and loss of life during large earthquake ground motions. A structure designed according to such life safety provisions might not be functional after a severe earthquake event due to structural and non-structural damage and large residual displacements. A higher level of performance is considered for high importance structures such as hospitals, emergency centers and fire stations as it is critical that they remain functional after a seismic event. The high economic losses observed from severe earthquake events in developed countries have persuaded both designers and building owners to consider higher levels of structural performance.

In the past 50 years, a large amount of research has been carried out on new earthquake-resistant systems that provide higher performance levels while having reasonable construction costs [1]. The new systems are known as structural control systems, and similar to conventional seismic design, most of them are designed to dissipate the earthquake input energy, by providing additional damping mechanisms using special devices known as dampers [1]. The structural control systems are divided into passive, semi-active and active systems [2]. In most of these systems, one or more devices, designed to modify the stiffness and/or increase the damping of the structure, are attached or embedded into the structure. In contrast to active and semi-active system, in passive control systems, the devices installed to improve the seismic response of the

structure do not require external power source. Examples of passive control systems are hysteretic or viscous dampers, tuned mass dampers and seismic isolators.

## **1.2 Seismic Isolation**

Seismic isolation systems aim at uncoupling the horizontal motion of the structure from the ground motion during an earthquake by installing flexible isolator devices underneath the supporting points of the structure. Isolator devices are usually installed between the foundation level and the superstructure. Unlike conventional seismic design or seismic design systems employing dampers (where the main objective is to dissipate the earthquake input energy), in seismic isolation systems the goal is to limit the earthquake energy transferred into the structure. Ideally, if no earthquake input energy is transferred into the structure, the structure remains unaffected during an earthquake event. The first mode of vibration in an isolated structure involves deformation almost entirely at the isolation level, while the superstructure remains almost rigid (Fig. 1.1) [3].

Research on seismic isolation was largely predicated in the middle and late 1970s on the observation that most strong motions recorded up to that date had lower spectral acceleration values (which are related to the forces in the structure) in the long-period range [4]. Consequently, seismic isolation has become an attractive technique to mitigate seismic induced damage. The maximum values of the spectral acceleration for the fixed base (FB) elastic structure are observed in a period range of 0.2 to 0.6 s [1]. With the flexibility provided by the seismic isolation system, the fundamental period of the base isolated (BI) structure shifts to larger values (Fig. 1.2), which results in a reduction in the

forces that must be resisted by the superstructure. Further seismic mitigation can be obtained by utilizing a damping ratio in the isolation system higher than that of the fixed base superstructure.

### **1.3 Elastomeric Bearings**

Seismic isolator devices must be sufficiently stiff in the vertical direction to limit vertical deflections under gravity loads, and flexible in the horizontal direction, in order to provide the isolated structure with a larger period. The concept of seismic isolation has become a practical reality within the last 30 years with the development of multilayer elastomeric bearings. This type of bearing is made by vulcanizing sheets of rubber to thin steel reinforcing plates [5]. Figure 1.3 shows a schematic view of a steel-reinforced elastomeric isolator (SREI, also known as laminated rubber bearings). Rubber materials, known for their low elastic modulus, are employed in SREIs to obtain low lateral stiffness. The steel reinforcing plates allow the rubber to shear freely while increasing the vertical stiffness of the isolator by laterally constraining the rubber layers when subjected to vertical loads. Currently, SREIs are the most common base isolation system in use [5]. Two thick steel end plates are usually bonded to the upper and lower surfaces of SREIs in order to connect the isolator to the superstructure and the substructure. The three main types of SREIs available are low-damped rubber bearings, lead-plug rubber bearings and high-damped rubber bearings [5, 6].

The application of seismic isolation technology in North America is almost entirely limited to large, expensive or historical buildings, or those with sensitive equipment, e.g.

hospitals. The reason for this limitation is primarily due to the cost of manufacturing and installing these devices, as well as specific test requirements in code provisions. For smaller projects like residential buildings, it is currently not economically feasible to use seismic isolation systems. The application of seismic isolation technology could be extended to ordinary importance and residential buildings or to developing countries by reducing the weight and the manufacturing cost of the isolators [7].

The high cost associated with SREIs is primarily due to the highly labour-intensive manufacturing process, which includes cutting, sand-blasting and coating the steel plates and laying-up the steel and rubber layers in a mold for hot vulcanization bonding [7]. The weight of SREIs could be reduced by replacing the steel reinforcing plates with a lower-weight material with the same order of elastic stiffness, e.g., fiber-reinforced polymer (FRP) [7]. In addition, using fiber reinforcing layers instead of steel would simplify the manufacturing process of the isolators [7].

#### **1.4 Fiber-Reinforced Elastomeric Isolators (FREIs)**

FREIs are a new type of laminated rubber bearings that utilize fiber material for the reinforcing layers. Compared with SREIs, FREIs have lower weight and can be manufactured using cold vulcanization. In order to further reduce the weight of FREIs and simplify the manufacturing process, FREIs can be manufactured without the steel end plates. In the absence of steel connecting plates, the isolators can be installed between the superstructure and substructure with no bonding or fastening in an unbonded application. This way, the shear force is transferred through the friction that develops

between the isolator and the support surfaces. FREIs are low-weight, potentially low-cost devices that could be employed for the seismic isolation of ordinary low-rise buildings. In addition, the simpler manufacturing and installation process can extend the application of FREIs to developing countries.

The lateral and vertical response characteristics of FREIs have been investigated through experimental test programs [8-14]. Test results have shown that the required vertical stiffness and horizontal flexibility for a seismic isolation system could be obtained with FREIs. It was observed [11] that the energy dissipation obtained from FREIs is superior compared to SREIs. This increase in the energy dissipation of FREIs is attributed to the internal friction mechanism developed between the rubber and fiber interface as the isolator undergoes lateral displacement.

#### **1.4.1 Vertical Stiffness**

The vertical stiffness of a seismic isolator is of great importance, as it must be large enough to limit the deflections under vertical loads and to suppress the rocking mode of vibration [15]. In the literature, several analytical solutions have been developed to predict the vertical response characteristics of elastomeric bearings. The pressure solution (PS) and the pressure approach (PA) are the two commonly used methods employed to determine closed-form solutions for the vertical stiffness of SREIs [16-17]. These two methods estimate the compressions modulus of an elastomer pad bonded to rigid plates, and are based on a number of simplifying assumptions. The assumptions used in the PS method are as follows: i) The top and bottom surfaces of the elastomer layer remain horizontal under the vertical load; ii) Points on a vertical line before the vertical load is

applied, form a parabola under the load; iii) The normal stresses at any point in the elastomer layer can be approximated by the value of the pressure at that point. The PA method is similar to PS and relies only on the two kinematic assumptions (i and ii). Assuming that the compression modulus of all elastomer layers are equal and is not affected by the end boundary condition (top and bottom plates), the vertical stiffness of the isolators can be calculated based on the compression modulus of one elastomer layer.

Unlike SREIs, where the steel reinforcing layers are usually assumed rigid, the fiber reinforcing layers in FREIs are flexible in extension. Over the past 15 years, a number of studies have been carried out to extend the formulations of PS and PA methods to consider the flexibility of reinforcement layers [18-22]. In the literature, closed form solutions exist for the vertical stiffness of FREIs with strip, circular and rectangular shapes. Tsai [22] used the PA method and included the effect of end boundary condition on the compression response of FREIs with a circular shape.

#### 1.4.2 Lateral Stiffness

The most important mechanical property of a seismic isolator is its lateral stiffness [4]. For SREIs (or FREIs employed in a bonded application), the effective (secant) lateral stiffness can be estimated by

$$K_h = \frac{GA}{t_r} \quad (1.1)$$

where  $G$  is the shear modulus of elastomer material,  $A$  is the plan area of the isolator and  $t_r$  is the total thickness of elastomer layers.

Due to the lack of flexural rigidity in the fiber reinforcement layers and absence of steel end plates, FREIs undergo a unique rollover deformation when subjected to lateral loading. Figure 1.4 compares the deformed shapes of a FREI under lateral loading with a SREI. Figure 1.5 shows a typical lateral load-displacement relationship of a FREI obtained from lateral cyclic testing. As the lateral displacement increases and due to the rollover, the effective stiffness of the isolator reduces. At larger displacement amplitudes, the originally vertical faces of the isolator contact the loading surfaces and result in an increase in the effective stiffness. Toopchi-Nezhad et al. [11] showed that the reduction in the effective stiffness of FREIs due to rollover deformation may cause instability issues, if the length-to-total height ratio (defined as aspect ratio) of the isolator is less than a certain value. The initial softening of FREIs can increase the efficiency of the isolation system by increasing the isolation period. The stiffening response observed in FREIs at larger displacement can be an advantage, as it limits the isolation displacement under extremely large rare seismic events [13].

The available closed-form solutions for the complex lateral response of FREIs [15, 24-27] are developed for strip-shaped isolators and are based on a number of simplifying assumptions (e.g., the free surface of the rollover portion is stress-free, the lateral response of the isolator is independent of the magnitude of vertical load). In the absence of sophisticated analytical solutions, finite element analysis (FEA) can be employed to investigate the lateral response characteristics of FREIs. Due to the near incompressibility of elastomer material, large displacements and complex contact problem, FEA of FREIs

under lateral loads requires high computational effort. There are a number of FEA studies on the lateral response of FREIs, which are primarily limited to 2D analyses [20, 28, 29].

### **1.4.3 Rectangular FREIs**

Due to the simplicity of manufacturing, most researchers have investigated rectangular-shaped (either square or long strip) FREIs [8-14]. Long rectangular FREIs have an advantage over square or circular-shaped isolators when the superstructure is comprised of structural walls (e.g., masonry or concrete shear walls) [6]. When applying seismic isolation to buildings with structural walls, additional wall-beam elements are needed to span between isolators and support the walls. Using long rectangular isolators provides a more uniform distribution of the gravity loads and can potentially reduce installation costs. However, unlike circular or annular shaped isolators, a different response is expected from rectangular FREIs when subjected to lateral loading along different directions. Investigating the lateral response of rectangular-shaped FREIs requires 3D FEA.

### **1.4.4 FREI Models**

In ASCE-7 [30], conducting time history analyses is recommended in designing seismic isolation systems. Performing such analyses requires computational models that accurately predict the lateral response of the isolators. The bilinear idealization is a commonly used model for several types of SREIs [4]. For FREIs, different models have been proposed and used in the time history analyses [31-33]. However, conducting nonlinear time history analysis using the existing FREI models requires a number of

iterations and a customized numerical code. In addition, experimental test results are required to determine the parameters of these models. A simplified model for the lateral response of FREIs that requires no iteration, and can be employed in general purpose structural analysis codes can facilitate the analysis and design of structures isolated with this type of isolators.

### **1.5 Research Objectives**

The main objectives of this research were to provide a better understanding of the mechanical behaviour of FREIs under vertical and lateral loading through FEA, develop an accurate dynamic model for use in nonlinear time history analysis, and to demonstrate the efficiency of rectangular FREIs in seismically isolating buildings with structural walls.

### **1.6 Organization of the Thesis**

This thesis was prepared in accordance with the regulations of a “sandwich” thesis format. Thus, each chapter contains its own introduction, conclusion and bibliography.

In the second chapter of this thesis (Paper #1), 3D FEA is carried out on sixteen FREIs to investigate their vertical response characteristics. The overall dimensions of the isolators were kept constant, while the number of elastomer layers and the in-plane tensile stiffness of reinforcement material were the parameters that were varied. The range of values of in-plane tensile stiffness of reinforcement layers was selected to represent a large variety of applicable materials (e.g., steel, carbon and glass FRP). The FEA results were compared against the predictions of two analytical methods, the

pressure solution [18] and the pressure approach [20]. In addition, the accuracy of the assumptions made in the analytical solutions was investigated for the various cases considered in the study.

In the third chapter of this thesis (Paper #2), 3D FEA is carried out to study the lateral response characteristics of square-shaped FREIs. The lateral load-displacement relationships obtained from FEA for the FREIs tested by Toopchi-Nezhad et al. [11] were compared against the experimental results and good overall agreement was observed. The evaluated FEA models were used to investigate the response of the FREIs subjected to lateral loading along various directions. In addition, the stress distributions in the elastomer and fiber reinforcing layers were studied under different loading conditions.

In Chapter 4 of this thesis (Paper #3), a new computational model is proposed for the lateral response of FREIs to be used in nonlinear time history analysis. The proposed Pivot-Elastic model is non-iterative and can be employed in general purpose structural analysis codes. In addition, determination of the model parameters does not necessarily require experimentally obtained hysteresis loops of the isolators, and the effective stiffness values obtained from FEA or closed-form solutions along with the estimated values for the damping ratio of the isolators can be used to determine the model parameters. Thus, the proposed model can also be used to conduct preliminary design analysis. The proposed model was used to conduct nonlinear time history analysis of a two-storey steel moment frame structure seismically isolated with FREIs. The predicted response of the structure under a total of six earthquake excitations was compared against

the results of a previous shake table study [29] to evaluate the predictions of the proposed model.

In Chapter 5 of this thesis (Paper #4), experimental and FEA studies are carried out to study the lateral response of rectangular shaped FREIs, a shape postulated to be suitable for masonry or shear wall buildings. In addition, the concept of using geometric modifications, as an additional parameter to optimize the design of seismic isolation system using FREIs was investigated by conducting a parametric FEA study.

In Chapter 6 (Paper #5) of this thesis, the rectangular FREI considered in Chapter 5 was used to seismically isolate a two-storey reinforced concrete shear wall building. A set of ten earthquake ground motions were selected to match the design response spectrum for a site in Vancouver. For each ground motion, three earthquake hazard levels were considered for the analysis. The Pivot-Elastic model, proposed in Chapter 4 was used to model the lateral response of rectangular FREIs. Three isolators were considered underneath each shear wall to provide a uniform distribution of vertical loads. The efficiency of the isolation system composed of rectangular FREIs was evaluated by investigating the seismic response of the structure with and without the seismic isolation system.

## **1.7 References**

- [1] Christopoulos C, Filiatrault A. Principles of passive supplemental damping and seismic isolation, IUSS Press; 2006.

- [2] Datta TK. Structural control for seismic disaster mitigation, International Workshop on Earthquake Hazards and Mitigation. Guwahati, India, 7-8 December 2007.
- [3] Skinner RI, Robinson WH, McVerry GH. An introduction to seismic isolation, John Wiley & Sons, New York; 1993.
- [4] Jangid RS, Kelly JM. Base isolation for near-fault motions, *Earthquake Engineering and Structural Dynamics* 2001; 30(5):691-707.
- [5] Naeim F, Kelly JM. Design of seismic isolated structures: From theory to practice. John Wiley & Sons, New York; 1999.
- [6] Priestley MJN, Seible F, Calvi GM. Seismic design and retrofit of bridges, John Wiley & Sons, New York; 1996.
- [7] Kelly JM. Analysis of fiber-reinforced elastomeric isolators. *Journal of Seismology and Earthquake Engineering* 1999; 2(1):19-34.
- [8] Foster BAD. Base isolation using stable unbonded fibre reinforced elastomeric isolators (SU-FREI). M.A.Sc. thesis, McMaster University: Hamilton, 2011.
- [9] Kelly JM. Seismic isolation systems for developing countries. *Earthquake Spectra* 2002; 18(3):385–406.
- [10] Moon BY, Kang GJ, Kang BS, Kim GS, Kelly JM. Mechanical properties of seismic isolation system with fiber-reinforced bearing of strip type. *International Applied Mechanics* 2003; 39(10):1231–9.
- [11] Toopchi-Nezhad H, Tait MJ, Drysdale RG. Testing and modeling of square carbon fiber-reinforced elastomeric seismic isolators. *Structural Control and Health Monitoring* 2007;15(6):876–900.

- [12] Mordini A, Strauss A. An innovative earthquake isolation system using fibre reinforced rubber bearings. *Journal of Engineering Structures* 2008; 30(10):2739–51.
- [13] Toopchi-Nezhad H, Tait MJ, Drysdale RG. Lateral response evaluation of fiber-reinforced neoprene seismic isolators utilized in an unbonded application. *Journal of Structural Engineering* 2008; 134(10):1627–37.
- [14] Russo G, Pauletta M, Cortesia A. A study on experimental shear behavior of fiber reinforced elastomeric isolators with various fiber layouts, elastomers and aging condition. *Engineering Structures* 2013; 52:422-433.
- [15] Kelly JM, Konstantinidis D. *Mechanics of rubber bearings for seismic and vibration isolation*. Chichester, UK: Wiley; 2011.
- [16] Kelly JM. *Earthquake-resistant design with rubber*. 2nd ed. London: Springer-Verlag; 1997.
- [17] Tsai HC, Lee C. Compressive stiffness of elastic layers bonded between rigid plates. *International Journal of Solids and Structures* 1998;35(23):3053–69.
- [18] Tsai HC, Kelly JM. *Stiffness analysis of fiber-reinforced elastomeric isolators*. Pacific Earthquake Engineering Research Center, PEER, Berkeley, California; 2001/5.
- [19] Tsai HC, Kelly JM. *Stiffness analysis of fiber-reinforced rectangular isolators*. *Journal of Engineering Mechanics* 2002;128(4):462–70.
- [20] Kelly JM, Calabrese A. *Mechanics of fiber reinforced bearings*. Pacific Earthquake Engineering Research Center, PEER, Berkeley, California; 2012/101.

- [21] Tsai HC. Compression stiffness of infinite-strip bearings of laminated elastic material interleaving with flexible reinforcements. *International Journal of Solids and Structures* 2004;41(24):6647–60.
- [22] Tsai HC. Compression stiffness of circular bearings of laminated elastic material interleaving with flexible reinforcements. *International Journal of Solids and Structures* 2006; 46(11):3484–97.
- [23] Kelly JM, Konstantinidis D. Low-cost seismic isolators for housing in highly seismic developing countries. In ASISi 10th World conference on seismic isolation, energy dissipation and active vibrations control of structures, Istanbul; 28-31 May 2007.
- [24] Konstantinidis D, Kelly JM, Makris N. Experimental investigations on the seismic response of bridge bearings. Earthquake Engineering Research Center, University of California, Berkeley, 2008; Report No. EERC-2008/02.
- [25] Van Engelen N, Tait MJ, Konstantinidis D. A model of the shear behaviour of unbonded fiber reinforced elastomeric isolators (FREIs) including rollover. *Journal of Structural Engineering* 2014; (in press).
- [26] Peng TB, Zhang H, Li JZ, Li WX. Pilot study on the horizontal shear behaviour of FRP rubber isolators. *Journal of Vibration and Shock* 2009; 28(1):127–130. In Chinese.
- [27] Toopchi-Nezhad H. Horizontal stiffness solutions for unbonded fiber reinforced elastomeric bearings. *Structural Engineering and Mechanics* 2014; 49(3):395-410.

- [28] Toopchi-Nezhad H, Tait MJ, Drysdale RG. Bonded versus unbonded strip fiber reinforced elastomeric isolators: finite element analysis. *Composite Structures* 2011;93(2):850–9.
- [29] Kelly JM, Marsico MR. Stability and post-buckling behavior in nonbolted elastomeric isolators. *Seismic Isolation and Protection Systems* 2010;1(1):41–54.
- [30] ASCE-7. Minimum design loads for buildings and other structures, ASCE/SEI 7–10. New York, American Society of Civil Engineers; 2010.
- [31] Toopchi-Nezhad H, Tait MJ, Drysdale RG. Simplified analysis of a low-rise building seismically isolated with stable unbonded fiber reinforced elastomeric isolators. *Canadian Journal of Civil Engineering* 2009; 36:1182-1194.
- [32] Toopchi-Nezhad H, Tait MJ, Drysdale RG. A novel elastomeric base isolation system for seismic mitigation of low-rise buildings. in 14th world conference on earthquake engineering. Beijing, 12–18 October 2008.
- [33] Love JS, Tait MJ, Toopchi-Nezhad H. A hybrid structural control system using a tuned liquid damper to reduce the wind induced motion of a base isolated structure. *Engineering Structures* 2011; 33(3):738-746.

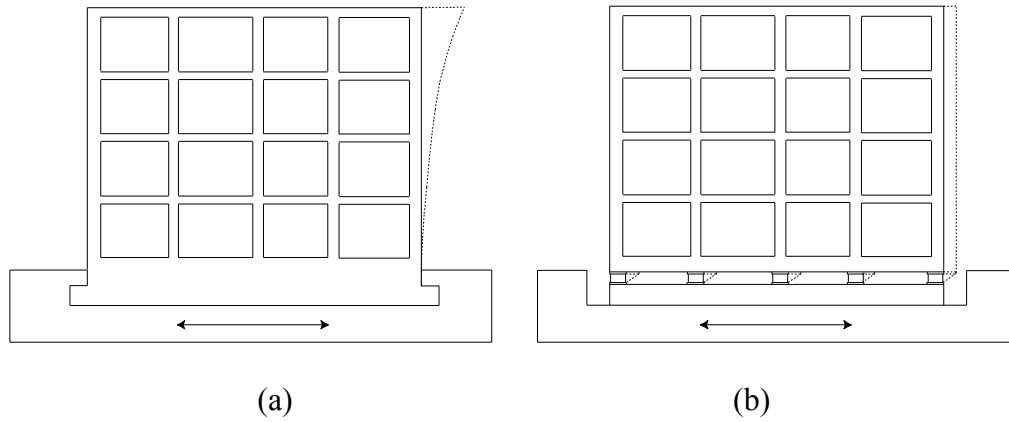


Figure 1.1. Schematic view of the deformation of a structure without (a) and with (b) seismic isolation

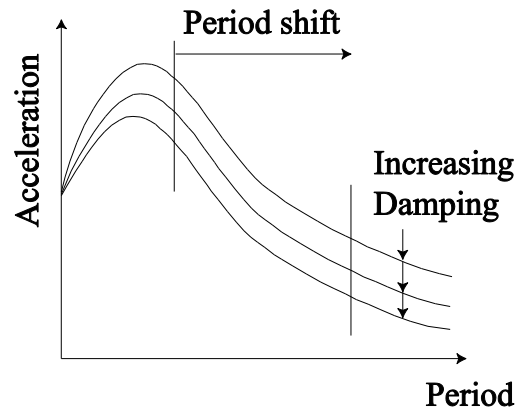


Figure 1.2. Reduction in seismic acceleration at larger period and damping [3]

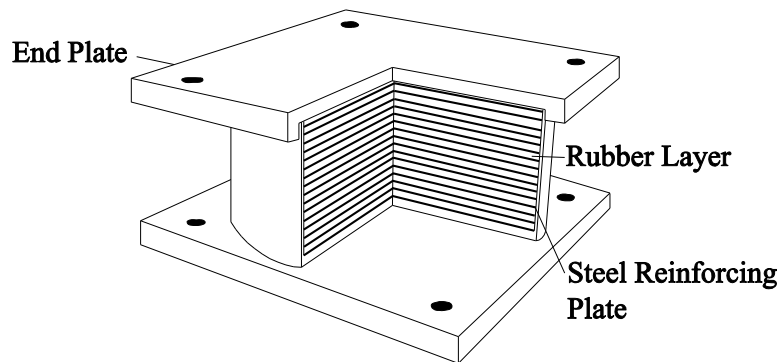


Figure 1.3. A typical SREI

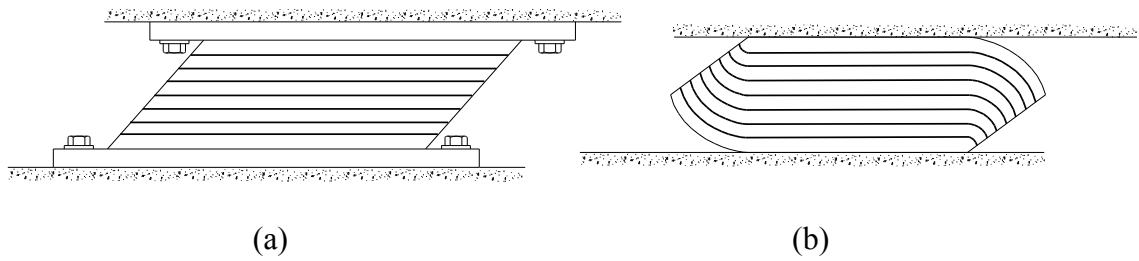


Figure 1.4. Schematic deformed shapes of a (a) SREI and a (b) FREI under lateral loading

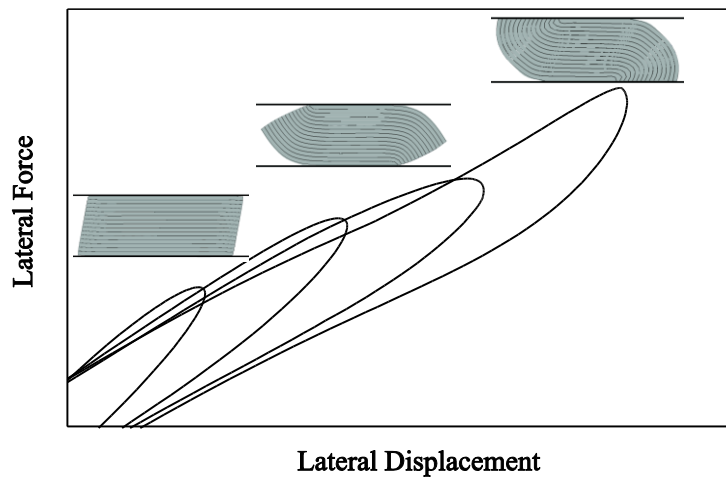


Figure 1.5. A typical load-displacement relationship of FREIs obtained from cyclic testing

## **Chapter 2: Three-Dimensional Finite Element Analysis of Circular Fiber-Reinforced Elastomeric Bearings under Compression**

### **Abstract**

Fiber reinforced elastomeric isolators (FREIs) are a relatively new type of elastomeric bearing. FREIs utilize fiber material for the reinforcing layers instead of steel which is used in conventional steel reinforced elastomeric isolators (SREIs). Unlike SREIs, where the steel reinforcing material is usually assumed to be rigid in extension, the reinforcing fiber layers are considered to be flexible in extension. As a result, the vertical response characteristics of FREIs differ from those of SREIs. In this study, a 3D parametric numerical finite element analysis (FEA) is carried out on sixteen circular FREI bearings. All bearings investigated have the same overall dimensions, while the thickness of elastomer layers and the axial stiffness of reinforcement are the parameters that are varied. FEA results, in terms of deformed shape, stiffness, stress and/or strain in reinforcing and elastomer layers are compared with predicted values obtained using the pressure solution and the pressure approach methods. Good overall agreement was observed between the FEA results and the results obtained from analytical solutions. It was concluded that the end boundary effect, which is often neglected, becomes a contributing factor on the vertical response for bearings reinforced with flexible reinforcements, or bearings with low shape factor values.

## **2.1 Introduction**

Seismic isolation in North America is primarily limited to high importance or post-disaster buildings, such as historical structures, hospitals and emergency centers. This limitation is largely due to the high manufacturing and installation costs associated with traditional seismic isolation systems. Currently, it is not economically feasible to employ these traditional seismic isolation systems in smaller structures such as residential buildings. A reduction in both the weight and cost of isolators is expected to significantly increase the application of this valuable technology to ordinary low-rise buildings [1]. In steel reinforced elastomeric isolators (SREIs), which are the most common isolators in use, the overall weight is mainly due to the thick top and bottom steel end plates as well as the steel reinforcing shims. The high cost of SREIs is predominantly associated with the highly labor-intensive manufacturing process [2].

The role of the reinforcing layers in elastomeric bearings is to limit the lateral bulging of the elastomer under vertical compression loads, thus increasing the vertical stiffness of the bearings and suppressing the rocking mode of vibration [3]. Reinforcing layers also allow the elastomer to shear freely under lateral loads in order to maintain the large lateral flexibility requirement. The weight of SREIs can be reduced by eliminating the thick steel end plates and replacing the steel shims with reinforcement made of alternative materials having the same order of elastic stiffness, e.g. carbon fiber material [4]. These modifications alter the deformation pattern of a bearing under horizontal displacement. However, if properly designed these modifications can result in stable unbonded isolators having favorable seismic isolation characteristics [5,6].

Fiber reinforced elastomeric isolators (FREIs) are a relatively new type of elastomeric bearing that utilize fiber material for the reinforcing layers. Previous studies [2, 4-7] have shown that it is possible to achieve adequate vertical stiffness with FREIs. Under horizontal cyclic testing, unbonded FREIs exhibit superior energy dissipation compared to bonded SREIs [6,7] resulting in improved seismic mitigation efficiency in terms of reducing base shear and isolator displacement [8,9]. In conventional SREIs, the reinforcing material is steel and is usually assumed to be rigid in extension. In FREIs however, the reinforcing fiber layers are flexible in extension, and thus the vertical response characteristics of FREIs may differ from those of SREIs.

Several analytical solutions have been developed to evaluate the vertical response of elastomeric bearings. One of the earliest analyses of the compression stiffness was conducted by Rocard [10] using an energy approach. Additional advancements were made by Gent and Lindley [11], who derived expressions for the compressive stiffness of incompressible infinite-strip-shaped and circular-shaped elastic layers bonded to rigid plates. Gent and Meinecke [12] subsequently extended the analysis and derived the compression modulus for square shape elastic layers. Lindley [13] applied the energy method to compressible elastic layers. Kelly [14] introduced the *pressure solution* (PS) method for determining the vertical compression stiffness of compressible elastic layers bonded to rigid plates. This method is based on the following three assumptions:

- (i) The top and bottom surfaces of the elastomer layers remain horizontal after application of the vertical load.
- (ii) Points on a vertical line in the initial state form a parabola after loading.

(iii) The normal stresses in the elastomer can be approximated by the pressure.

Tsai and Kelly [1,15,16] extended the PS method for analyzing the compression and bending stiffness of infinite-strip, rectangular and circular elastic layers bonded to flexible plates. Kelly [2] derived the compression stiffness of infinite-strip elastic layers bonded to flexible plates considering bulk compressibility. Kelly and Calabrese [17] derived the compression stiffness of incompressible rectangular and compressible circular pads bonded to flexible plates.

Tsai and Lee [18] derived the compression stiffness of infinite-strip, circular and square elastic compressible pads using a method similar to the PS, but relying only on the two kinematic assumptions (i and ii). This method hereafter is referred to as the *pressure approach* (PA). Tsai [19,20] used the PA method to derive the vertical stiffness of infinite-strip and circular bearings with flexible reinforcements considering the compressibility of the elastomer. Solutions were presented for the effective compression modulus for two boundary conditions (rigid-end and free-end), as well as the monotonic deformation case, where every layer in the bearing is assumed to deform identically, and thus has the same compression modulus.

Pinarbasi et al. [21,22] developed an analytical solution based on the modified Galerkin method for the analysis of elastic layers bonded to rigid plates for infinite-strip, circular and annular shapes. The order of the theory is based on the number of shape functions considered in the displacement expansions. The method was extended [23, 24] to investigate the vertical response of elastic layers bonded to flexible plates.

A number of finite element analysis (FEA) studies investigating the response behavior of FREIs have been conducted and presented in the literature. Most of these studies have focused on the horizontal response characteristics of the bearings [25-29]. However, relatively few FEA studies have focused on the vertical response characteristics of FREIs. Toopchi-Nezhad et al. [30] carried out a 2D FEA to investigate the stress distribution and vertical stiffness of a strip FREI. Five different values of tensile stiffness were considered for the reinforcing material and the results were compared with predictions obtained using the PS method. It was found that for bearings with fiber reinforcement of relatively low stiffness, the FEA results significantly differ from the pressure solution based predicted values. Toopchi-Nezhad et al. [29] extended the 2D FEA and investigated the influence of individual elastomer layers on the vertical and horizontal response of unbonded strip FREIs. Kelly and Calabrese [17] performed FEA and investigated the vertical and horizontal response characteristics of strip, circular and square FREI bearings. 2D analysis on six strip FREI bearings was conducted under pure compression and combined compression and shear loads. The vertical response of six circular and six square FREI bearings was investigated using 3D FEA. The vertical stiffness values obtained from FEA were compared with predicted values obtained from the pressure solution method and good overall agreement was found.

This paper presents the results of a 3D parametric FEA of circular FREIs under compression. While the symmetry of the problem makes it possible to use axisymmetric 2D analysis, full 3D analysis is conducted so as to validate 3D FEA models against both the PS and PA analytical solutions. 3D finite element models such as these can

subsequently be used to study the behavior of circular bearings under non-symmetric loading conditions, e.g., combined vertical and lateral loading, for which an axisymmetric analysis is not possible. To investigate the effect of reinforcement stiffness on the vertical response behavior of circular bearings with different shape factors (defined as the ratio of the total loaded area of one elastomer layer to the load free area), sixteen circular bearings with the same overall dimensions, but varying number of elastomer layers and a wide range of reinforcement tensile stiffness are modeled and analyzed using the commercially available finite element program MSC Marc [31]. In addition, this study also examines the effect of end boundary conditions as well as the magnitude of the vertical load on the overall response of the bearings. It should be noted that the analytical solutions are based on small deformation theory assuming linearly elastic material behavior, while the FEA incorporates a large deformation formulation, and the rubber is treated as a compressible Neo-Hookean hyperelastic material.

## 2.2 Review of Analytical Solutions

Among the various analytical solutions discussed earlier, the *pressure solution* (PS) and the *pressure approach* (PA) methods are used in this study. The PS method is the most common method for calculating the vertical stiffness of elastomeric bearings and the PA method, although similar to PS, considers different end boundary conditions.

### 2.2.1 Pressure Solution (PS)

Figure 2.1 shows a circular elastic pad of radius  $b$  and thickness  $t$  bonded on top and bottom to flexible reinforcement plates of thickness  $t_f$ . Following the pressure solution,

Kelly and Calabrese [17] derived the effective compression modulus  $E_c^{PS}$  of the circular fiber reinforced elastomeric pad considering the compressibility of the elastomer:

$$E_c^{PS} = 24GS^2(1 + \nu_f) \frac{I_0(\eta) - \frac{2}{\eta}I_1(\eta)}{\alpha^2 \left[ I_0(\eta) - \frac{1 - \nu_f}{\eta}I_1(\eta) \right] + \beta^2 \frac{1 + \nu_f}{2}I_0(\eta)} \quad (2.1)$$

where  $G$  is the shear modulus of the elastomer,  $S = b/2t$  is the shape factor,  $\nu_f$  is Poisson's ratio for the reinforcement material and  $I_i$  is the modified Bessel function of the first kind of order  $i$ . The parameters  $\alpha$ ,  $\beta$  and  $\eta$  are defined by

$$\alpha = \sqrt{\frac{12(1 - \nu_f^2)Gb^2}{E_f t_f t}}; \quad \beta = \sqrt{\frac{12Gb^2}{\kappa t^2}}; \quad \eta = \sqrt{\alpha^2 + \beta^2} \quad (2.2)$$

where  $E_f$  is the elastic modulus of the reinforcement layer material, and  $\kappa$  is the bulk modulus of the elastomer. The compression force  $P$  in a single pad compressed by an amount  $\delta$  is expressed as

$$P = \frac{E_c A \delta}{t} \quad (2.3)$$

where  $A = \pi b^2$  is the loaded area of the layer and  $E_c$  is the effective compression modulus. For a bearing consisting of  $n - 1$  elastomer layers interleaved with  $n - 1$  reinforcement layers, as shown in Fig 2.2, and the assumption that all the layers have the same compression modulus (neglecting the boundary effects), the total vertical stiffness is calculated to be

$$K_v = \frac{E_c A}{t_r} \quad (2.4)$$

where  $t_r$  is the total thickness of elastomer layers. The internal forces per unit length in the reinforcing layers in polar coordinates are given by

$$N_{rr}^{PS}(r) = \frac{E_f t_f}{2(1 - \nu_f)} \frac{\Delta}{t} \left[ 1 - \frac{I_0(\alpha r) - \frac{1 - \nu_f}{\alpha r} I_1(\alpha r)}{I_0(\alpha b) - \frac{1 - \nu_f}{\alpha b} I_1(\alpha b)} \right] \quad (2.5)$$

$$N_{\theta\theta}^{PS}(r) = \frac{E_f t_f}{2(1 - \nu_f^2)} \frac{\Delta}{t} \left[ 1 - \frac{\nu_f I_0(\alpha r) + \frac{1 - \nu_f}{\alpha r} I_1(\alpha r)}{I_0(\alpha b) - \frac{1 - \nu_f}{\alpha b} I_1(\alpha b)} \right] \quad (2.6)$$

where  $\Delta = \bar{p}t/E_c$  is the total vertical displacement of the elastomer layer under the total compression load  $P$  and  $\bar{p} = P/A$  is the mean vertical pressure. The pressure  $p^{PS}(r)$  in the elastomer is given by

$$p^{PS}(r) = \frac{8Gb}{\eta t^2} A_1 \left[ I_0(\eta) - I_0\left(\eta \frac{r}{b}\right) \right] \quad (2.7)$$

where  $A_1$  is defined

$$A_1 = \frac{\Delta}{2t} (1 + \nu_f) \left\{ \frac{2\alpha^2}{3\eta b} \left[ I_0(\eta) - \frac{1 - \nu_f}{\eta} I_1(\eta) \right] + \frac{2\beta^2}{3\eta b} \frac{1 + \nu_f}{2} I_0(\eta) \right\}^{-1} \quad (2.8)$$

Knowing the pressure  $p^{PS}(r)$ , the normal stresses, normal strains and the displacements within the elastomer pad can be calculated. The shear strains developed in the elastomer under compression can be calculated by

$$\gamma_{rz}^{PS} = -\frac{8z}{t^2} A_1 I_1 \left( \eta \frac{r}{b} \right) \quad (2.9)$$

## 2.2.2 Pressure Approach (PA)

### 2.2.2.1 Monotonic Deformation

Tsai [20] derived the effective compression modulus of a circular pad bonded to flexible reinforcements using the PA method:

$$E_c^{PA} = 2\mu + \frac{\mu\lambda}{\lambda + \mu} + \frac{\lambda^2(\lambda + 2\mu)}{(\lambda + \mu)^2} \left( \frac{\alpha_0^2}{2D_1} \right) \left[ I_0(\beta_0 b) - \frac{2I_1(\beta_0 b)}{\beta_0 b} \right] \quad (2.10)$$

where  $\mu$  and  $\lambda$  are Lamé's constants and  $\alpha_0$ ,  $\beta_0$  and  $D_1$  are defined by

$$\alpha_0 = \frac{1}{t} \sqrt{\frac{12\mu}{\lambda + 2\mu}}; \quad \beta_0 = \sqrt{\alpha_0^2 + \alpha_1^2} \quad (2.11)$$

$$D_1 = \frac{\alpha_0^2}{\lambda + \mu} \left[ \left( \frac{\lambda}{2} + \mu \right) I_0(\beta_0 b) - \mu \frac{I_1(\beta_0 b)}{\beta_0 b} \right] + \frac{\alpha_1^2}{1 + \nu_f} \left[ I_0(\beta_0 b) - (1 - \nu_f) \frac{I_1(\beta_0 b)}{\beta_0 b} \right] \quad (2.12)$$

and  $\alpha_1$  is given by

$$\alpha_1 = \sqrt{\frac{12\mu(1 - \nu_f^2)}{E_f t_f t}} \quad (2.13)$$

The total vertical stiffness of the bearing can then be calculated using Eq. (2.4).

### 2.2.2.2 Rigid Ends

Elastomeric isolators are usually bonded to steel end plates. These steel plates are assumed to be rigid and affect the vertical response behavior of the elastomer layers. The bearing shown in Fig. 2.2 is assumed to be perfectly bonded to rigid end plates. The diameter of the bearing is  $2b$  and each elastomeric layer has a thickness of  $t$ . In order to account for the rigid end effects, Tsai [20] assumed that the horizontal displacements of the successive reinforcement layers are quadratically proportional to a displacement function in all reinforcement layers. The effective compression modulus of the  $i^{\text{th}}$  elastomeric layer is expressed as

$$E_c^{PA,i} = 2\mu + \lambda - \frac{2\lambda}{D_3} \left\{ \left( 1 - \frac{\alpha_{2i}^2}{\beta_{2i}^2} \right) \left[ I_0(\beta_{3i}b) - (1 - \nu_f) \frac{I_1(\beta_{3i}b)}{\beta_{3i}b} \right] \frac{I_1(\beta_{2i}b)}{\beta_{2i}b} - \left( 1 - \frac{\alpha_{2i}^2}{\beta_{3i}^2} \right) \left[ I_0(\beta_{2i}b) - (1 - \nu_f) \frac{I_1(\beta_{2i}b)}{\beta_{2i}b} \right] \frac{I_1(\beta_{3i}b)}{\beta_{3i}b} \right\} \quad (2.14)$$

with

$$\alpha_{2i}^2 = \frac{\alpha_1^2(-f_{i+1} + 2f_i - f_{i-1})}{12f_i} = \frac{2\alpha_1^2}{3n^2f_i}; \quad \alpha_{3i}^2 = \frac{(f_i + f_{i-1})\alpha_1^2}{2f_i} \quad (2.15)$$

$$\beta_{2i}^2 = \frac{1}{2} \left[ \alpha_0^2 + \alpha_{2i}^2 + \alpha_{3i}^2 - \sqrt{(\alpha_0^2 + \alpha_{2i}^2 + \alpha_{3i}^2)^2 - 4\alpha_0^2\alpha_{2i}^2} \right] \quad (2.16)$$

$$\beta_{3i}^2 = \frac{1}{2} \left[ \alpha_0^2 + \alpha_{2i}^2 + \alpha_{3i}^2 + \sqrt{(\alpha_0^2 + \alpha_{2i}^2 + \alpha_{3i}^2)^2 - 4\alpha_0^2\alpha_{2i}^2} \right] \quad (2.17)$$

$$\begin{aligned}
D_3 = & \left[ \left( 1 + \frac{2\mu}{\lambda} \right) I_0(\beta_{2i}b) - \frac{2\mu}{\lambda} \frac{I_1(\beta_{2i}b)}{\beta_{2i}b} \right] \left( 1 - \frac{\alpha_{2i}^2}{\beta_{2i}^2} \right) \left[ I_0(\beta_{3i}b) \right. \\
& \left. - (1 - \nu_f) \frac{I_1(\beta_{3i}b)}{\beta_{3i}b} \right] \\
& - \left[ \left( 1 + \frac{2\mu}{\lambda} \right) I_0(\beta_{3i}b) - \frac{2\mu}{\lambda} \frac{I_1(\beta_{3i}b)}{\beta_{3i}b} \right] \left( 1 - \frac{\alpha_{2i}^2}{\beta_{3i}^2} \right) \left[ I_0(\beta_{2i}b) \right. \\
& \left. - (1 - \nu_f) \frac{I_1(\beta_{2i}b)}{\beta_{2i}b} \right]
\end{aligned} \tag{2.18}$$

In Eq. (2.15)  $f_i$  is defined by

$$f_i = 4 \frac{i}{n} \left( 1 - \frac{i}{n} \right) \tag{2.19}$$

In order to calculate the total vertical stiffness of the bearing with rigid end supports, the effective compression modulus of all the elastomeric layers should be calculated. The vertical stiffness of the bearing can be obtained by

$$(K_v)_{\text{rigid}} = \frac{A}{t \sum_{i=1}^n \frac{1}{E_c^{PA,i}}} \tag{2.20}$$

The internal forces per unit length in reinforcing layer  $i$  can be calculated from

$$\begin{aligned}
N_{rr}^{PA,i}(r) = & \left( \frac{6\mu\lambda}{\lambda + \mu} \right) \frac{\varepsilon_c^{(i)}}{D_1 t} \left\{ [I_0(\beta_0 b) - I_0(\beta_0 r)] \right. \\
& \left. - (1 - \nu_f) \left[ \frac{I_1(\beta_0 b)}{\beta_0 b} - \frac{I_1(\beta_0 r)}{\beta_0 r} \right] \right\}
\end{aligned} \tag{2.21}$$

$$\begin{aligned}
N_{\theta\theta}^{PA,i}(r) = & \left( \frac{6\mu\lambda}{\lambda + \mu} \right) \frac{\varepsilon_c^{(i)}}{D_1 t} \left\{ \left[ I_0(\beta_0 b) - \nu_f I_0(\beta_0 r) \right] \right. \\
& \left. - (1 - \nu_f) \left[ \frac{I_1(\beta_0 b)}{\beta_0 b} + \frac{I_1(\beta_0 r)}{\beta_0 r} \right] \right\}
\end{aligned} \tag{2.22}$$

where  $\varepsilon_c^{(i)} = \bar{p}/E_c^{PA,i}$  is the average compression strain for elastomer layer  $i$ . Unlike the PS method where the pressure is assumed to be constant through the thickness of the elastomer pad ( $p^{PS}(r, z) = p^{PS}(r)$ ), in the PA method the pressure can vary along the thickness of the elastomer layers. However, the derivations in the PA method are based on the average value for the pressure, defined by

$$p_{ave}^{PA,i}(r) = -\frac{1}{t} \int_{-t/2}^{t/2} p^{PA,i}(r, z) dz \tag{2.23}$$

where  $p^{PA,i}(r, z)$  is the pressure in the elastomer layer  $i$ . The average pressure in elastomer layer  $i$  is given by

$$\begin{aligned}
p_{ave}^{PA,i}(r) = & \kappa \left\langle \frac{\Delta^i}{t} \right. \\
& - \frac{\Delta^i}{t D_3} \left\{ \left( 1 - \frac{\alpha_{2i}^2}{\beta_{2i}^2} \right) \left[ I_0(\beta_{3i} b) - (1 - \nu_f) \frac{I_1(\beta_{3i} b)}{\beta_{3i} b} \right] I_0(\beta_{2i} r) \right. \\
& \left. \left. - \left( 1 - \frac{\alpha_{2i}^2}{\beta_{3i}^2} \right) \left[ I_0(\beta_{2i} b) - (1 - \nu_f) \frac{I_1(\beta_{3i} b)}{\beta_{3i} b} \right] I_0(\beta_{2i} r) \right\} \right\rangle
\end{aligned} \tag{2.24}$$

where  $\Delta_i = \varepsilon_c^{(i)} t$  is the total vertical displacement of elastomer layer  $i$  under the total compression load  $P$ .

From the solution for  $p_{ave}^{PA,i}(r)$  presented by Tsai [20], the shear strains  $\gamma_{rz}^{PA,i}$  in elastomer layer  $i$  can be computed using

$$\gamma_{rz}^{PA,i} = \frac{1}{t} \left\{ [C_5 I_1(\beta_{2i}r) + C_6 I_1(\beta_{3i}r)] \left( -8 \frac{z}{t} \right) + u_f^{(i-1)} - u_f^{(i)} \right\} \quad (2.25)$$

where

$$C_5 = \frac{b^2 \bar{p} \pi}{E_c^{PA,i} A D_3} \left( 1 - \frac{\alpha_{2i}^2}{\beta_{2i}^2} \right) \left[ I_0(\beta_{3i}b) - \frac{(1 - \nu_f) I_1(\beta_{3i}b)}{\beta_{3i}b} \right] \left( \frac{3\beta_{2i}}{2\alpha_0^2} \right) \quad (2.26)$$

$$C_6 = \frac{b^2 \bar{p} \pi}{E_c^{PA,i} A D_3} \left( \frac{\alpha_{2i}^2}{\beta_{3i}^2} - 1 \right) \left[ I_0(\beta_{2i}b) - \frac{(1 - \nu_f) I_1(\beta_{2i}b)}{\beta_{2i}b} \right] \left( \frac{3\beta_{3i}}{2\alpha_0^2} \right) \quad (2.27)$$

and  $u_f^{(i)}$  is the displacement of the reinforcement layer  $i$  which can be calculated by

$$u_f^{(i)} = \frac{4f_i}{3\alpha_{2i}^2(f_i + f_{i-1})} [C_5(\alpha_0^2 + \alpha_{3i}^2 - \beta_{2i}^2)I_1(\beta_{2i}r) + C_6(\alpha_0^2 + \alpha_{3i}^2 - \beta_{3i}^2)I_1(\beta_{3i}r)] \quad (2.28)$$

### 2.3 Finite Element Analysis

In order to investigate the effect of the reinforcement material on the vertical response of circular elastomeric bearings with different shape factors, and to compare the results of the FEA against closed-form solutions, sixteen circular isolators were analyzed. All bearings had an overall thickness of 210 mm and a diameter of 600 mm. The parameters that varied from bearing to bearing were the shape factor  $S$  and the in-plane tensile stiffness of the reinforcement material  $K_f$ , defined by

$$K_f = \frac{E_f t_f}{1 - \nu_f^2} \quad (2.29)$$

In this study, a constant value of  $\nu_f = 0.3$  was used for the reinforcing material. A shear modulus of  $G = 0.8$  MPa and bulk modulus of  $K = 2000$  MPa, corresponding to an elastic modulus of  $E = 2.4$  MPa and Poisson's ratio of  $\nu = 0.4998$ , were used for the elastomer material. Table 2.1 shows the properties of the sixteen bearings analyzed in this study. The bearing designation BX-Y identifies a bearing with  $S = X$  and  $K_f = Y$  kN/mm. The range of values of  $K_f$  was selected to represent a large variety of materials. A value of 500 kN/mm is representative of steel reinforcement with  $E_f = 200$  GPa and  $t_f = 2.3$  mm, while a  $K_f = 50$  kN/mm is representative of a glass fiber reinforced polymer with  $E_f = 35$  GPa and a thickness of  $t_f = 1.3$  mm.

Finite element analyses were carried out using MSC Marc [31], a commercially available general purpose finite element program. The *Neo-Hookean* constitutive model was used to describe the elastomer material. This model is defined by two material constants that are directly related to the shear and bulk moduli of the material. Reinforcement materials were modeled using a linear-elastic isotropic material. All the analyses were carried out in 3D using the Updated Lagrangian formulation. The top and bottom supports were modeled using rigid contact surfaces. The contact between the bearings and rigid end surfaces was defined as GLUE in order to prevent slip along the interface. Linear full integration 8-node isoparametric hexahedron elements were used to model the elastomer. This element type uses a mixed formulation and is suited for incompressible and nearly incompressible materials. The reinforcement was modeled

using 4-node thin shell elements. All bearings were loaded monotonically up to a compressive load of 4524 kN ( $\bar{p} = 16$  MPa mean vertical pressure).

Different mesh sizes were considered in a preliminary analysis in order to track the modeling error and select the appropriate mesh size. Figure 2.3 shows the variation of the relative error in the models with respect to the number of 3D elements used to model elastomer layers along the height and diameter for bearing B5-10. The total number of the elements used in the bearing models are also shown in the figure in order to represent an estimate of the total analysis time required for each model. The relative error is calculated by comparing the values of the total vertical displacements of the models at a vertical load of 566 kN ( $\bar{p} = 2$  MPa). Figure 2.3 confirms that increasing the number of the elements along both the height and diameter of the bearing reduces the relative error. However, increasing the number of the elastomer elements along the height of the bearing increases the total number of the elements in the model by an order of one, while increasing the number of the elements along the diameter of the bearing increases the total number of the elements in the bearing model by an order of two. When using a total of 112 elements along the height of the bearing, (16 elements along the height of each elastomer layer), the relative error is calculated to be less than 0.1% for all the considered number of elements along the diameter of the bearing. Similar analysis was carried out for other bearings. In order to maintain a relative error of less than 0.1%, the total number of elements along the height of the bearings was selected to be 126, 168, 168 and 252 (corresponding to 18, 12, 6 and 6 elements along the thickness of each elastomer layer) for bearings with  $S = 5, 10, 20$  and  $30$ , respectively. The total number of the elements

used along the diameter of the bearings was 90, 80, 80 and 70 for bearings with  $S = 5$ , 10, 20 and 30, respectively. Since the maximum lateral bulging of elastomers occurs at the edges of the bearings, a finer mesh was used at the edges.

## 2.4 Results and Discussion

### 2.4.1 Deformed Shapes

Figure 2.4 shows the deformed shape of bearing B5-10 under  $\bar{p} = 2$  MPa. The effect of the rigid end boundary condition on the deformed shapes of top and bottom elastomer layers can be observed from the figure. Figure 2.5 shows the deformed shapes of the bearings with  $K_f = 100$  kN/mm under  $\bar{p} = 2$  MPa. The figure also illustrates the mesh size used to model the bearings. It can be seen that under the same applied vertical load, the lateral bulging of the elastomer layers is significantly reduced as the shape factor of the bearing is increased.

Figure 2.6 compares the deformed shapes of the first and center elastomer layers in bearings with  $S = 5$  and  $S = 30$  at  $r/b = 1/2$  and  $r/b = 5/6$ , obtained from FEA, PS and PA considering rigid end effects for  $K_f$  values of 10 kN/mm and 500 kN/mm. It can be observed from the figure that for the bearings with  $K_f = 500$  kN/mm, the predictions of the closed-form solutions are in very good agreement with the FEA results. Additionally, comparing the deformed shapes of the first and center elastomer layers shows that for bearings with  $K_f = 500$  kN/mm, the rigid ends have negligible effect on the deformed shape of the first elastomer layers. However, for bearings with  $K_f = 10$  kN/mm, the lateral deformation of the elastomer layers adjacent to the rigid supports is

reduced in comparison to the center layers, as a result of the constraint provided by the supports. This reduction is more noticeable in bearings with larger shape factor values. For bearings with  $K_f = 10$  kN/mm, the predictions of the PS method deviate from the FEA results within the first elastomer layer. For example, in the first elastomer layer of bearing B30-10, the maximum lateral deformation at  $r/b = 1/2$  is observed to occur at the interface between the elastomer and reinforcement layers ( $z/t = 0.5$ ), while at  $r/b = 5/6$  the maximum lateral deformation is observed to occur at  $z/t = 0.25$ . However, the PS method consistently predicts the maximum deformation to occur at  $z/t = 0$ .

#### 2.4.2 Influence of Applied Vertical Stress

Figure 2.7 compares the  $E_c/E$  of the bearings obtained from FEA calculated under different vertical pressures. It can be seen that the vertical stiffness of the bearings increases as the applied vertical compression load is increased. This stiffening behavior is induced by the nonlinearity of the Neo-Hookean material constitutive model as well as the geometric nonlinearity caused by the extreme lateral bulging of elastomers under larger vertical loads, and is pronounced in bearings with lower shape factors, while it is insignificant in bearings with  $S = 30$ . In B5-100, for example, the vertical stiffness of the bearing at  $\bar{p}/E = 6.67$  ( $\bar{p} = 16$  MPa) is almost 25% larger than at  $\bar{p}/E = 0.83$  ( $\bar{p} = 2$  MPa), while in B20-100 the increase is only 3%. Figure 2.7 also shows that for a given shape factor, the rate of stiffening is independent of  $K_f$ . In the PA and PS methods, which are based on small deformation theory, the elastomer material is assumed linear-elastic

isotropic and thus the calculated effective compression modulus is independent of the applied vertical load on the bearing. In order to minimize the stiffening behavior resulting from the vertical load and for comparison purposes, the FEA results under a mean vertical pressure of  $\bar{p} = 2$  MPa are utilized.

### 2.4.3 Vertical Stiffness

Table 2.2 shows the vertical stiffness of each bearing obtained from FEA, compared with the values obtained from the calculation of effective compression moduli using the PS (Eq. 2.1), the PA for monotonic loading (Eq. 2.10) and the PA considering rigid end effects (Eq. 2.14). It can be seen that the FEA results are in very good agreement with the predictions of the PA method considering the rigid end effects (Eq. 2.14) for all the bearings, with a maximum difference of 3.3%. Comparing the stiffness values predicted from FEA against those calculated using the PS (Eq. 2.1) and the PA for monotonic loading, it can be seen that the FEA predictions are closer to the latter for all the bearings studied. When neglecting the end effects, it can be seen that as the shape factor,  $S$ , of the bearings increases, the difference between  $K_v$  calculated using the PS and  $K_v$  calculated using the PA decreases, suggesting that for larger  $S$  values the normal components of the deviatoric stress are negligible, which is in agreement with the stress assumption in the PS. The effect of rigid ends on the overall stiffness of the bearings is notable in bearings with low shape factors as well as the bearings with low  $K_f$  values.

Figure 2.8 compares the overall compression modulus,  $E_c = K_v t_r / A$ , of the bearings divided by the elastic modulus of the elastomer  $E$  as a function of  $K_f / Et$ . The figure

shows four curves corresponding to  $S = 5, 10, 20$  and  $30$  that are obtained using the PA method, including the end effects, for a circular bearing with  $600$  mm diameter and  $t_r = 210$  mm. The points on the curves correspond to the FEA results. It can be seen that for larger shape factor values, the flexibility of the reinforcement plays an important role on the overall vertical stiffness of the bearings. For  $S = 5$  for example, decreasing the  $K_f$  from  $500$  kN/mm ( $K_f/Et = 6945$ ) to  $50$  kN/mm ( $K_f/Et = 695$ ) results in an 8% decrease in the total vertical stiffness (and in  $E_c/E$ ) of the bearing, while for  $S = 30$  the decrease is 90%. For the values of  $S$  considered in this study, replacing the flexible reinforcement having  $K_f = 500$  kN/mm with a completely rigid reinforcement results in a maximum of 2% increase in the bearing's overall vertical stiffness. This confirms the validity of the assumption of rigid reinforcement typically made when analyzing conventional SREIs.

Table 2.3 compares the ratio of the effective compression modulus of the first two elastomer layers to a mid-height layer,  $E_c^1/E_c^{\text{mid}}$  and  $E_c^2/E_c^{\text{mid}}$ , in all bearings obtained from FEA and the PA, including end effects (Eq. 2.14). It can be observed from the FEA results that for values of  $K_f \geq 50$  kN/mm, the boundary condition only affects the elastomer layers in contact with the supports, while the compression moduli of the second elastomer layers are very close to the center layer. Meanwhile, the difference between  $E_c^1/E_c^{\text{mid}}$  and  $E_c^2/E_c^{\text{mid}}$  is less than 2% for  $K_f = 500$  kN/mm. Comparing the results of FEA and theory, it can be seen that the PA method predicts lower values for the compression modulus of the first elastomer layer, and higher values for the compression modulus of the second elastomer layers. This could be attributed to the assumed

displacement function for the reinforcement layers in the PA method considering rigid end effects.

#### 2.4.4 Stress and Strain in Elastomer

Figures 2.9 and 2.10 show the normalized stress contours of radial stress  $\sigma_{rr}$  in the elastomer layers obtained at  $\bar{p} = 2$  MPa for the bearings with  $K_f = 10$  kN/mm and  $K_f = 500$  kN/mm, respectively. The stress values are normalized with respect to the mean pressure ( $\bar{p}$ ). It can be observed from the figures that the normalized radial stress values decrease as the shape factor of the bearing increases. Increasing the  $K_f$  value in the reinforcements from 10 kN/mm to 500 kN/mm results in an increase in the  $\sigma_{rr}$  values in the elastomer layers.

Figures 2.11, 2.12 and 2.13 show the variation of the normalized strains ( $\varepsilon_{rr}E/\bar{p}$ ,  $\varepsilon_{\theta\theta}E/\bar{p}$  and  $\varepsilon_{zz}E/\bar{p}$ ) obtained from FEA through the elastomer layers in bearings with  $K_f = 10$  kN/mm and  $K_f = 500$  kN/mm at  $r/b = 0$ ,  $r/b = 1/2$  and  $r/b = 5/6$ , respectively. Due to the axisymmetric nature of the bearings, at  $r/b = 0$ , the radial and tangential strains in the elastomer layers are equal ( $\varepsilon_{rr} = \varepsilon_{\theta\theta}$ ). As  $r/b$  increases, the tangential strains deviate from the radial strains and it can be observed from the figures that the absolute magnitude of strains in bearings with  $K_f = 500$  kN/mm are reduced compared to the strains in bearings with  $K_f = 10$  kN/mm. FEA results show that the variation of the vertical strains ( $\varepsilon_{zz}$ ) and their values at  $r/b = 0$  and  $r/b = 1/2$  are similar. However, at  $r/b = 5/6$  the absolute values of the vertical strain are observed to increase rapidly. This increase is more noticeable in bearings with lower shape factors.

For this particular set of bearings and at  $r/b = 0$  and  $r/b = 1/2$ , the minimum values of the radial strains in the first elastomer layers are observed to occur at the interface between the layer and the rigid supports. However, at  $r/b = 5/6$ , the radial strains increase and the maximum values in the first elastomer layers are observed to occur at the interface between the layer and the supports. This increase in the radial strains close to the edges is attributed to the lateral bugling of the elastomer layers that is significant at the edges.

FEA results shows that the variation of the pressure within the thickness of the elastomer layers is negligible, and the maximum difference between the values of the pressure along the height of the center elastomer layers is less than 2% in all the bearings considered in this study. For this reason, and in order to plot the variation of the pressure along the width of the bearings, the average pressure ( $p_{ave}$ ) in the center elastomer layers is calculated from the FEA results and is plotted in Fig. 2.14. The pressure values are normalized with respect to the mean vertical pressure ( $\bar{p}$ ). It can be seen from the figure that changing the values of  $K_f$  has negligible effect on the normalized pressure distribution in bearings with  $K_f \geq 50$  kN/mm.

Figure 2.15 compares the pressure distribution in the center elastomer layers obtained from FEA results with the values calculated using the PS and PA method considering rigid end effects (Eqs. 2.7 and 2.24), for bearings with  $K_f = 100$  kN/mm. It can be observed that the FEA results are in excellent agreement with the analytically predicted values. For bearings with  $S = 20$  and  $S = 30$ , the lines representing the predictions of the PA and the PS methods are nearly indistinguishable.

Shear strains (or shear stresses) that develop in the elastomer layers due to compression are especially important for design, where the sum of the maximum shear strain due to compression added to the maximum shear strain due to other loads should not exceed a certain limit relating to the elastomer's elongation-at-break limit [3]. Both in the PA and PS methods, the variations of the vertical displacements with respect to the vertical axis are neglected in calculating the shear strains. In other words, in calculating the shear strains, the horizontal planes within the elastomer layer are assumed to remain horizontal after applying the vertical load. The plots in Fig. 2.16 show the distribution of normalized shear strains  $\gamma_{rz}$  along the height of the first and center elastomer layers obtained from FEA and theory (Eqs. 2.9 and 2.25) in bearings with  $S = 5$ . The strains are compared at  $r/b = 1/2$  and  $r/b = 5/6$  and for the smallest and largest values of  $K_f$  considered in this study. A similar comparison is made in Fig. 2.17 for bearings with  $S = 30$ . The variation of the shear strains through the height of elastomer layers is found to be linear in all the bearings considered. The difference between the shear strains in the first and center elastomer layers decreases as the value of  $K_f$  increases. In bearings with  $K_f = 500$  kN/mm, there is practically no difference between the shear strains in the first and center elastomer layers, and the predictions of the PS and PA methods are in good agreement with the FEA results. In bearings with  $K_f = 10$  kN/mm, however, the FEA results show that there is a difference between the shear strain values in the first and center elastomer layers. The difference is considerable for bearing B30-10. In bearing B30-10, at  $r/b = 5/6$ , the difference between the values of the maximum shear strain in the first elastomer layer obtained from FEA results and the predictions of the PS and PA

methods is 36% and 9%, respectively. It should be noted that very near the edges of the elastomer layers ( $r/b \rightarrow 1$ ), the distribution of the shear strains along the height of elastomer layers obtained from FEA analysis is no longer linear and the theoretical methods are unable to predict the variation of shear strains along the layer. This is primarily attributed to the lateral bulging of the elastomer layers near the edges.

#### 2.4.5 Stress in Reinforcement

Figures 2.18 and 2.19 compare the normalized values of radial stress  $\sigma_{rr}$  and tangential stress  $\sigma_{\theta\theta}$  in the mid-height reinforcement layers in the bearings obtained from FEA. It can be observed from the figures that the peak stress values vary almost linearly with change in the thickness of the elastomer layer. Furthermore, Figs. 2.18 and 2.19 show that for each value of  $S$ , the values of  $\sigma_{rr}$  and  $\sigma_{\theta\theta}$  stresses are nearly equal when  $K_f \geq 50$  kN/mm.

Figure 2.20 compares FEA results to predictions from the PS and PA (considering rigid end effects) of the normalized  $\sigma_{rr}$  and  $\sigma_{\theta\theta}$  stresses in the mid-height reinforcement layers in the bearings with  $K_f = 100$  kN/mm. The theoretical stresses are obtained by calculating the internal forces per unit length in the reinforcing layers (Eqs. 2.5, 2.6, 2.21 and 2.22) and dividing them by  $t_f$ . The solid lines represent the FEA results and the dashed lines and the dotted lines represent the stress values predicted by the PA and PS methods, respectively. As can be seen from the figure, the values of peak normalized  $\sigma_{rr}$  and  $\sigma_{\theta\theta}$  stresses in the mid-height reinforcement layers are almost equal in each bearing. Good overall agreement is observed between the FEA results and the analytical solutions

for bearings with  $S = 5$  and  $S = 10$ . For  $S = 20$  and  $S = 30$ , the predictions of the PA and the PS are in excellent agreement with each other and with the FEA results.

## 2.5 Conclusion

This paper presents the results of a parametric 3D FEA investigation into the compressive behavior of circular elastomeric bearings with axially flexible reinforcement layers. The study examined a total of sixteen bearings with four different shape factor values ( $S = 5, 10, 20$  and  $30$ ) and four different reinforcement tensile stiffness values ( $K_f = 10, 50, 100$  and  $500$  kN/mm). The FEA results were compared with values from two analytical solutions for circular bearings in the literature: the *pressure solution* (PS) presented by Kelly and Calabrese [17] and the *pressure approach* (PA) presented by Tsai [20]. The pressure solution is the most common method for calculating the vertical stiffness of elastomeric bearings and is based on three assumptions: (i) Plane sections at the top and bottom of elastomer layers remain plane after applying the compression load; (ii) Points on a vertical line in the elastomer initially, form a parabola after loading; and (iii) The normal stress components in the elastomer are approximated by the pressure. The PA is similar to the pressure solution and is based only on the first two assumptions. For the pressure approach method, the monotonic loading and the rigid end boundary condition were considered.

FEA results showed that under a mean vertical pressure of  $\bar{p} = 2$  MPa and for the investigated bearings, initially horizontal planes in the elastomer layers remained almost horizontal after the application of the vertical load. Comparing the deformed shapes of

the elastomer layers with the predictions of the closed-form solutions showed that the assumed parabolic bulging of the elastomer layers in the analytical solutions is a satisfactory assumption.

When comparing the overall vertical stiffness of the bearings, the FEA results were in good agreement with the results from analytical solutions. The maximum difference between the FEA results and theory was found to be 13.5%, 10.6% ,and 3.3% for the PS, PA and the PA including end effects, respectively. The study concluded that the end effect could be ignored for bearings with large shape factors ( $S \geq 20$ ) or for bearings with  $K_f \geq 100$  kN/mm ( $K_f/Et \geq 1500$ ). For a fixed value of  $S$ , the radial and tangential stress distributions in the reinforcements were nearly unaffected for  $K_f \geq 50$  KN/mm. When comparing the stresses in the center reinforcement layer and the average pressure distribution in the center elastomer layer, the predictions of the analytical solutions agreed well with the FEA results. The predictions of the PA method considering end effects for the shear stresses in the center and top elastomer layer agreed well with FEA results.

When examining the effect of pressure on the compression stiffness, it was noted that, bearings with  $S \geq 20$  showed very low sensitivity to larger pressures while bearings with  $S = 5$  and  $S = 10$  showed a stiffening behavior under larger pressures. The flexibility of reinforcements was found to have negligible effect on the stiffening behavior.

## **2.6 Acknowledgments**

This research was carried out as part of the mandate of the Centre for Effective Design of Structures (CEDS) at McMaster University and is partially funded by the Ontario Ministry of Economic Development and Innovation and by the Natural Sciences and Engineering Research Council of Canada (NSERC). The authors also acknowledge MSC Software Corporation for their support.

## **2.7 References**

- [1] Tsai HC, Kelly JM. Bending stiffness of fiber-reinforced circular seismic isolators. *Journal of Engineering Mechanics* 2002;128(11):1150–1157.
- [2] Kelly JM. Seismic isolation systems for developing countries, *Earthquake Spectra* 2002; 18(3):385-406.
- [3] Kelly JM, Konstantinidis D. *Mechanics of rubber bearings for seismic and vibration isolation*. Wiley, Chichester, UK. 2011.
- [4] Kelly JM. Analysis of fiber-reinforced elastomeric isolators, *Journal of Seismology and Earthquake Engineering* 1999;2(1):19-34.
- [5] Toopchi-Nezhad H, Tait MJ, Drysdale RG. Testing and modeling of square carbon fiber-reinforced elastomeric seismic isolators, *Structural Control and Health Monitoring* 2007;15(6):876-900.
- [6] Toopchi-Nezhad H, Tait MJ, Drysdale RG. Lateral response evaluation of fiber-reinforced neoprene seismic isolators utilized in an unbonded application, *Journal of Structural Engineering* 2008;134(10):1627-1637.

- [7] Moon BY, Kang GJ, Kang BS, Kelly JM. Design and manufacturing of fiber-reinforced elastomeric isolator for seismic isolation, *Journal of Materials Processing Technology* 2002;130-131: 145-150.
- [8] Toopchi-Nezhad H, Tait MJ, Drysdale RG. A novel elastomeric base isolation system for seismic mitigation of low-rise buildings, *Proceedings of the 14<sup>th</sup> World Conference on Earthquake Engineering*, Beijing, 12-18 October 2008.
- [9] Toopchi-Nezhad H, Tait MJ, Drysdale RG. Simplified analysis of a low-rise building seismically isolated with stable unbonded fiber reinforced elastomeric isolators, *Canadian Journal of Civil Engineering* 2009;36(7):1182-1194.
- [10] Rocard Y. Note sur le calcul des propriétés élastiques des supports en caoutchouc adhérent, *Journal de Physique et de Radium* 1937;8:197-203.
- [11] Gent AN, Lindley PB. Compression of bonded rubber blocks, *Institution of Mechanical Engineers* 1959;173(3):111-122.
- [12] Gent AN, Meinecke EA. Compression, bending and shear of bonded rubber blocks, *Polymer Engineering and Science* 1970;10(1):48-53.
- [13] Lindley PB. Compression module for blocks of soft elastic material bonded to rigid end plates, *Journal of Strain Analysis* 1979;14(1):11–16.
- [14] Kelly JM. *Earthquake-resistant design with rubber*, Second Edition. Springer-Verlag, London, 1997.
- [15] Tsai HC, Kelly JM. Stiffness analysis of fiber-reinforced elastomeric isolators, *Pacific Earthquake Engineering Research Center, PEER, Berkeley, California*. 2001/5.

- [16] Tsai HC, Kelly JM. Stiffness analysis of fiber-reinforced rectangular isolators, *Journal of Engineering Mechanics* 2002;128(4):462-470.
- [17] Kelly JM, Calabrese A. *Mechanics of fiber reinforced bearings*. Pacific Earthquake Engineering Research Center, PEER, Berkeley, California, 2012/101.
- [18] Tsai HC, Lee C. Compressive stiffness of elastic layers bonded between rigid plates. *International Journal of Solids and Structures* 1998;35(23):3053–3069.
- [19] Tsai HC. Compression stiffness of infinite-strip bearings of laminated elastic material interleaving with flexible reinforcements, *International Journal of Solids and Structures* 2004;41(24):6647-6660.
- [20] Tsai HC. Compression stiffness of circular bearings of laminated elastic material interleaving with flexible reinforcements, *International Journal of Solids and Structures* 2006;46(11):3484-3497.
- [21] Pinarbasi S, Akyuz U, Mengi Y. A new formulation for the analysis of elastic layers bonded to rigid surfaces, *International Journal of Solids and Structures* 2006;43(14):4271-4296.
- [22] Pinarbasi S, Mengi Y, Akyuz U. Compression of solid and annular circular discs bonded to rigid surfaces, *International Journal of Solids and Structures* 2008;45(16):4543-4561.
- [23] Pinarbasi S, Mengi Y. Elastic layers bonded to flexible reinforcements, *International Journal of Solids and Structures* 2008;45(3): 794-820.
- [24] Pinarbasi S, Okay F. Compression of hollow-circular fiber-reinforced rubber bearings, *Structural Engineering and Mechanics* 2011; 38(3): 361-384.

- [25] Mordini A, Strauss A. An innovative earthquake isolation system using fibre reinforced rubber bearings, *Journal of Engineering Structures* 2008;30(10):2739-2751.
- [26] Kelly JM, Marsico MR. Stability and post-buckling behavior in nonbolted elastomeric isolators, *Seismic Isolation and Protection Systems* 2010;1(1):41-54.
- [27] Gerhaher U, Strauss A, Bergmeister K. Numerical modeling of elastomeric bearings in structural engineering, *Advances in Materials Sciences* 2011;11(3):51-63.
- [28] Toopchi-Nezhad H, Tait MJ, Drysdale RG. Bonded versus unbonded strip fiber reinforced elastomeric isolators: finite element analysis, *Composite Structures* 2011;93(2):850-859.
- [29] Toopchi-Nezhad H, Tait MJ, Drysdale RG. Influence of thickness of individual elastomer layers (first shape factor) on the response of unbonded fiber-reinforced elastomeric bearings, *Journal of Composite Materials* 2012, Published online at Dec. 4<sup>th</sup>, 2012.
- [30] Toopchi-Nezhad H, Tait MJ, Drysdale RG. Stiffness analysis of fiber-reinforced rubber isolators under compressive loads: A finite element approach, *Proceedings of the 9<sup>th</sup> US National and 10<sup>th</sup> Canadian Conference on Earthquake Engineering*, Toronto, 25-29 July 2010.
- [31] MSC Marc. Theory and user information, vol. A. Santa Ana: MSC Software Corporation; 2011.

Table 2.1. Bearing dimensions and properties

Bearing	$S$	$t$ (mm)	$n$	$K_f$ (kN/mm)	$K_f/Et$
B5-10				10	139
B5-50	5	30	7	50	694
B5-100				100	1389
B5-500				500	6944
B10-10				10	278
B10-50	10	15	14	50	1389
B10-100				100	2778
B10-500				500	13889
B20-10				10	556
B20-50	20	7.5	28	50	2778
B20-100				100	5556
B20-500				500	27778
B30-10				10	833
B30-50	30	5	42	50	4167
B30-100				100	8333
B30-500				500	41667

Table 2.2. Vertical stiffness values obtained from FEA and analytical solutions

Bearing	FEA	Pressure Solution, Monotonic Loading		Pressure Approach, Monotonic Loading		Pressure Approach, Rigid End Effects	
	$K_v$ (MN/mm)	$K_v$ (MN/mm)	Difference with FEA (%)	$K_v$ (MN/mm)	Difference with FEA (%)	$K_v$ (MN/mm)	Difference with FEA (%)
B5-10	107.1	92.6	13.5	95.7	10.6	104.7	2.2
B5-50	143.7	133.1	7.4	136.2	5.2	139.6	2.9
B5-100	150.5	140.9	6.4	144.0	4.3	145.9	3.1
B5-500	156.4	147.8	5.5	150.9	3.5	151.3	3.3
B10-10	266.1	246.0	7.5	249.1	6.4	269.6	1.3
B10-50	423.5	408.5	3.5	411.4	2.9	422.0	0.4
B10-100	458.8	445.8	2.8	448.7	2.2	454.9	0.9
B10-500	492.0	481.0	2.2	483.9	1.6	485.3	1.4
B20-10	567.0	541.2	4.6	544.0	4.1	573.8	1.2
B20-50	962.6	938.8	2.5	941.3	2.2	958.5	0.4
B20-100	1058.0	1035.3	2.1	1037.8	1.9	1048.2	0.9
B20-500	1150.0	1128.5	1.9	1131.0	1.7	1133.4	1.4
B30-10	809.0	783.7	3.1	786.4	2.8	816.6	0.9
B30-50	1324.3	1303.2	1.6	1305.5	1.4	1321.7	0.2
B30-100	1442.5	1422.5	1.4	1424.8	1.2	1434.4	0.6
B30-500	1553.7	1535.4	1.2	1537.6	1.0	1539.9	0.9

Table 2.3. Comparison of  $E_c^1/E_c^{\text{mid}}$  and  $E_c^2/E_c^{\text{mid}}$  obtained from FEA and the pressure approach

Bearing	Finite Element		Pressure Approach (Eq. 2.15)	
	1 <sup>st</sup> layer	2 <sup>nd</sup> layer	1 <sup>st</sup> layer	2 <sup>nd</sup> layer
B5-10	1.344	1.014	1.227	1.079
B5-50	1.080	1.001	1.057	1.022
B5-100	1.041	1.000	1.029	1.012
B5-500	1.008	1.000	1.006	1.002
B10-10	1.524	1.036	1.323	1.122
B10-50	1.127	1.003	1.089	1.038
B10-100	1.065	1.001	1.047	1.020
B10-500	1.013	1.000	1.010	1.004
B20-10	1.600	1.074	1.360	1.145
B20-50	1.141	1.006	1.102	1.046
B20-100	1.072	1.002	1.054	1.025
B20-500	1.015	1.000	1.011	1.005
B30-10	1.557	1.098	1.334	1.139
B30-50	1.121	1.008	1.091	1.042
B30-100	1.061	1.002	1.048	1.023
B30-500	1.014	1.002	1.010	1.005

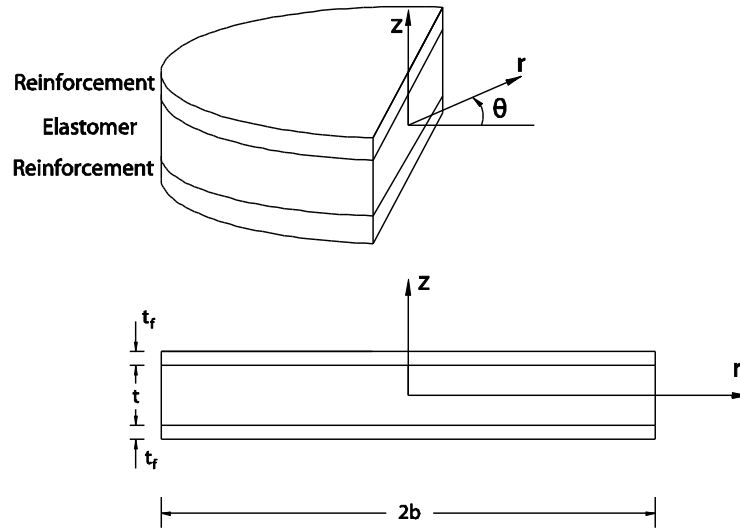


Figure 2.1. A circular elastomeric pad bonded to flexible reinforcements

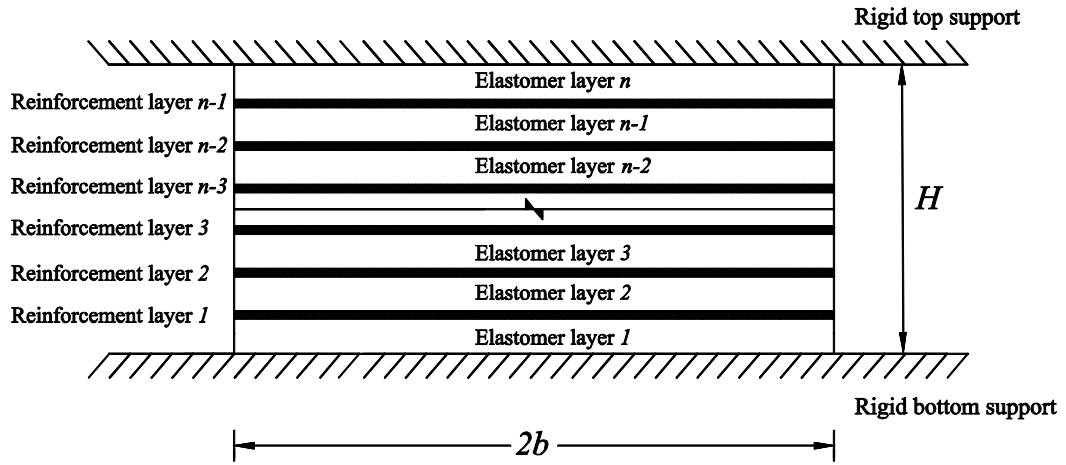


Figure 2.2. Bearing consisting of  $n$  elastic layers bonded to rigid supports

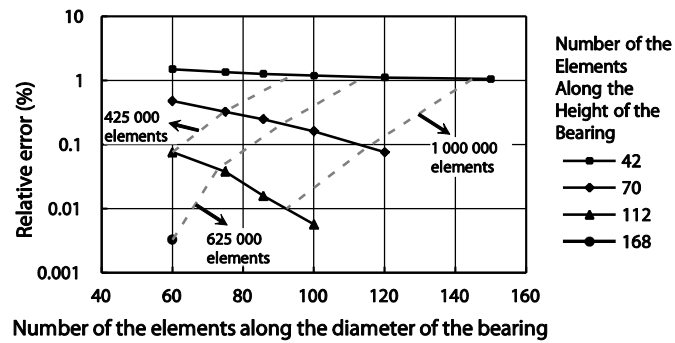


Figure 2.3. Effect of element size on the modeling error in B5-10 bearing

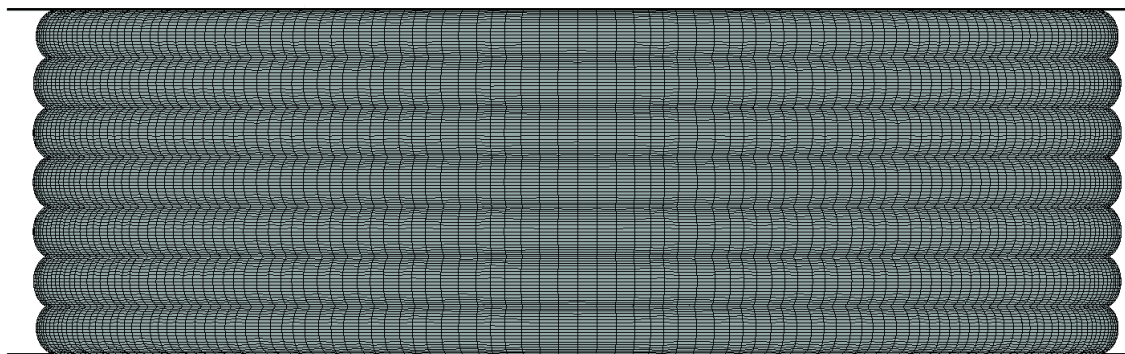


Figure 2.4. Deformed shape of bearing B5-10 under  $\bar{p} = 2$  MPa

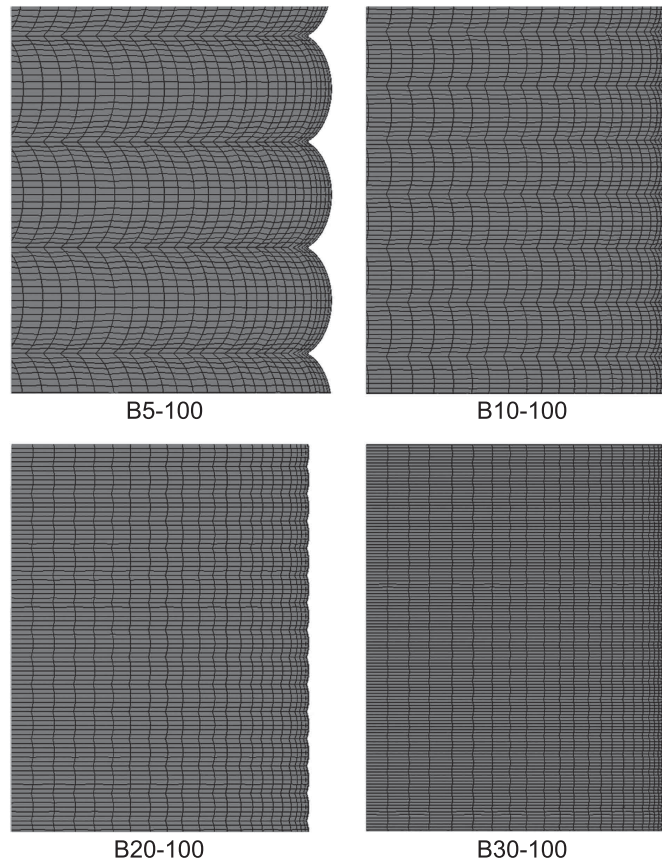


Figure 2.5. Deformed shapes of bearings with  $K_f = 100$  kN/mm under  $\bar{p} = 2$  MPa

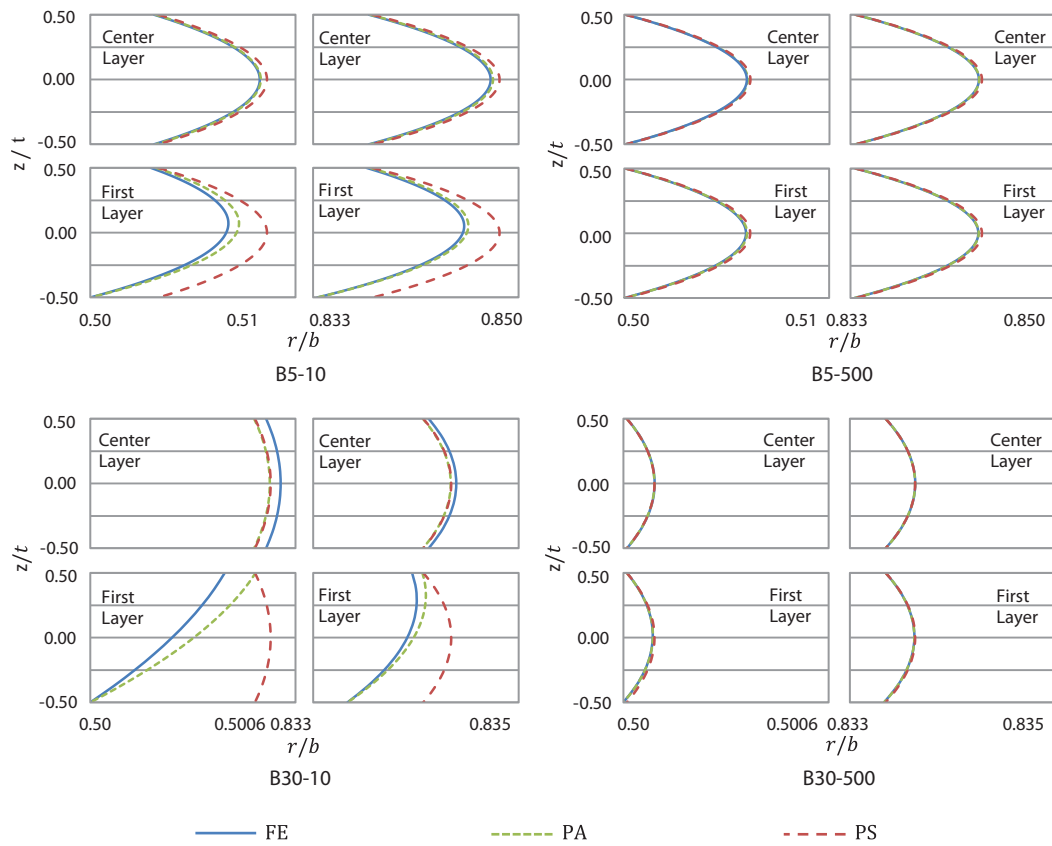


Figure 2.6. Comparison of the deformed shapes of the first and center elastomer layers at  $r/b = 1/2$  and  $r/b = 5/6$  obtained from FE analysis, PA considering rigid end effects and PS under  $\bar{p} = 2$  MPa

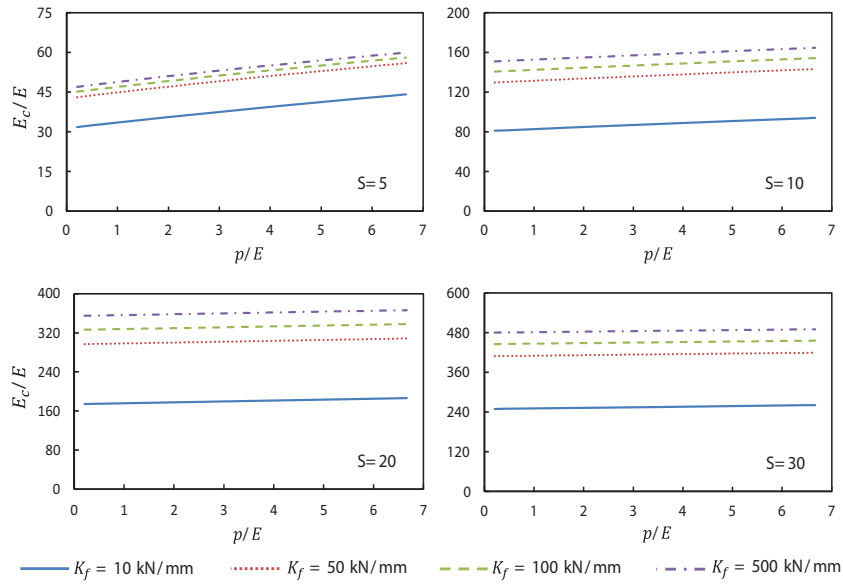


Figure 2.7. Variation of  $E_c/E$  obtained from FE analysis at different load levels in bearings

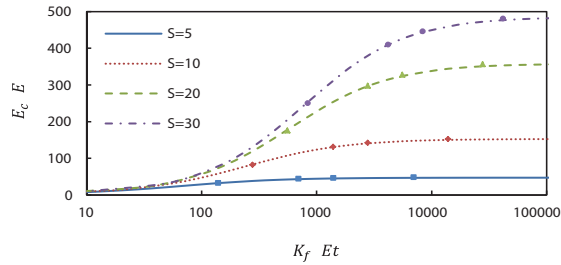


Figure 2.8.  $E_c/E$  as a function of  $K_f/Et$ , as computed using the PA including rigid end effects and FEA

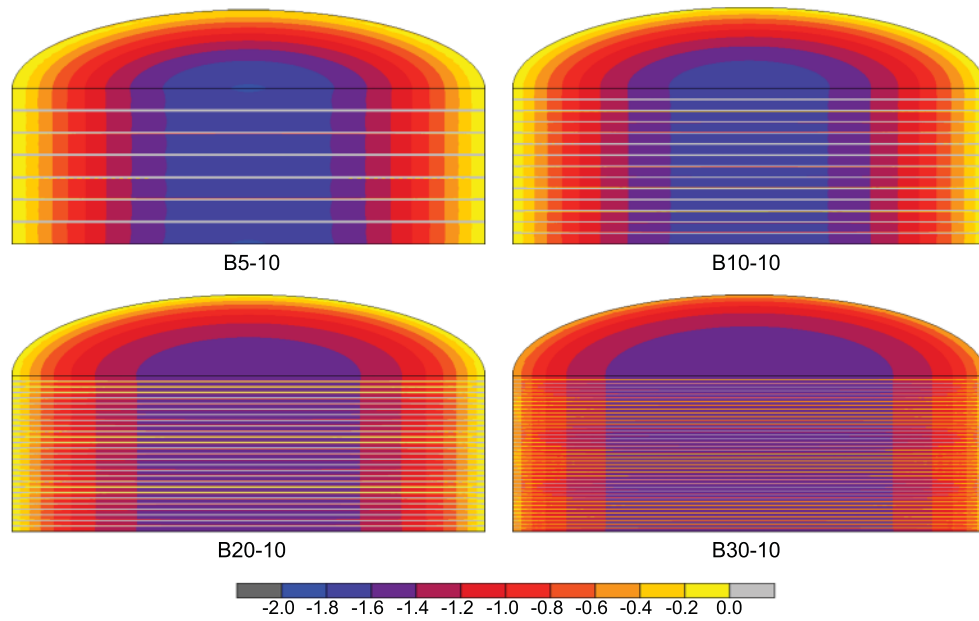


Figure 2.9. Contours of normalized  $\sigma_{rr}$  stress in bearings with  $K_f = 10$  kN/mm under  $\bar{p} = 2$  MPa

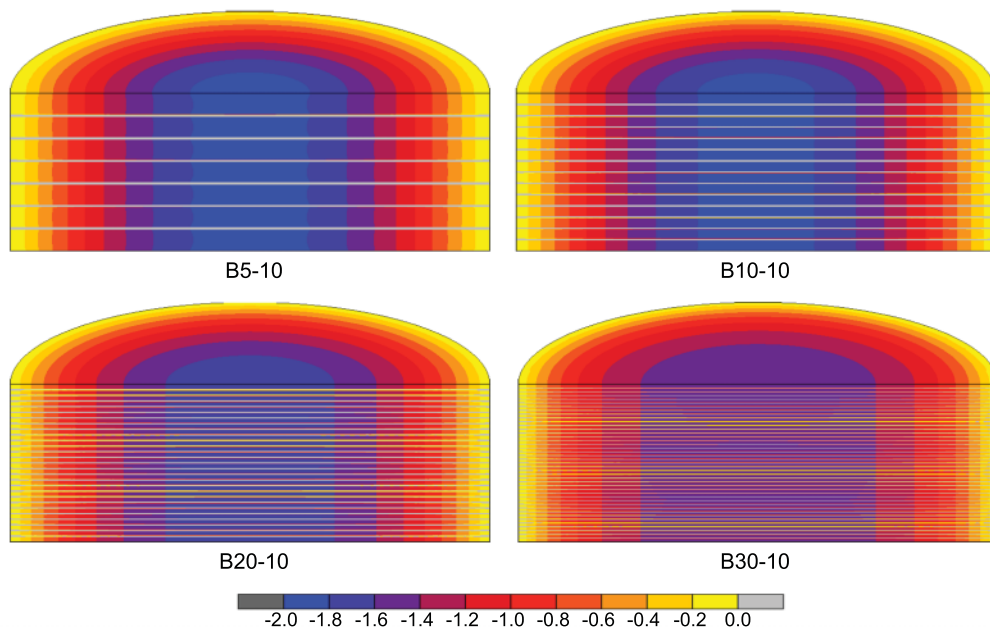


Figure 2.10. Contours of normalized  $\sigma_{rr}$  stress in bearings with  $K_f = 500$  kN/mm under  $\bar{p} = 2$  MPa

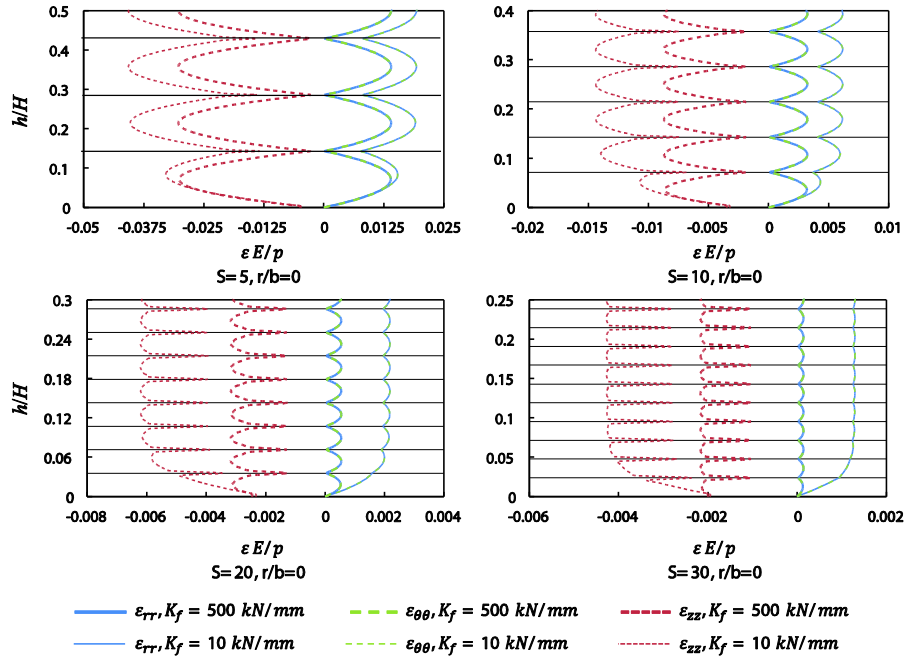


Figure 2.11. Variation of the normalized strains through the elastomer layers obtained from FEA at  $r/b = 0$

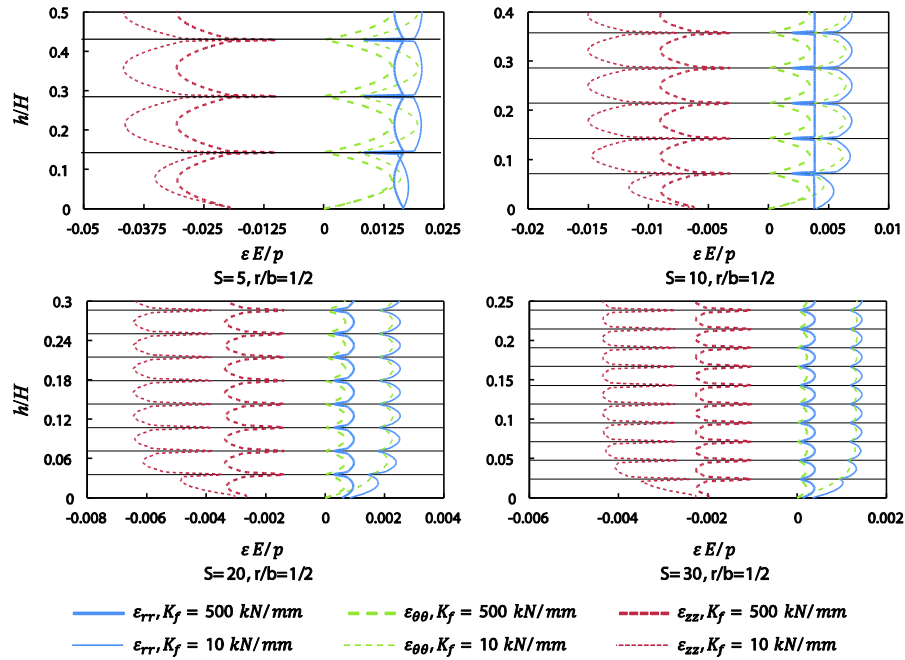


Figure 2.12. Variation of the normalized strains through the elastomer layers obtained from FEA at  $r/b = 1/2$

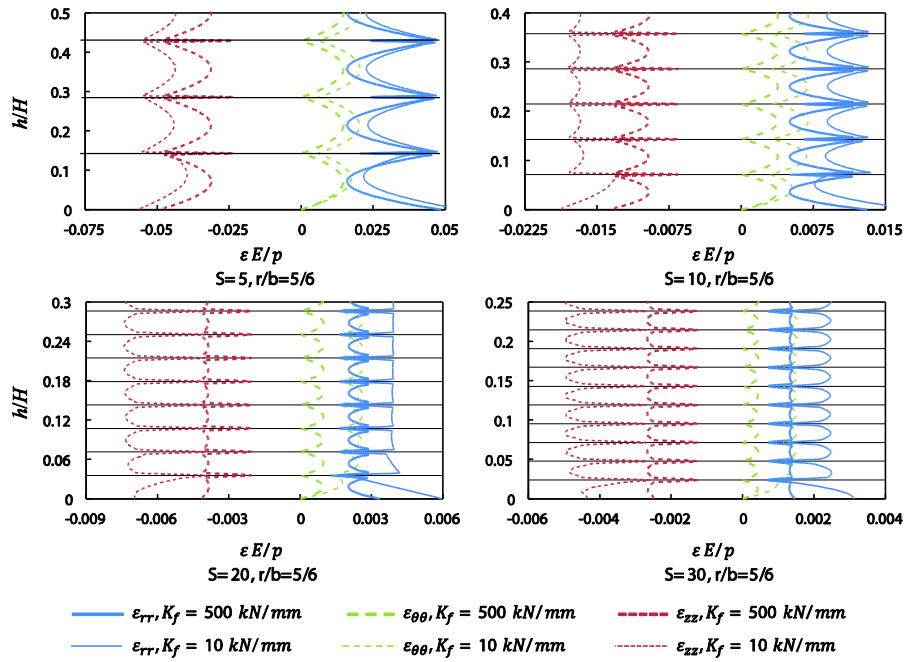


Figure 2.13. Variation of the normalized strains through the elastomer layers obtained from FEA at  $r/b = 5/6$

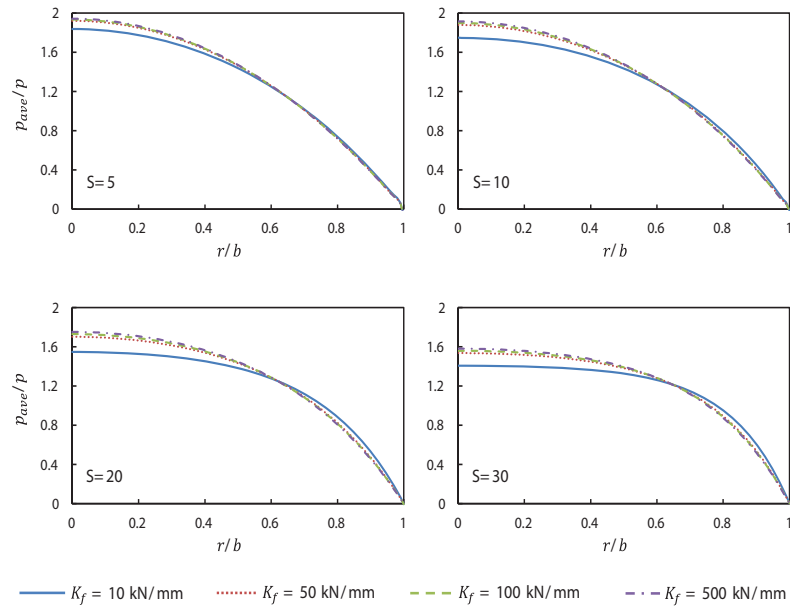


Figure 2.14. Variation of normalized average pressure ( $p_{ave}/\bar{p}$ ) in the centre elastomer layers obtained from FEA results

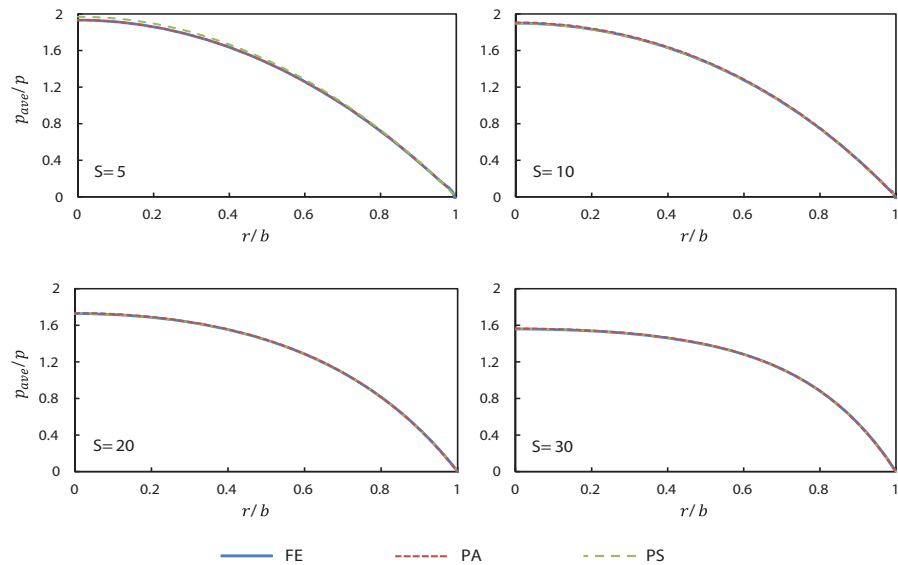


Figure 2.15. Comparison of normalized average pressure ( $p_{ave}/\bar{p}$ ) in the centre elastomer layers for bearings with  $K_f = 100$  kN/mm obtained from FEA, PS and PA considering rigid end effects

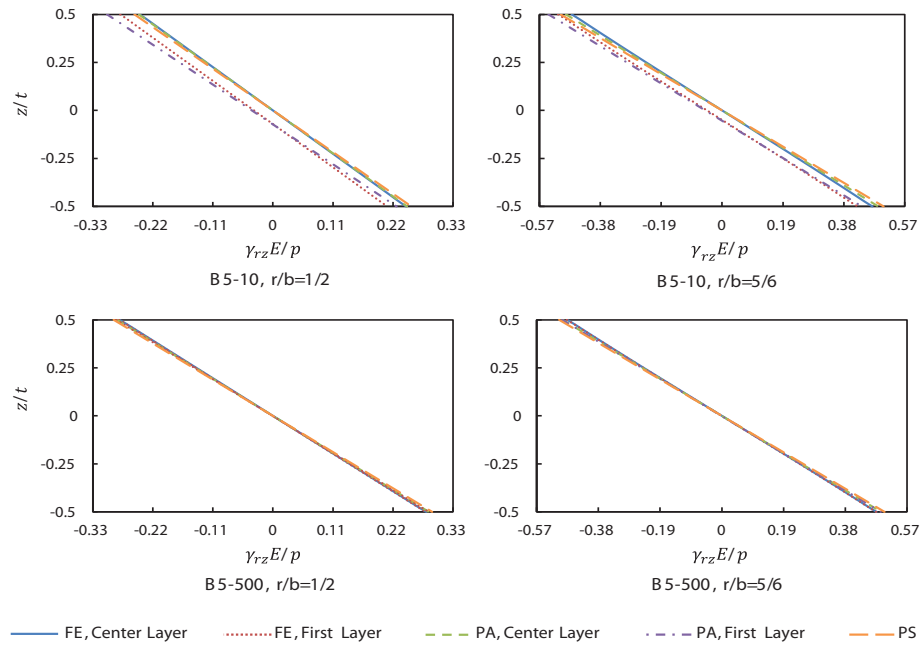


Figure 2.16. Variation of normalized shear strains ( $\gamma_{rz}E/\bar{p}$ ) in the first and center elastomer layers obtained from FEA, PS and PA considering rigid end effects for bearings with  $S = 5$

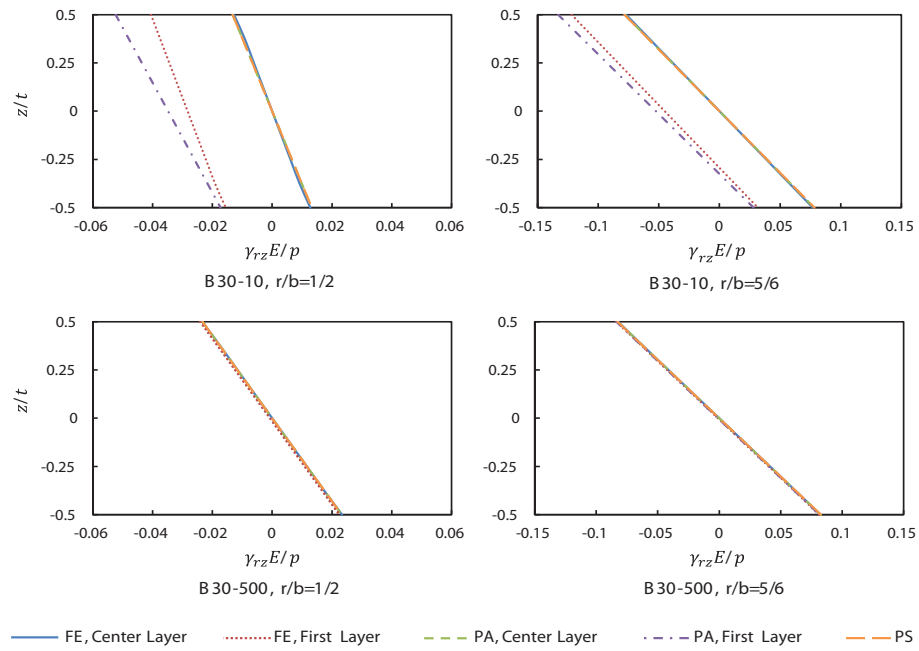


Figure 2.17. Variation of normalized shear strains ( $\gamma_{rz}E/\bar{p}$ ) in the first and center elastomer layers obtained from FEA, PS and PA considering rigid end effects for bearings with  $S = 30$

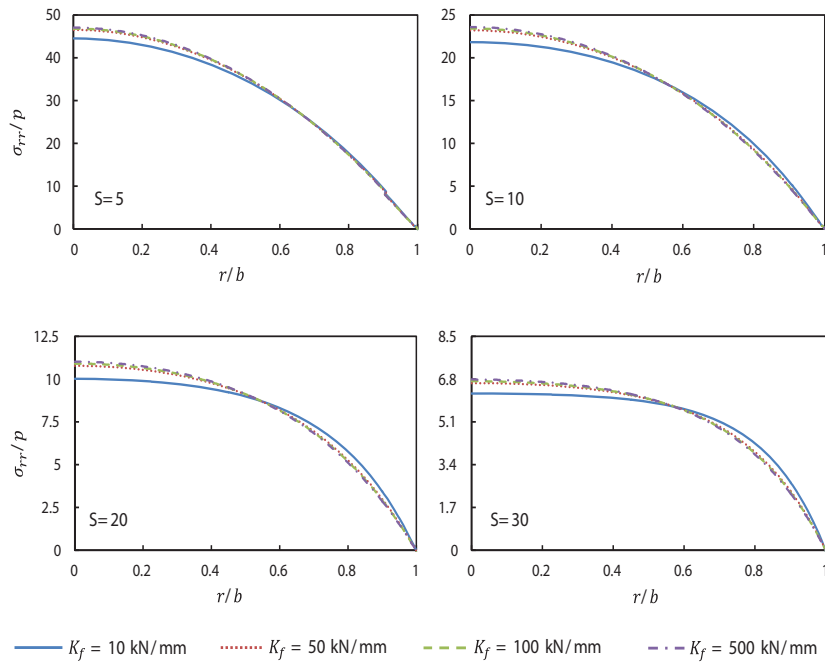


Figure 2.18. Variation of normalized  $\sigma_{rr}$  stress in center reinforcement layers obtained from FEA

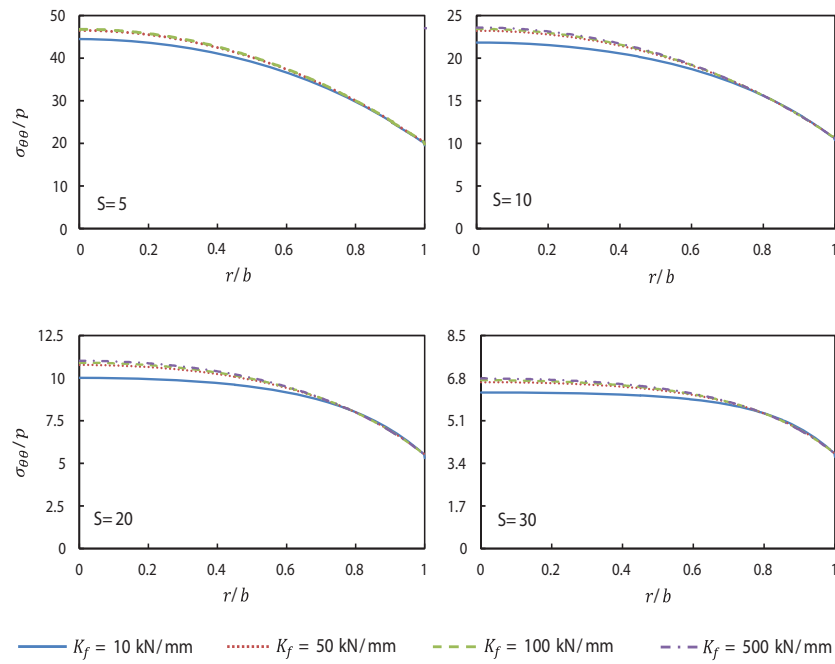


Figure 2.19. Variation of normalized  $\sigma_{\theta\theta}$  stress in center reinforcement layers obtained from FEA

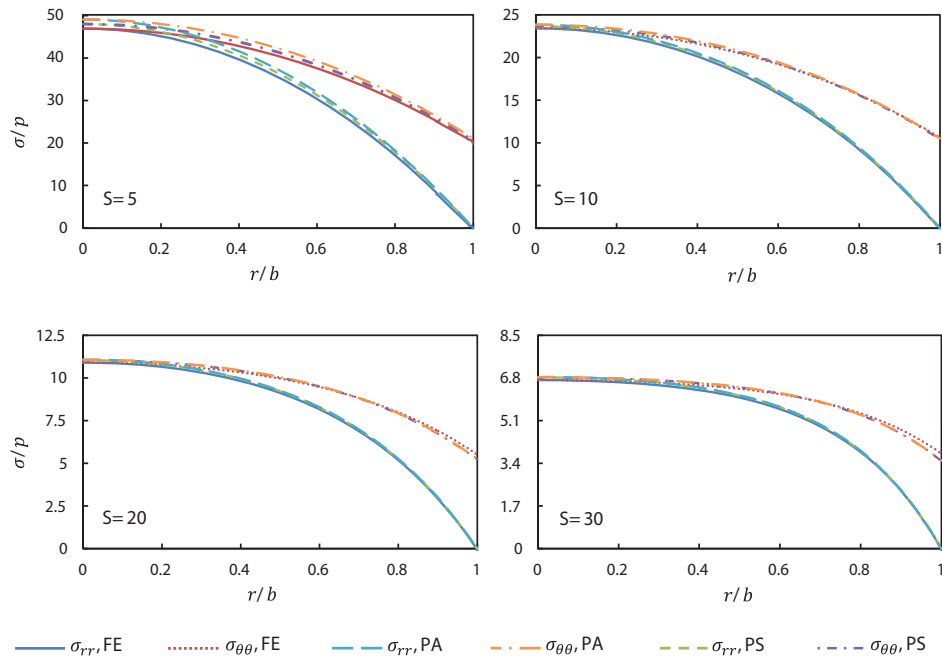


Figure 2.20. Comparison of normalized  $\sigma_{rr}$  and  $\sigma_{\theta\theta}$  in center reinforcement layers obtained from FEA, PS and PA considering rigid end effects

### **Chapter 3: Finite Element Analysis of Unbonded Square Fiber-Reinforced Elastomeric Isolators (FREIs) under Lateral Loading in Different Directions**

#### **Abstract**

Compared to conventional elastomeric bearings, fiber-reinforced elastomeric isolators (FREIs) are expected to cost much less and be easier to install, particularly when unbonded isolators are utilized. Due to the complex lateral response of unbonded FREIs, only a limited number of analytical studies are available in the literature. In addition, most of these analytical studies are based on a number of simplifying assumptions, applicable only to a few basic geometries. In this paper, three-dimensional finite element analysis (FEA) is carried out to investigate the lateral response of square FREIs, having aspect ratios of 1.9, 2.6 and 2.9, when loaded in different directions. Since square isolators are not axisymmetric, variations in lateral response can be expected to occur when subjected to different loading directions. The finite element (FE) models are validated using experimental test results for bearings loaded at  $0^\circ$  and are subsequently employed to analyze the lateral response characteristics of the bearings when loaded at  $15^\circ$ ,  $30^\circ$  and  $45^\circ$ . The results show that in general, the effective lateral stiffness of the bearings increases as the loading direction changes from  $0^\circ$  to  $45^\circ$ . In addition, as the aspect ratio decreases, the sensitivity of the lateral response to the loading direction increases.

### **3.1 Introduction**

Seismic isolation is a well-known earthquake mitigation technique, which lowers the seismic demand on a structure by shifting the natural period of vibration of the structure beyond the high-energy period range of earthquakes. As a result, the seismic energy transferred to the structure is significantly reduced. The application of seismic isolation in North America has been limited almost entirely to expensive or high importance (post-disaster) structures, e.g., hospitals and emergency centers. This limited use is largely due to the high material, manufacturing and installation costs associated with conventional seismic isolators. It is expected that the use of seismic isolators can be extended to smaller structures and typical residential (normal importance) buildings if the weight and cost of the isolators are reduced [1].

Steel-reinforced elastomeric isolators (SREIs), which are the most common type of seismic isolators in use, are laminated rubber bearings composed of layers of elastomer interleaved with steel reinforcement shims (approximately 3mm thick). Typically, steel end plates (25 mm thick, or more) are bonded to the top and bottom surfaces of the bearing. These steel plates are used to install the isolator and to connect it to the foundation and superstructure. The steel plates as well as the reinforcing steel shims make SREIs heavy. Furthermore, manufacturing of SREIs involves a labor-intensive process [2], making them expensive. Kelly [1] suggested that the weight of the SREIs can be reduced by replacing the steel shims with other materials having the same order of elastic stiffness as steel, e.g., fiber-reinforced polymer (FRP) materials. The manufacturing process of the isolators can also be simplified when using fiber materials

instead of steel along with the elimination of the top and bottom steel end plates. Fiber-reinforced elastomeric isolators (FREIs) can be installed by simply placing them between the superstructure and foundation. In this case, the shear force from the superstructure is transferred to the bearing and then the foundation through the friction that develops along the interfaces between the bearing and its supports. Test results [1, 3-9] have shown that it is possible to obtain adequate vertical stiffness and horizontal flexibility with FREIs.

Steel shims in SREIs are usually assumed rigid both in extension and bending. However, the fiber layers in FREIs are more flexible in extension and have negligible flexural rigidity. Due to the low flexural rigidity of the fibers and absence of steel end plates, FREIs exhibit a unique rollover deformation where the upper and lower contact surfaces of the isolator separate from the supports when the isolator is loaded laterally. This type of deformation is found to increase the efficiency of the isolator by providing further lateral flexibility [10]. The stress demand on both the rubber and reinforcement layers is also found to be lower in unbonded FREIs [10]. This lower stress demand makes it possible to use a simpler manufacturing process [10, 11].

The vertical response of FREIs has been investigated through a number of analytical and FEA studies [1-3, 8, 9, 12-20]. The lateral response of FREIs is complex and few closed-form solutions [2, 11, 21, 22] currently exist in the literature. In addition, these solutions are based on simplified assumptions (e.g., the free surface of the rollover portion is stress free, the fiber reinforcement is infinitely flexible, the magnitude of the vertical load has no effect on the lateral response). One of the benefits of using fiber reinforcement instead of steel is that the bearings can be manufactured in a large

rectangular sheet, and individual bearings can subsequently be cut to the required shape and size [1]. Most researchers [3, 5, 6, 17, 23] have preferred rectangular-shaped FREIs, either long strip or square, over other shapes. It is generally assumed that the isolation system will be isotropic when using symmetrically shaped isolators (circular or square) [1]. However, unlike circular or annular shaped isolators which are axisymmetric, a different lateral response can be expected from square FREIs when the direction of the lateral load is not parallel to the principal axes.

In this paper, finite element analysis (FEA) is employed to numerically investigate the lateral response characteristics of FREIs. Due to the near incompressibility of the elastomer material, large displacements, and large strains associated with FREIs, FEA of FREIs requires high computational effort. In the literature, there are several FEA studies focused on the lateral response of unbonded FREIs. These studies have either been limited to 2D analyses [10, 19, 24] or if 3D analysis has been conducted, it has only considered the behavior of the isolator when loaded parallel to its width [23, 25, 26].

This paper investigates the lateral response of square FREIs loaded in different directions. Three square FREIs, from a previous study [5], are investigated using 3D FEA. The finite element (FE) models are evaluated using experimental data obtained from lateral cyclic tests where the load was applied parallel to the width of the bearings ( $0^\circ$ ), as shown in Fig. 3.1. FE models are subsequently used to load each bearing at directions of  $15^\circ$ ,  $30^\circ$  and  $45^\circ$  (Fig. 3.1). The behavior of the unbonded square FREIs loaded in these directions is investigated using FEA results, including the lateral load-

displacement response, and the stresses and strains in the elastomer and reinforcement layers.

### 3.2 Lateral Response of Unbonded FREIs

Figure 3.2 shows a typical lateral load-displacement curve of a FREI loaded in the  $0^\circ$  direction. Under small lateral displacements, the lateral stiffness of the bearing is nearly linear, up to a displacement level at which the upper and lower contact surfaces of the bearing start to roll off the supports. This point is denoted by  $D_r$ . As the displacement is further increased, which induces rollover, the lateral stiffness of the bearing is observed to decrease because of the reduction in the effective shear area. At a certain displacement, portions of the originally vertical faces of elastomer layers adjacent to the top and bottom layers contact the supports. The displacement at which this contact initiates is denoted by  $D_c$ . With additional increase in displacement, an increased number of elastomer layers make contact with the supports. The displacement at which the originally vertical faces of all the elastomer layers fully contact the supports is denoted by  $D_f$ . When the displacement of the bearing is in the  $D_c$  to  $D_f$  range, the lateral response of the bearing is influenced by two things: a reduction in the effective lateral stiffness of the bearing due to rollover, and an increase in the lateral stiffness due to the initiation of contact between the vertical faces of the elastomer layers with the support surfaces. Thus, the  $D_c$  to  $D_f$  range is a transition region, and at a certain displacement within this range, the increase in the effective lateral stiffness of the bearing due to contact exceeds the decrease in the stiffness due to rollover, and a hardening behavior is observed to occur. The displacement

at which this hardening occurs is denoted by  $D_h$ . This hardening behavior observed in unbonded FREIs is considered to be an advantageous characteristic since it can limit the displacement of the isolation system in beyond-design-basis seismic events [5].

According to ASCE-7 [27], a seismic isolator should maintain positive incremental lateral force resisting capability within the range of the considered lateral displacements. In other words, the tangent lateral stiffness of a stable seismic isolator is positive throughout the displacement range. Toopchi-Nezhad et al. [5] showed through experimental tests that the width-to-height ratio (defined as aspect ratio) of a FREI plays an important role on the overall stability of the isolator. When the aspect ratio is lower than a certain value, in the  $D_c$  to  $D_h$  region, the increase in the lateral stiffness of the bearing due to the contact of elastomer layers and the supports does not exceed the decrease in the stiffness due to rollover, and thus the tangent lateral stiffness becomes negative.

It will be shown later that the lateral response characteristics of a FREI are different when the loading is in a direction other than  $0^\circ$ . Although the definitions of the displacement levels  $D_r$ ,  $D_c$ ,  $D_h$  and  $D_f$ , given in Fig. 3.2 are based on the lateral response of a FREI loaded in the  $0^\circ$  direction, they will also be used to describe the lateral response characteristics of the bearings in other loading directions.

### 3.3 Unbonded FREIs

Three square FREIs, with properties matching bearings manufactured and tested under pure compression and under combined compression and shear by Toopchi-Nezhad

et al. [5], were investigated in this study. The bearings had a width of 200 mm with overall heights of  $h = 105, 78$  and  $68$  mm. The shape factor,  $S$ , defined as the total loaded area of one elastomer layer to the load-free area of the layer, was 10.6, and the aspect ratios of the three bearings were 1.9, 2.6 and 2.9. The bearings manufactured and tested by Toopchi-Nezhad et al. [5] used a soft compound of natural gum rubber for the elastomer and were reinforced with bi-directional carbon fiber fabric. The shear modulus of the rubber was calculated to be  $G = 0.5$  MPa from the shear tests on the bearings conducted at  $u/t_r = 0.25$ , where  $u$  is the lateral displacement, and  $t_r$  is the total thickness of rubber layers in the bearing. The elastic modulus of the carbon fiber composite was  $E_f = 23$  GPa, obtained from uniaxial tension tests. Table 3.1 shows the properties of the bearings considered in this study.  $t_f$  is the thickness of fiber reinforcement layers,  $n$  is the number of rubber layers, and  $t$  is the thickness of an individual rubber layer.

### 3.4 FE Modeling

The FEA was carried out using MSC Marc [28], a commercially available general purpose finite element program. Figure 3.3 shows the FE model of bearing B200X78. The dimensions of the brick elements used to model the elastomer layers in the bearings were  $4\text{mm} \times 4\text{mm} \times 1.2\text{mm}$ . All the analyses were performed in 3D using the Updated Lagrangian (UL) formulation. In this formulation, the reference configuration is updated with the current known deformed configuration and is taken as an initial state for the

subsequent configuration. The stress in the UL formulation is Cauchy stress (also known as true stress), calculated based on the current deformed configuration.

The compressible neo-Hookean hyperelastic constitutive model and a linear-elastic isotropic material model were used to model the material properties of elastomer and fiber-reinforcement layers, respectively. Nine-node hexahedron first-order isoparametric elements were used to model the elastomer layers. The fiber reinforcement layers were modeled using four-node isoparametric quadrilateral membrane elements with no bending stiffness. The contact between the bearings and the loading plates were defined so that no tension reaction developed, allowing the nodal points of the elastomer layer elements to detach from the top and bottom supports when the normal compression stress reached zero.

In order to match the 1.6 MPa average vertical stress applied to the bearings in the experimental study, a vertical load of  $P = 64$  kN was applied and held constant while the bearings were subjected to a monotonically increasing lateral displacement in one of four directions ( $0^\circ$ ,  $15^\circ$ ,  $30^\circ$  and  $45^\circ$ ), as shown in Fig. 3.1. The maximum target displacement for all bearings was  $u/t_r = 2.00$ .

### 3.5 FE Model Validation

Figure 3.4 shows the normalized lateral load-displacement relationships obtained from experimental tests and FEA results for the bearings. The lateral force,  $F$ , is normalized by  $GA$ , where  $A$  is the plan area of the undeformed bearing. Good agreement is observed between the experimental and FEA results. For all three bearings, the

effective lateral stiffness decreases as the displacement of the bearings is increased, up to a point beyond which the lateral stiffness increases as a result of the contact between the originally vertical faces of the bearings with the supports. It is important for the FE model to be able to capture this hardening behavior observed in FREIs, as this beneficial characteristic limits the maximum isolation system displacement during, for example, a beyond-design-basis earthquake event. As seen in Fig. 3.4, the hardening in the lateral load displacement response is predicted with fair accuracy by the FEA.

The reduction in the effective lateral stiffness of the FREIs results in an increase in the base isolated period of the structure and can increase the efficiency of the isolators [5]. The amount of reduction in the effective lateral stiffness is higher in bearings with lower aspect ratios. As can be seen in Fig. 3.4, the tangent lateral stiffness in bearing B200X105 with an aspect ratio of 1.9 becomes negative and the bearing does not exhibit stable behavior. However, bearings B200X78 and B200X68, with aspect ratios of 2.6 and 2.9 respectively, perform in a stable manner. These bearings are defined as stable unbonded fiber reinforced elastomeric isolators (SU-FREIs) [5]. According to the FEA results, the normalized lateral displacement at which all the elastomer layers contact the support plates,  $D_f/t_r$ , is 2.00, 1.99 and 1.96 in bearings B200X68, B200X78 and B200X105, respectively. These values are in agreement with those observed during the experimental testing where  $D_f$  was estimated to occur at approximately the  $u/t_r = 2.00$  cycle. The displacement values  $D_r$ ,  $D_c$ ,  $D_h$  and  $D_f$ , normalized with respect to  $t_r$ , for the bearings obtained from FEA results are presented in Table 3.2.

The validation of MSC Marc presented herein together with the validation presented in other studies [10, 25] provides confidence in its use to model the behavior of square FREIS loaded in different directions.

### 3.6 Lateral Response in Different Directions

#### 3.6.1 Deformed Shapes

Figures 3.5 to 3.8 show the deformed shapes of bearing B200X78 obtained from FEA when displaced at  $0^\circ$  (Fig. 3.5),  $15^\circ$  (Fig. 3.6),  $30^\circ$  (Fig. 3.7) and  $45^\circ$  (Fig. 3.8) directions and at  $u/t_r = 0, 0.75, 1.50$  and  $2.00$ . A comparison between the deformed shapes for  $u/t_r = 0.75$  in different loading directions shows that as the loading direction changes from  $0^\circ$  to  $45^\circ$ , the portion of the bearing that experiences rollover decreases, thus increasing the effective shear area. A similar conclusion can be made by comparing the deformed shapes of the bearing at  $u/t_r = 1.50$ , although due to the complexity of the deformed shapes, distinguishing the rollover portion of the bearing loaded at  $30^\circ$  and  $45^\circ$  is not as obvious. At  $u/t_r = 2.00$ , some parts of the rollover portions of the bearing are in contact with the supports, which increases the lateral stiffness of the bearing. It can be seen in Figures 3.5 to 3.8 that as the direction of the loading changes from  $0^\circ$  to  $45^\circ$ , the rollover portion of the bearing that is in contact with the support surfaces is reduced. This change in volume of the rollover portions of the bearing that is in contact with the supports results in different tangent stiffness values beyond the displacement level  $D_h$  and will be discussed later.

### 3.6.2 Load-Displacement Relationships

Figure 3.9 compares the normalized lateral load-displacement curves of the bearings obtained in different loading directions. It can be seen from the figure that as the aspect ratio of the bearing increases, the lateral response of the bearing becomes less sensitive to the loading direction. The maximum difference between the lateral forces obtained at  $45^\circ$  with the lateral force obtained at  $0^\circ$  in bearing B200X105 is found to be 11.4% and 63.3% at  $u/t_r = 0.75$  and  $1.50$ , respectively. In bearing B200X78, the difference between the lateral forces is 5.7% and 22.7% at the same  $u/t_r$  values.

The lateral response of each bearing under different loading directions can be divided into two stages. In the first stage, the increase in the effective shear area as the loading direction changes from  $0^\circ$  to  $45^\circ$  results in higher stiffness at any given displacement. This stage starts at zero displacement and extends up to  $u/t_r = 1.65$ ,  $1.69$  and  $1.73$  in bearings B200X105, B200X78 and B200X68, respectively. During the second stage, the stiffness of the bearings is affected by the contact between the originally vertical faces of the bearing. The increase in the effective stiffness due to this contact is reduced when the rollover portion of the bearing is smaller. Thus, in the second stage, the effective lateral stiffness of each bearing loaded at  $0^\circ$  and  $15^\circ$  exceeds the effective stiffness obtained at  $30^\circ$  and  $45^\circ$ . The trend in relative stiffness between the  $0^\circ$  and  $45^\circ$  results from FEA is in general agreement with experimental results for bearings B200X68 and B200X78 [5].

It can be observed from Fig. 3.9 that all the bearings exhibited a hardening behavior for  $u/t_r > 1.50$ . However, the normalized displacement at which this hardening occurs,

$D_h/t_r$ , is affected by the loading direction. In all the bearings,  $D_h/t_r$  is increased with an increase in the loading direction from  $0^\circ$  to  $45^\circ$ . The rate of increase in the effective stiffness beyond  $D_h/t_r$  was also affected by the change in the loading direction. In all the bearings and when loading at  $0^\circ$ , the tangent lateral stiffness at  $D_h/t_r$  is dramatically increased. As the loading direction is increased to  $45^\circ$ , the increase in the tangent stiffness at  $D_h/t_r$  is less pronounced.

It can be observed from Fig. 3.9 that the tangent lateral stiffness of bearing B200X105 at  $0^\circ$  and  $15^\circ$  becomes negative and thus the bearing does not exhibit a stable lateral response for these two loading directions. At  $30^\circ$  and  $45^\circ$  however, the bearing exhibits stable rollover behavior. This change in the lateral response of the bearing B200X105 at  $30^\circ$  and  $45^\circ$  is attributed to the reduction in the rollover portion of the bearing when loaded in these directions.

Table 3.3 compares the values of the effective stiffness of the bearings, normalized by  $GA/t_r$ , given at  $u/t_r$  increments of 0.25. For all the bearings, the normalized effective stiffness increases with an increase in the aspect ratio of the bearing. The only exception is bearing B200X78 when loaded in the  $0^\circ$  direction at  $u/t_r = 1.75$ , where the effective normalized lateral stiffness (0.544) is 3% higher than that of bearing B200X68 (0.529). At  $0^\circ$ ,  $15^\circ$  and  $30^\circ$ , all bearings showed an increase in effective stiffness. This increase is observed to occur between  $u/t_r = 1.75$  and 2.00.

### 3.6.3 Stress and Strain in Elastomer Layers

Due to rollover, unbonded FREIs experience large displacements and rotations. Thus, defining local coordinates for the stresses and strains is important. Figure 3.10 shows the definition of the local stresses  $S_{11}$ ,  $S_{22}$  and  $S_{33}$  in a bearing, before and after deformation. Initially, for the case shown,  $S_{11}$ ,  $S_{22}$  and  $S_{33}$  are parallel to the global directions of  $x$ ,  $y$  and  $z$  (Fig. 3.10). As the displacement increases, the local coordinates update with the displacements and rotations of the elements used to model the elastomer and fiber reinforcement.

The normalized  $S_{11}$  stress contours in the elastomer layers in bearing B200X68 at  $u/t_r = 0$  (i.e., under pure compression load), 1.00 and 2.00 when loaded at  $0^\circ$ ,  $15^\circ$ ,  $30^\circ$  and  $45^\circ$  are shown in Fig 3.11. The stresses are normalized with respect to the average vertical stress  $\bar{p}$ . For better representation, only half of the bearing is shown. It can be observed from the figure that applying the lateral displacement increases the compression stresses and induces tensile stress in the elastomer layers. It should be noted, however, that these tensile stresses are small compared to those that develop in a bonded bearing [10]. As the displacement increases, both the tensile and compressive peak stress values in the elastomer increase. A stress concentration is observed along the edge of the top and bottom elastomer layers, where the elastomer is being compressed as the bearing is displaced laterally. FEA results show that as the loading direction changes from  $0^\circ$  to  $45^\circ$ , the peak stress in the top and bottom elastomer layers decreases.

Figure 3.12 shows the definition of section lines A-A and B-B in bearing B200X78. A-A runs along the center of the middle elastomer layer, and B-B runs along the center of

the adjacent fiber reinforcement layer, both in the  $x$ -direction. The normalized stress profiles along A-A section line in the bearings obtained for  $0^\circ$  and  $45^\circ$  are presented in Fig. 3.13. For the considered loading directions in Fig. 3.13, FEA results showed similar values for  $S_{11}$  and  $S_{22}$  stresses along section line A-A, and as a result only  $S_{11}$  and  $S_{33}$  stresses are plotted. Under pure compression, the values of  $S_{11}$  and  $S_{33}$  stresses are similar to each other, which is in agreement with the stress assumption in the *pressure solution* method [1]. The closed-form solution developed by Tsai and Kelly [13] for the distribution of the pressure in the elastomer layers is used to calculate the normalized pressure in the center of the elastomer layer under pure compression, and to compare with FEA results. This solution is based on the pressure solution approach and calculates the effective compression modulus of a rectangular pad made of an incompressible material bonded to flexible reinforcement layers at the top and bottom, and is based on these assumptions: (i) The top and bottom surfaces of the elastomer layers remain horizontal after application of the vertical load; (ii) Points on a vertical line in the initial state form a parabola after loading; and (iii) The normal stresses in the elastomer are approximated by the pressure. Good agreement is observed with the prediction of the pressure solution method and the FEA results. The peak normalized stress value predicted by the pressure solution is 2.04, while the peak normalized stress value under compression load obtained from FEA result are 2.01, 2.00 and 2.00 in bearings B200X68, B200X78 and B200X105, respectively.

It can be observed from Fig 3.13 that as the displacement of the bearings increases, the peak absolute values of the  $S_{11}$  stress increase. This increase is more pronounced in

bearing B200X105, where at  $0^\circ$ , for example, the peak absolute normalized value of  $S_{11}$  with a value of 2.00 under pure compression increases to 2.54 and 3.45 at  $u/t_r = 1.00$  and 2.00, respectively. The variation of the peak  $S_{33}$  is different in the bearings. In bearing B200X105, the peak absolute values of  $S_{33}$  increase as the displacement of the bearing increases. In bearings B200X68 and B200X78 however, the peak absolute values of  $S_{33}$  decrease as the lateral displacement of the bearing increases. In bearing B200X68 and at  $0^\circ$  loading direction, for example, the peak absolute normalized value of  $S_{33}$  with a value of 2.01 under pure compression decreases to 1.93 and 1.84 at  $u/t_r = 1.00$  and 2.00, respectively. In addition, changing the loading direction in the bearings from  $0^\circ$  to  $45^\circ$  results in an increase in the peak absolute values of the stresses. FEA results show that at  $u/t_r > 1.00$ , tensile stresses develop in elastomer layers. Traditionally, the presence of large tensile stresses has been a cause of concern in bonded SREIs due to the risk of cavitation [29, 30]; experimental observations on bonded SREIs, however, report bearings surviving without damage at tensile strains greatly exceeding the expected strain at cavitation [2]. Furthermore, SU-FREIs have been tested up to  $u/t_r = 2.50$  at  $0^\circ$  and  $45^\circ$  [6], and up to  $u/t_r = 3.00$  at  $0^\circ$  [31,32] and in no case was cavitation observed to have occurred.

Contours of  $\varepsilon_{13}$  shear strain at different displacement values for bearings B200X68 and B200X105 loaded at  $0^\circ$  and  $45^\circ$  are presented in Fig. 3.14. Under pure compression, shear strains vary linearly through the thickness of each elastomer layer, with a peak value of 0.27 in both bearings. As the bearings undergo displacement, additional shear strains are induced in the elastomer layers. Comparing the contours of shear strain in the

center portion of the bearing, it can be observed that the values of  $\varepsilon_{13}$  shear strains are reduced when the loading direction is varied from  $0^\circ$  to  $45^\circ$ . It should be noted that in the  $45^\circ$  loading direction, the bearing is deformed along the global  $x$  and  $y$  directions, and unlike the  $0^\circ$  loading,  $\varepsilon_{23}$  shear strains have non-zero magnitudes. It can be observed that changing the number of elastomer layers from 13 to 20 has a negligible effect on the distribution of the shear strains and the contours of shear strains in bearing B200X105 look similar to those of bearing B200X68, both at  $0^\circ$  and  $45^\circ$ . However, an increase in the peak shear strain values is observed by changing the aspect ratio from 2.9 to 1.9. At  $u/t_r = 1.00$ , for example, the maximum shear strain in the elastomer layers is found to be 1.27 at  $0^\circ$  and 1.30 at  $45^\circ$  in bearing B200X68. In bearing B200X105, the maximum  $\varepsilon_{13}$  shear strain values are found to be 1.43 and 1.47 at  $0^\circ$  and  $45^\circ$ , respectively, which shows an average increase of 13%. In selecting the maximum  $\varepsilon_{13}$  shear strain values, the localized shear strains at the corner of the top and bottom elastomer layers, shown in a gray in Fig. 3.14, are neglected.

### 3.6.4 Stress in Fiber Reinforcement Layers

Fig. 3.15 compares the distribution of normalized in-plane  $S_{11}$  and  $S_{22}$  stresses in the center fiber reinforcement layer along section line B-B in the bearings. The definition of  $S_{11}$  and  $S_{22}$  in the four-node quadrilateral elements used to model the fiber reinforcement layers is similar to that in the nine-node hexahedron elements used for elastomer layers (Fig. 3.10). FEA results show that under a pure compression load, the peak normalized tensile stress in the fiber reinforcement layer is 6.02 in all the bearings. At  $u/t_r = 1.00$ ,

the distribution of stresses changes and compressive stresses are observed in the fiber reinforcement layer in regions close to the edges. The peak normalized stress values are also found to increase. In bearing B200X105 loaded at  $0^\circ$ , for example, the peak normalized values of  $S_{11}$  and  $S_{22}$  are 8.51 and 7.05, respectively, while at  $45^\circ$ , due to symmetry, the peak normalized  $S_{11}$  and  $S_{22}$  are equal to each other, with a value of 8.72. At  $u/t_r = 2.00$  in the  $0^\circ$  loading direction, FEA results show an increase in the peak  $S_{11}$ , while the change in the peak  $S_{22}$  stress values is negligible, compared to the values at  $u/t_r = 1.00$ . Comparing the stress plots at  $u/t_r = 1.00$  and  $2.00$  in Fig. 3.15 shows that changing the loading direction from  $0^\circ$  to  $45^\circ$  results in an increase in the peak stress values and the development of large  $S_{22}$  stresses at the edge of the fiber reinforcement layers. For bearing B200X105 at  $u/t_r = 2.00$ , the peak  $S_{11}$  and  $S_{22}$  stress values at the center portion of the bearing increase by 39% and 209%, respectively, when the loading directions is varied from  $0^\circ$  to  $45^\circ$ . As the aspect ratio of the bearing increases, the increase in the peak stress values observed at  $45^\circ$  loading direction decreases. In bearing B200X68 for example, the increase in the peak  $S_{11}$  and  $S_{22}$  stresses at the center portion of the fiber reinforcement layer is 8% and 20%, respectively.

### 3.7 Conclusions

This paper presents the results of 3D FEA of the lateral response characteristics of unbonded square FREIs loaded in different directions. FE models of three previously tested FREIs [5] were validated using experimental test results. The investigated square bearings in this study had a width of 200 mm with total height values of 68mm, 78mm

and 105mm. The shape factor of all three bearings was 10.6, while their aspect ratios were 1.9, 2.6 and 2.9. FEA of each bearing was conducted to investigate its response characteristics in the lateral loading directions  $0^\circ$ ,  $15^\circ$ ,  $30^\circ$  and  $45^\circ$ . Based on the FEA results, the following conclusions are drawn:

- Due to rollover, the effective lateral stiffness of all the bearings decreased with an increase in the lateral displacement.
- In general, the effective lateral stiffness of the bearings increased as the loading direction changed from  $0^\circ$  to  $45^\circ$ . As the height of the bearing decreased, the sensitivity of the lateral response of the bearing to the loading direction decreased.
- Bearings showed a hardening behavior at large displacements (ranging from  $u/t_r = 1.55$  to 2.00). The displacement at which this hardening occurs ( $D_h$ ) was affected by the loading direction. For the bearings and the loading directions considered in this study,  $D_h$  increased with an increase in the loading direction from  $0^\circ$  to  $45^\circ$ .
- Bearing B200X105 with an aspect ratio of 1.9 showed an unstable response when loaded at  $0^\circ$  and  $15^\circ$ , while at  $30^\circ$  and  $45^\circ$  it exhibited a stable rollover response. Bearings with aspect ratios of 2.5 and 2.9 exhibited a stable rollover response at all the considered loading directions.
- As the displacement of the bearings increases, the peak absolute values of  $S_{11}$  and  $S_{33}$  stresses in the elastomer layers increased. Changing the loading direction from  $0^\circ$  to  $45^\circ$  resulted in an increase in the peak absolute values of  $S_{11}$  and  $S_{33}$  in the center elastomer layers, but a decrease in the top and bottom elastomer layers.

However, the peak absolute values of stresses decreased in the top and bottom elastomer layers as the loading direction was varied from  $0^\circ$  to  $45^\circ$ .

- Changing the loading direction from  $0^\circ$  to  $45^\circ$  resulted in a decrease in  $\varepsilon_{13}$  and an increase in  $\varepsilon_{23}$  shear strain values. The peak shear strain value in the bearing with an aspect ratio of 1.9 was observed to be 13% higher than the peak shear strain in bearing with an aspect ratio of 2.9.
- FEA results showed that as the displacement of the bearing increases, the tensile stresses in the reinforcement layers increase. Changing the loading direction from  $0^\circ$  to  $45^\circ$  resulted in an increase in the peak stress values in the reinforcement layers. At  $u/t_r = 2.00$ , in the  $45^\circ$  loading direction, large tensile  $S_{22}$  stresses developed at the edges of the reinforcement layer.

In this study, the lateral response of three unbonded square FREIs in different loading directions was investigated using FEA. During each analysis, the magnitude of the displacement was monotonically increased; however, the direction of loading was held constant. Additionally, the magnitude of the vertical load was held constant, and the effect of varying the vertical load on the lateral response of the bearing was not considered in this study. Additional work is required in order to evaluate the bidirectional behavior of unbonded FREIs, where both the magnitude and direction of the displacement change during the loading history. Furthermore, as the stress-strain relationship of rubber materials is known to be nonlinear, the use of a more sophisticated constitutive model, e.g., Mooney-Rivlin or Ogden, in future studies is recommended.

Finally, additional experimental testing to evaluate the lateral response of FREIs loaded in multiple directions would be beneficial.

According to the results of this study, if the goal is to maintain constant lateral response behavior under various loading directions, it is recommended that higher aspect ratio values be considered for square unbonded FREIs.

### **3.8 Acknowledgments**

This research was carried out as part of the mandate of the Centre for Effective Design of Structures (CEDs) at McMaster University and is partially funded by the Ontario Ministry of Economic Development and Innovation and by the Natural Sciences and Engineering Research Council of Canada (NSERC). The authors also acknowledge MSC Software Corporation for their support.

### **3.9 References**

- [1] Kelly JM. Analysis of fiber-reinforced elastomeric isolators. *Journal of Seismology and Earthquake Engineering* 1999;2(1):19-34.
- [2] Kelly JM, Konstantinidis D. *Mechanics of rubber bearings for seismic and vibration isolation*. Wiley, Chichester, UK. 2011.
- [3] Kelly JM. Seismic isolation systems for developing countries. *Earthquake Spectra* 2002;18(3):385-406.

- [4] Moon BY, Kang GJ, Kang BS, Kelly JM. Design and manufacturing of fiber-reinforced elastomeric isolator for seismic isolation. *Journal of Materials Processing Technology* 2002;130-131:145-150.
- [5] Toopchi-Nezhad H, Tait MJ, Drysdale RG. Testing and modeling of square carbon fiber-reinforced elastomeric seismic isolators. *Structural Control and Health Monitoring* 2007;15(6): 876-900.
- [6] Toopchi-Nezhad H, Tait MJ, Drysdale RG. Lateral response evaluation of fiber-reinforced neoprene seismic isolators utilized in an unbonded application. *Journal of Structural Engineering* 2008;134(10):1627-1637.
- [7] Russo G, Pauletta M, Cortesia A. A study on experimental shear behaviour of fiber-reinforced elastomeric isolators with various fiber layouts, elastomers and aging conditions. *Engineering Structures* 2013;52:422-433.
- [8] Kelly JM, Takhirov SM. Analytical and experimental study of fiber-reinforced elastomeric isolators. PEER Report 2001/11, Pacific Earthquake Engineering Research Center, University of California, Berkeley, 2001.
- [9] Kelly JM, Takhirov SM. Analytical and experimental study of fiber-reinforced strip isolators. PEER Report 2002/11, Pacific Earthquake Engineering Research Center, University of California, Berkeley, 2002.
- [10] Toopchi-Nezhad H, Tait MJ, Drysdale RG. Bonded versus unbonded strip fiber reinforced elastomeric isolators: finite element analysis. *Composite Structures* 2011;93(2):850-859.

- [11] Kelly JM, Konstantinidis D. Low-cost seismic isolators for housing in highly-seismic developing countries. ASSISI 10th World Conference on Seismic Isolation, Energy Dissipation and Active Vibrations Control of Structures, Istanbul, 28-31 May 2007.
- [12] Tsai HC, Kelly JM. Stiffness analysis of fiber-reinforced elastomeric isolators. PEER Report 2001/05, Pacific Earthquake Engineering Research Center, University of California, Berkeley, 2001.
- [13] Tsai HC, Kelly JM. Stiffness analysis of fiber-reinforced rectangular isolators, *Journal of Engineering Mechanics* 2002;128(4):462-470.
- [14] Tsai HC. Compression stiffness of infinite-strip bearings of laminated elastic material interleaving with flexible reinforcements. *Int J Solids Struct* 2004;41(24):6647–60.
- [15] Tsai HC. Compression stiffness of circular bearings of laminated elastic material interleaving with flexible reinforcements. *Int J Solids Struct* 2006;46(11):3484–97.
- [16] Pinarbasi S, Mengi Y. Elastic layers bonded to flexible reinforcements. *Int J Solids Struct* 2008;45(3): 794-820.
- [17] Toopchi-Nezhad H, Tait MJ, Drysdale RG. Stiffness analysis of fiber-reinforced rubber isolators under compressive loads: a finite element approach. In: *Proceedings of the 9th US national and 10th Canadian conference on earthquake engineering*. Toronto, 25–29 July 2010.
- [18] Pinarbasi S, Okay F. Compression of hollow-circular fiber-reinforced rubber bearings. *Struct Eng and Mech* 2011;38(3):361-84.

- [19] Kelly JM, Calabrese A. Mechanics of fiber reinforced bearings. PEER Report 2012/101, Pacific Earthquake Engineering Research Center, University of California, Berkeley, 2012.
- [20] Osgooei PM, Tait MJ, Konstantinidis D. Three-dimensional finite element analysis of circular fiber-reinforced elastomeric bearings under compression. *Composite Structures* 2013 DOI: 10.1016/j.compstruct.2013.09.008.
- [21] Peng TB, Zhang H, Li JZ, Li WX. Pilot study on the horizontal shear behavior of FRP rubber isolators. *Journal of Vibration and Shock* 2009;28:127-130. [in Chinese]
- [22] Konstantinidis D, Kelly JM, Makris N. Experimental investigations on the seismic response of bridge bearings. Report No. EERC-2008/02, Earthquake Engineering Research Center, University of California, Berkeley, 2008.
- [23] Mordini A, Strauss A. An innovative earthquake isolation system using fibre reinforced rubber bearings. *Engineering Structures* 2008;30(10):2739-2751.
- [24] Kelly JM, Marsico MR. Stability and post-buckling behavior in nonbolted elastomeric isolators. *Seismic Isolation and Protection Systems* 2010;1(1):41-54.
- [25] Osgooei PM, Tait MJ, Konstantinidis D. Three-dimensional finite element analysis of square fiber-reinforced elastomeric isolators (FREIs) under lateral loads. CSCE 2013 Annual Conference, Montréal, May 29 to June 1, 2013.
- [26] Gerhaher U, Strauss A, Bergmeister K. Numerical modeling of elastomeric bearings in structural engineering, *Advances in Materials Sciences* 2011;11(3):51-63.
- [27] ASCE-7. Minimum design loads for buildings and other structures, ASCE/SEI 7-10. New York, American Society of Civil Engineers, 2010.

- [28] MSC Marc. Theory and user information, vol. A. Santa Ana: MSC Software Corporation; 2011.
- [29] Pinarbasi S, Akyuz U, Mengi Y. A new formulation for the analysis of elastic layers bonded to rigid surfaces, *International Journal of Solids and Structures* 2006;43(14):4271-4296.
- [30] Gent AN, Meinecke EA. Compression, bending and shear of bonded rubber blocks, *Polymer Engineering and Science* 1970; 10(1):48-53.
- [31] Tait MJ, de Raaf MGP, Toopchi-Nezhad H. Stability of fiber-reinforced elastomeric bearings in an unbonded application. *Composite Materials* 2011, 45(18):1873-1884.
- [32] Foster, BAD. Base isolation using stable unbonded fibre reinforced elastomeric isolators (SU-FREI). M.A.Sc. thesis, McMaster University. 2011.

Table 3.1. Characteristics of the bearings considered in this study

Bearing	Width (mm)	Height (mm)	$t_r$ (mm)	$n$	$t$ (mm)	$t_f$ (mm)	$S$	Aspect Ratio
B200X105	200	105	94.0	20	4.7	0.56	10.6	1.9
B200X78	200	78	70.5	15	4.7	0.56	10.6	2.6
B200X68	200	68	61.1	13	4.7	0.56	10.6	2.9

Table 3.2. Normalized displacement values  $D_r$ ,  $D_c$ ,  $D_h$  and  $D_f$  for the bearings loaded at  $0^\circ$ .

Bearing	$D_r/t_r$	$D_c/t_r$	$D_h/t_r$	$D_f/t_r$
B200X105	0.10	1.11	1.62	1.96
B200X78	0.14	1.30	1.67	1.99
B200X68	0.16	1.31	1.68	2.00

Table 3.3. Effective lateral stiffness in different loading directions

$u/t_r$	Effective lateral stiffness normalized by $GA/t_r$											
	B200X105				B200X78				B200X68			
	$0^\circ$	$15^\circ$	$30^\circ$	$45^\circ$	$0^\circ$	$15^\circ$	$30^\circ$	$45^\circ$	$0^\circ$	$15^\circ$	$30^\circ$	$45^\circ$
0.25	0.826	0.819	0.812	0.818	0.874	0.870	0.869	0.867	0.893	0.887	0.887	0.886
0.50	0.716	0.726	0.743	0.752	0.802	0.805	0.811	0.821	0.818	0.832	0.838	0.841
0.75	0.603	0.620	0.651	0.665	0.715	0.723	0.744	0.755	0.743	0.760	0.777	0.787
1.00	0.491	0.513	0.560	0.584	0.626	0.639	0.671	0.688	0.674	0.685	0.710	0.726
1.25	0.382	0.413	0.478	0.512	0.545	0.563	0.606	0.631	0.607	0.620	0.653	0.675
1.50	0.276	0.337	0.418	0.448	0.474	0.507	0.554	0.582	0.549	0.567	0.607	0.631
1.75	0.411	0.371	0.392	0.414	0.544	0.517	0.522	0.539	0.529	0.574	0.570	0.584
2.00	0.470	0.466	0.419	0.413	0.587	0.587	0.541	0.509	0.615	0.627	0.585	0.548

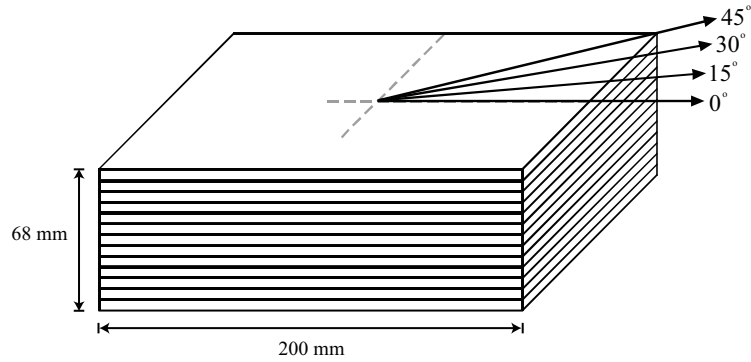


Figure 3.1. Directions of lateral loading investigated in this study (shown on bearing B200X68)

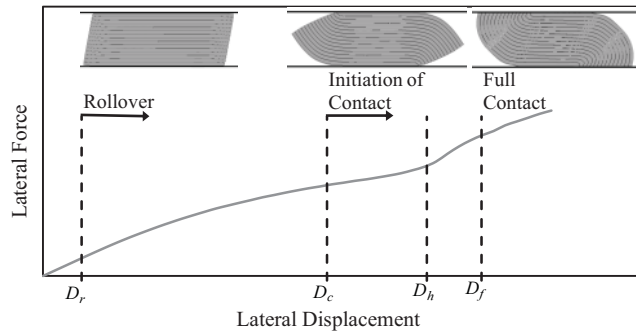


Figure 3.2. Typical lateral load-displacement of a FREI bearing loaded in the 0° direction

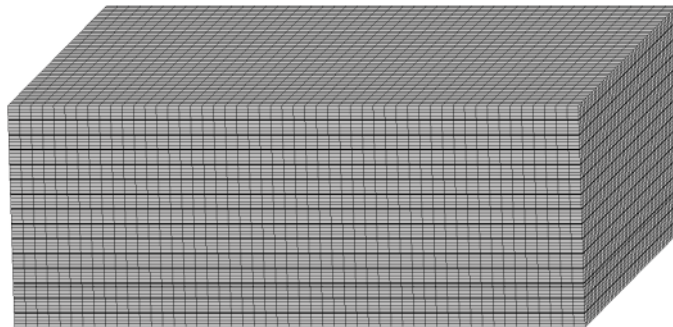


Figure 3.3. Finite element model of bearing B200X78

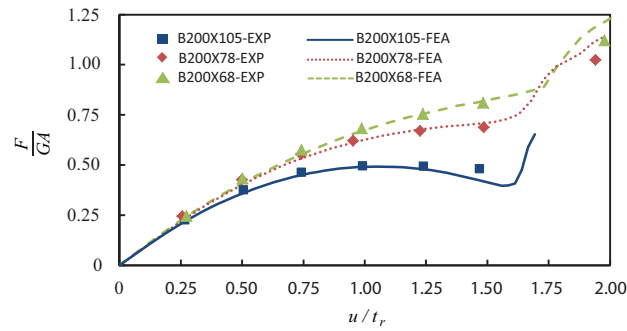


Figure 3.4. Lateral load-displacement relationships of the bearings obtained from FEA and test results

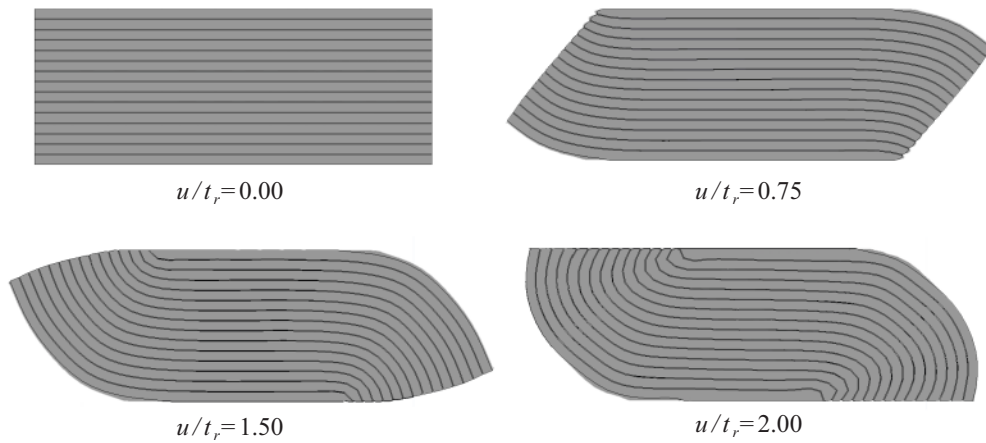


Figure 3.5. Deformed shapes of bearing B200X78 at 0°, obtained from FEA results

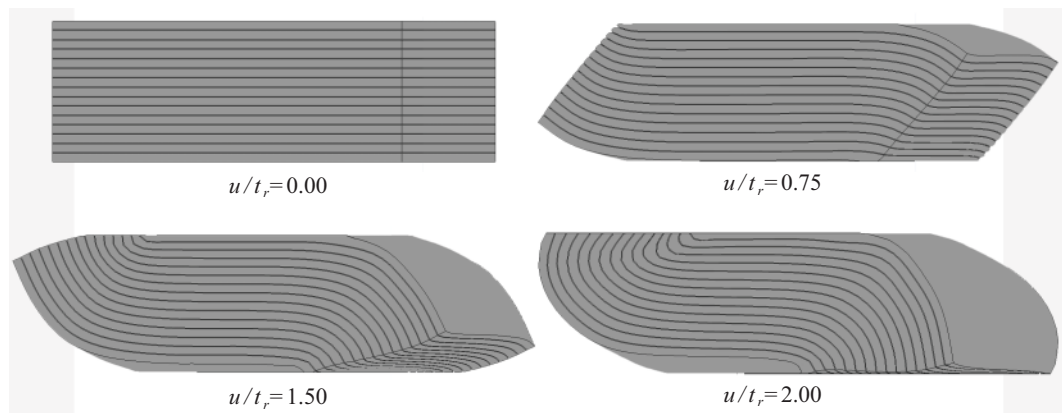


Figure 3.6. Deformed shapes of bearing B200X78 at 15°, obtained from FEA results

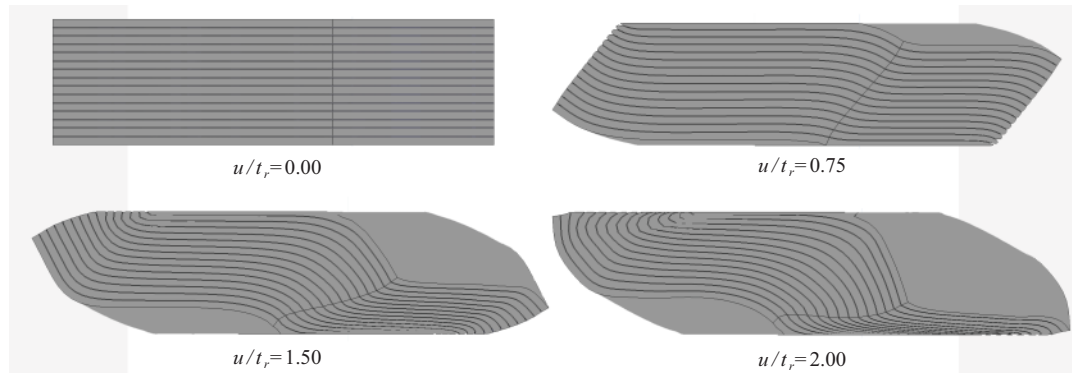


Figure 3.7. Deformed shapes of bearing B200X78 at 30°, obtained from FEA results

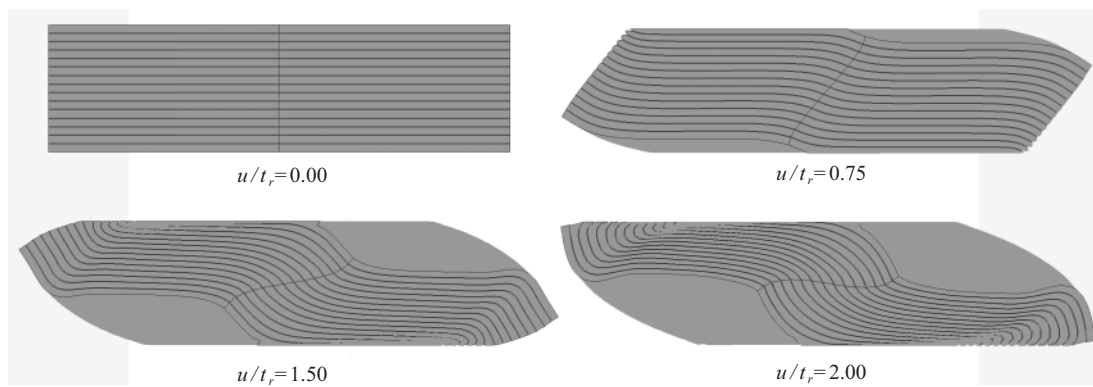


Figure 3.8. Deformed shapes of bearing B200X78 at 45°, obtained from FEA results

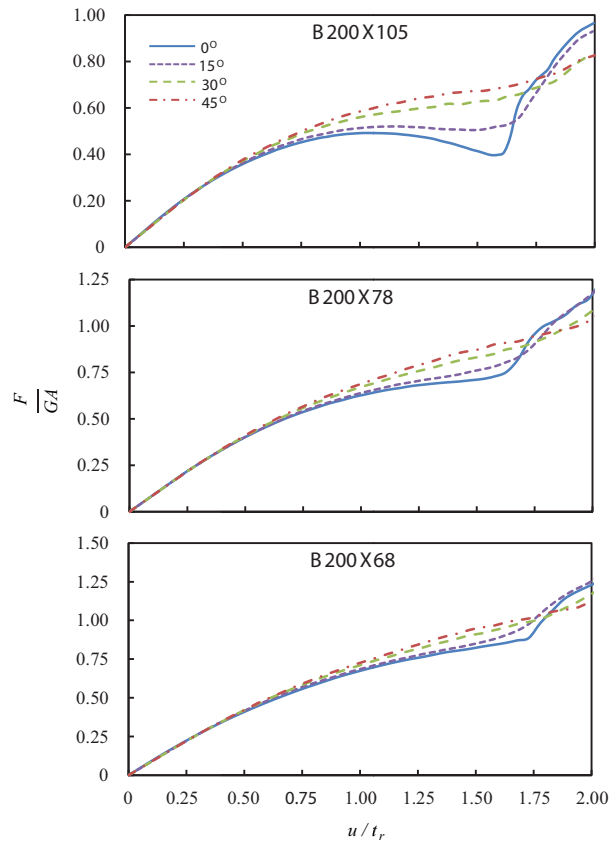


Figure 3.9. Lateral load-displacement curves of the bearings at different loading orientations obtained from FEA results

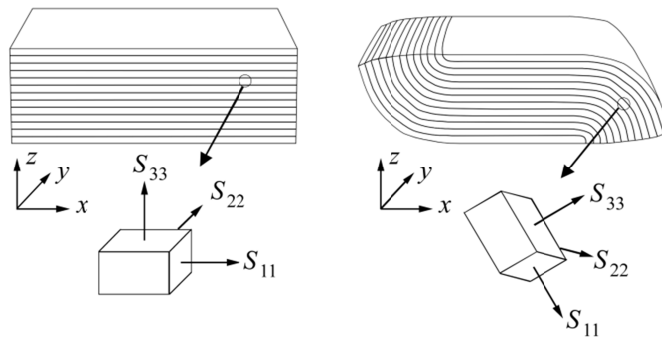


Figure 3.10. Local stresses in the undeformed configuration (left) and deformed configuration (right)

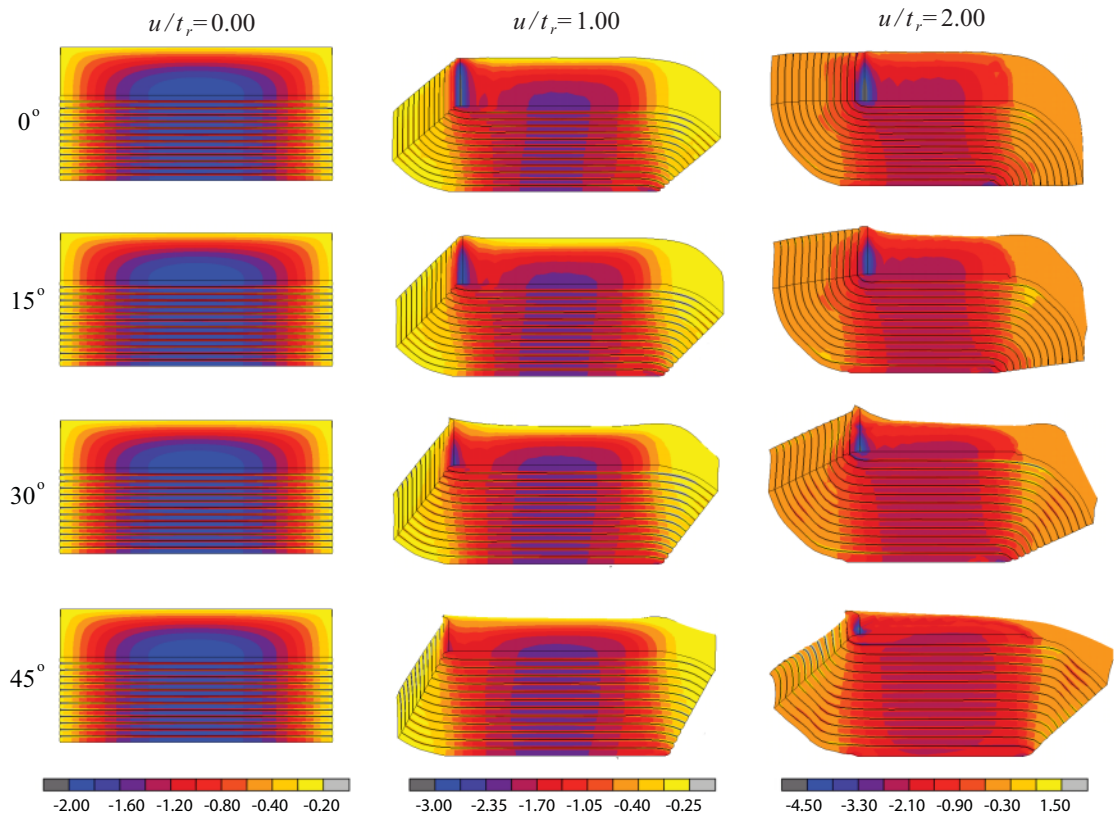


Figure 3.11. Contours of normalized  $S_{11}$  stress in bearing B200X68 for the four different loading directions

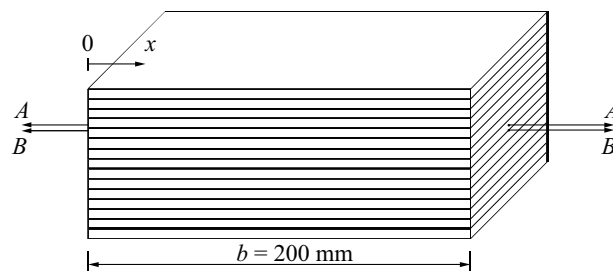


Figure 3.12. Definition of A-A and B-B section lines in bearing B200X78

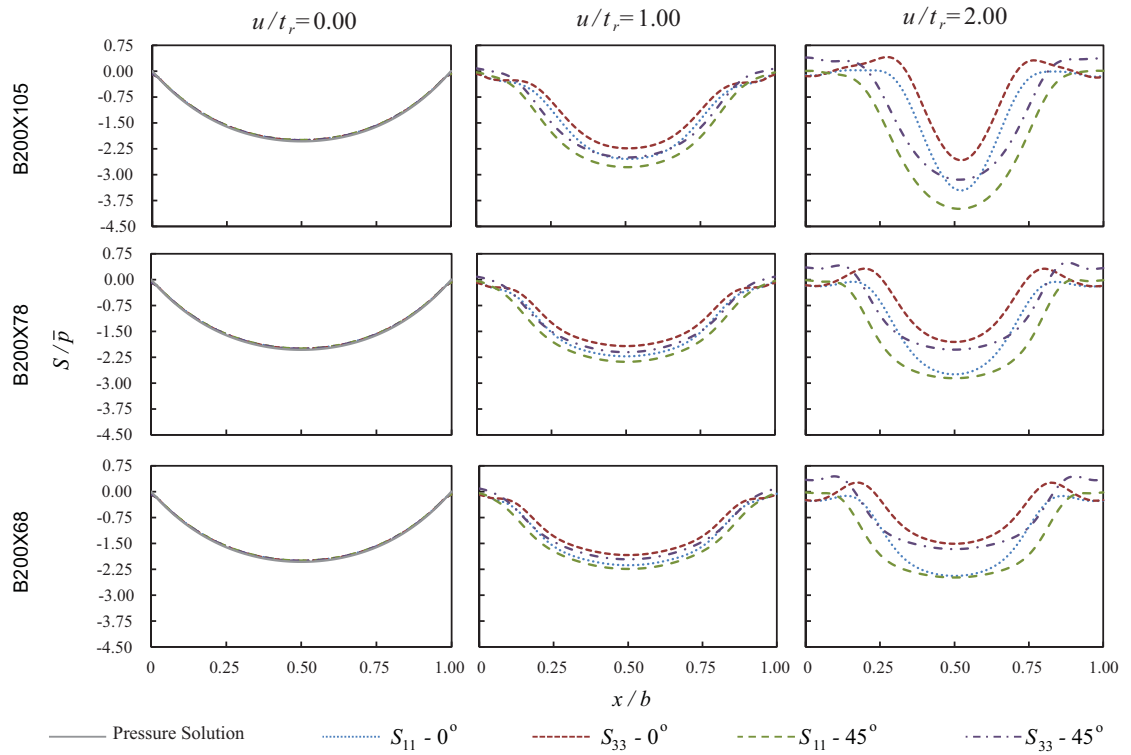


Figure 3.13. Variation of normalized stress profiles along the width of the bearings at  $0^\circ$  and  $45^\circ$

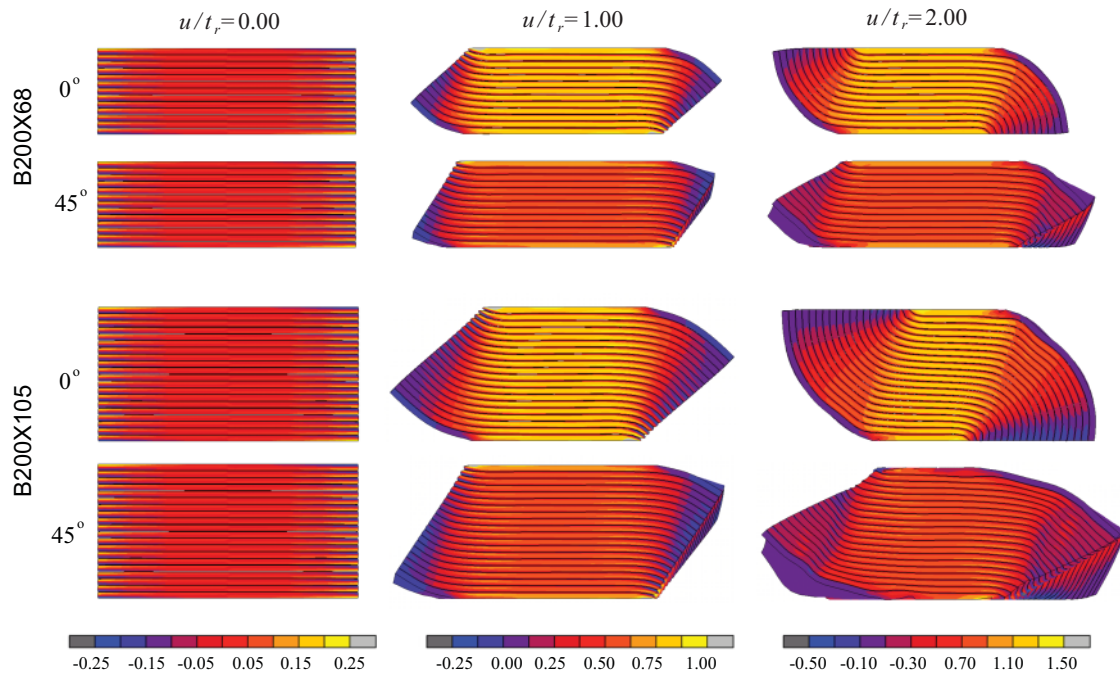


Figure 3.14. Contours of shear strain  $\epsilon_{13}$  in bearings B200X68 and B200X105 loaded at 0° and 45°

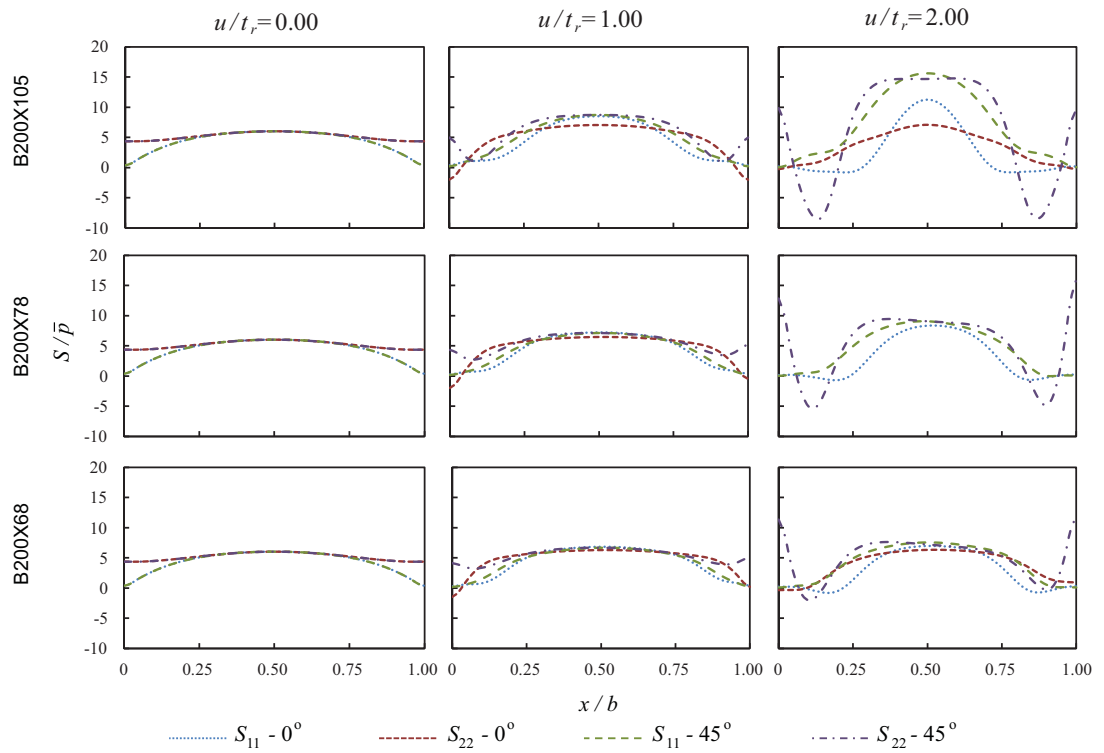


Figure 3.15. Variation of normalized in-plane stresses in center fiber reinforcement layers along section line B-B in the bearings

## **Chapter 4: Computational Model for Unbonded Fiber-Reinforced Elastomeric Isolators (U-FREIs)**

### **Abstract**

A model is proposed to simulate the lateral response of unbonded fiber-reinforced elastomeric isolators (U-FREIs). This proposed model combines a bilinear model having Pivot hysteresis with a nonlinear elastic model. These two models, when connected in parallel, can be used to predict the variation of the effective stiffness and effective damping ratio of a U-FREI isolation system. In contrast to existing U-FREI models, the proposed Pivot-Elastic model is non-iterative, determination of the model parameters does not require fitting over the entire experimentally obtained hysteresis loops, and its simplified form allows it to be implemented in commercially available structural analysis programs. The Pivot-Elastic model is employed to conduct nonlinear time history analyses, and the accuracy of this model is evaluated using test results from a previous shake table study. Findings confirm the ability of the proposed model to predict the seismic response of structures isolated with U-FREIs. Subsequently, the sensitivity of the peak response values of the isolated structure to variation in isolation effective stiffness and effective damping ratio is investigated. Finally, the effect of different installation applications is investigated by considering FREIs in a bonded application.

#### **4.1 Introduction**

Conventional steel-reinforced elastomeric isolators (SREIs) are heavy and expensive, which limits their application to high importance and/or expensive structures. By eliminating the thick top and bottom steel connecting plates and using fiber material instead of steel for the reinforcing layers, the weight of the isolators can be significantly reduced. Unlike SREIs, which utilize a hot vulcanization manufacturing process, fiber-reinforced elastomeric isolators (FREIs) can be manufactured using cold vulcanization [1], which has the potential to reduce the high manufacturing costs associated with SREIs. An additional advantage of FREIs is the ability to manufacture large pads and cut individual isolators from the pads to the desired size.

FREIs can be installed with no bonding or fastening to the supports in an unbonded application. Shear forces are transferred from the isolator to the superstructure and substructure through friction along the support surfaces. Due to the absence of the thick end plates and flexibility of fiber reinforcement layers, unbonded FREIs (U-FREIs) undergo a unique rollover deformation when subjected to lateral loading. This rollover is shown to increase the seismic isolating efficiency by reducing the effective lateral stiffness of the isolators [2]. Additionally, unbonded application results in a reduced stress demand on the isolators [2] and U-FREIs have been shown [1,3] to provide a higher level of energy dissipation compared to conventional SREIs. Experimental studies [1,3-5] have confirmed the viability of U-FREIs.

The lateral load-displacement relationship of U-FREIs can be divided into three different regions: an initial linear region; a softening region, where the effective stiffness

reduces due to the rollover; and a subsequent stiffening region, where the effective stiffness increases due to the contact of the originally vertical faces of the isolator with the supports [6]. Results from lateral cyclic tests conducted on U-FREIs [1,3,4] have shown that both the effective stiffness and equivalent damping vary nonlinearly with displacement. As such, modeling an isolation system composed of U-FREIs with such complex load-displacement behavior is challenging.

There are few closed-form solutions in the literature to predict the lateral response of U-FREIs [7-11]. However, these solutions do not take into account the damping in the isolators. To conduct time history analysis of structures seismically isolated with U-FREIs, a model that accurately predicts both the stiffness and damping characteristics of the isolators is required. Toopchi-Nezhad et al. [12] proposed two methods to model the lateral behavior of U-FREIs, a bilinear type model and a 10-parameter rate-dependent model based on a set of equations proposed by Hwang et al [13]. Toopchi-Nezhad et al. [14] used a 5-parameter nonlinear spring and a viscous dashpot to model the lateral response of U-FREIs. Love et al. [15] employed a modified form of the linearized Bouc-Wen model to model a base isolation system comprised of U-FREIs. For all these U-FREI models, separate model parameters are assigned to hysteresis loops obtained at different displacement amplitudes, and thus conducting a time history analysis using these models requires a number of iterations and a customized numerical code. A simplified computational model that accurately simulates the response of U-FREIs and requires no iterations is needed to facilitate the analysis and design of structures isolated with this type of isolator.

In this paper, a model to predict the lateral response of U-FREIs is proposed. The proposed model, hereafter referred to as the *Pivot-Elastic model*, is non-iterative and can be employed in general purpose structural analysis codes, such as SAP2000 [16]. In addition, and in contrast to existing U-FREI models, determination of the parameters of the Pivot-Elastic model does not require fitting over entire hysteresis loops; rather, only the values of the effective stiffness and damping ratio are required. Thus, the Pivot-Elastic model could be used to complete a preliminary analysis before the isolators are manufactured and tested. The model is an in-parallel combination of two models: a bilinear plastic model with Pivot hysteretic response [17] and a nonlinear elastic spring. Results from lateral cyclic tests carried out on a square U-FREI are used to determine the model parameters. The Pivot-Elastic model is subsequently used to conduct nonlinear time history analyses of a two-story steel moment frame structure seismically isolated with U-FREIs. In order to evaluate the model, the predicted response of the building under earthquake excitation is compared with the results of a previous shake table study. The proposed model is subsequently used to conduct a series of analyses in order to investigate the sensitivity of the predicted peak response values of the isolated structure to  $\pm 15\%$  change in the values of the effective stiffness and damping ratio of the isolators. Finally, the effect of different installation applications on the peak response values of the isolated structure is investigated by considering FREIs in a bonded application.

## 4.2 Modeling U-FREIs

### 4.2.1 Bilinear Model

In an effort to simplify the inelastic analysis of seismically isolated bridges, AASHTO's 1991 Guide Specifications for Seismic Isolation Design [18] introduced the concept of an equivalent linear system, using an effective period and effective damping ratio, to describe the dynamic behavior of the most common isolation systems at the time, namely the lead plug system and the friction pendulum system, both of which can be modeled by bilinear hysteresis [19]. While the validity of using an effective period and effective damping ratio to accurately describe the seismic response of bilinear hysteretic systems has been challenged by various studies (e.g., Hwang and Sheng [20, 21] and Makris and Kampas [22]), these linear parameters are invariably present in current seismic isolation design code provisions. Figure 4.1 shows the definition of the bilinear model, where  $u_y$  is the yield displacement, and  $K_1$  and  $K_2$  are the first and second stiffness, respectively. The effective (secant) stiffness of the system,  $K_{\text{eff,bi}}$ , at displacement  $u$  can be calculated using

$$K_{\text{eff,bi}} = \begin{cases} K_1 & u < u_y \\ K_2 + \frac{u_y}{u}(K_1 - K_2) & u \geq u_y \end{cases} \quad (4.1)$$

The energy dissipated per cycle,  $E_{\text{h,bi}}$ , for  $u \geq u_y$  can be obtained by

$$E_{\text{h,bi}} = 4u_y(u - u_y)(K_1 - K_2) \quad (4.2)$$

and the effective damping ratio of the system for  $u \geq u_y$  can be calculated using

$$\beta_{\text{eff,bi}} = \frac{2u_y(u - u_y)(K_1 - K_2)}{\pi K_{\text{eff,bi}} u^2} \quad (4.3)$$

The damping ratio of the system has a value of zero at  $u \leq u_y$ , reaches its peak value as the displacement increases, and approaches a value of zero when  $u \rightarrow \infty$ . It can be shown that the maximum value of the damping occurs at a displacement of [19]

$$u_{\beta,\text{bi}} = u_y(1 + \sqrt{1 + \alpha}) \quad (4.4)$$

where  $\alpha = (K_1 - K_2)/K_2$ . Substituting Eq. (4.4) into Eq. (4.3), the maximum value of the damping ratio of the system is calculated to be [19]

$$\beta_{\text{bi,max}} = \frac{2\alpha}{\pi} \frac{1}{2\sqrt{1 + \alpha} + 2 + \alpha} \quad (4.5)$$

Toopchi-Nezhad et al. [12] employed the bilinear idealization for modeling square U-FREIs. The hysteresis loops obtained from lateral cyclic tests were used to determine the bilinear model parameters for different displacement amplitudes considered in the tests. As a result, the time history analysis required an iterative procedure to be adopted. At the beginning of each time history analysis, a maximum isolation displacement was assumed, and the corresponding bilinear model was used for the U-FREI system. At the end of each iteration, the maximum isolation displacement was calculated and compared with the value used at the beginning of the iteration, and, if required, the analysis was repeated with the updated model parameters until convergence was reached. In addition, Toopchi-Nezhad et al. [12] used  $\beta = \beta_{\text{bi,max}}$  for  $u < u_{\beta,\text{bi}}$ . This constraint on damping overcomes one of the deficiencies of the bilinear model, which is the underprediction of

the damping ratio at low displacement amplitudes; however, it requires a customized numerical code for the purpose of analysis.

#### 4.2.2 Bilinear Pivot Model

Figure 4.2(a) shows the definition of the Pivot hysteretic relationship, introduced by Dowell et al. [17]. A special case of the Pivot model (the Bilinear Pivot model) is obtained when  $\beta = 1$  and the unloading stiffness is equal to the initial stiffness  $K_1$ , as shown in Fig. 4.2(b). The energy dissipated per cycle of displacement amplitude  $u > u_y$  is

$$E_{h,bp} = \frac{(3K_1u_y + K_2u - K_2u_y)(K_1 - K_2)(u - u_y)}{K_1} \quad (4.6)$$

Unlike the bilinear model, where the energy dissipated per cycle is a linear function of the displacement (Eq. 4.2), it can be observed from Eq. (4.6) that for the bilinear Pivot model, the energy dissipated per cycle is a quadratic function of the displacement. This feature of the bilinear Pivot model provides additional control on the amount of energy dissipation at various displacement amplitudes compared to the bilinear model.

#### 4.2.3 Proposed Pivot-Elastic Model

Figure 4.3 shows a schematic of the proposed Pivot-Elastic model, which is a combination of a bilinear Pivot model and a nonlinear elastic model. These two models can be combined to obtain the required values of effective stiffness and damping ratio of the isolation system at the selected displacement amplitudes. In this study, a fifth-order

polynomial is adopted for the load-displacement relationship of the nonlinear elastic (NE) model. The force of the NE element,  $F_{NE}$ , at displacement  $u$  will be equal to

$$F_{NE} = a_1u + a_2u^3 + a_3u^5 \quad (4.7)$$

where  $a_i$  are model parameters to be determined. The effective stiffness of the proposed model at displacement  $u$  is

$$K_{\text{eff}} = \begin{cases} K_1 + a_1 + a_2u^2 + a_3u^4 & u < u_y \\ (K_1 - K_2)\frac{u_y}{u} + K_2 + a_1 + a_2u^2 + a_3u^4 & u \geq u_y \end{cases} \quad (4.8)$$

Since the bilinear Pivot model provides the only source of energy dissipation in the Pivot-Elastic model, the effective damping ratio of the system at  $u \geq u_y$  can be calculated by

$$\beta_{\text{eff}} = \frac{(3K_1u_y + K_2u - K_2u_y)(K_1 - K_2)(u - u_y)}{2\pi K_{\text{eff}}K_1u^2} \quad (4.9)$$

### 4.3 U-FREI System

The U-FREI considered in this study is a square  $\frac{1}{4}$ -scale bearing with plan dimensions of 70 mm  $\times$  70 mm and a total height of 25 mm. The shape factor (defined as the total loaded area of one elastomer layer to the load-free area of the layer) is  $S = 11$ , and the aspect ratio (width-to-height ratio) is  $R = 2.8$ . The isolators were constructed using neoprene rubber and were reinforced with bidirectional woven carbon fiber-reinforced polymer (CFRP) [2]. A constant average vertical stress of  $p = 1.6$  MPa was applied to the bearings while they were subjected to sinusoidal cycles of lateral

displacements (referred to as lateral cyclic testing) [2]. The following displacement amplitudes were considered in the experiment:  $u/t_r = 0.25, 0.50, 0.75, 1.00, 1.50$  and  $2.00$ , where  $t_r = 19$  mm is the total thickness of rubber layers. Figure 4.4 shows the input displacement history used in the cyclic testing. The values of the effective stiffness and damping ratio of the bearing calculated from the unscragged hysteresis loops are presented in Table 4.1.

#### 4.4 Modeling U-FREI using Pivot-Elastic Model

The proposed Pivot-Elastic model is used to simulate the force-displacement response of the U-FREI. The required parameters for the model are those for the bilinear Pivot ( $K_1$ ,  $K_2$  and  $u_y$ ) and the fifth-order polynomial elastic ( $a_1$ ,  $a_2$  and  $a_3$ ) models. These parameters can be determined by minimizing the error between the values of the effective stiffness and effective damping ratio, calculated using Eqs. (4.6) and (4.7), respectively, and those obtained from cyclic tests over a wide range of displacement amplitudes (Table 4.1). Thus, unlike existing U-FREI models, the procedure of determining the parameters of the Pivot-Elastic model does not require fitting over the entire hysteresis loops of the isolators. Furthermore, the model is rate-independent and suitable over a wide range of displacement amplitudes, without need for iterations. Since the energy dissipated in most elastomers is nearly frequency-independent [23], the proposed model is appropriate for a wide range of elastomers. The performance of the model remains to be evaluated for particular elastomers, such as highly filled compounds, which exhibit large amounts of viscous damping (i.e., high-damping rubber bearings).

The model parameters calculated for the U-FREI are shown in Table 4.2. The predicted values for effective stiffness and damping ratio by the model and the percentages of error with respect to the experimental values are listed in Table 4.3. Figure 4.5 compares the normalized hysteresis loops of the bearing predicted by the model (solid line) with the experimentally obtained unscrapped response (dashed line). In Fig. 4.5, the force is normalized with respect to  $GA$ , where  $G = 0.4$  MPa is the nominal shear modulus of the rubber, and  $A = 4900$  mm<sup>2</sup> corresponds to the plan area of the isolator.

## 4.5 Evaluation of the Proposed Pivot-Elastic Model

### 4.5.1 Base Isolated Structure

Results of a shake table study carried out by Toopchi-Nezhad et al. [24] are used to evaluate the suitability of the proposed model for the U-FREI system. The structure considered in the shake table study was a two-story single-span steel moment frame building seismically isolated using four square U-FREIs (Fig. 4.6). The 1/4-scale model building had dimensions of 1500 mm × 1400 mm in plan and a total height of 1628 mm. Three concrete slabs were used on top of the floors in order to provide a rigid diaphragm. Hollow structural sections were used for beams (HSS 76X51X6.4) and columns (HSS 64X64X6.4). The total weight of the isolated structure was  $W = 31.1$  kN to match the average vertical stress of  $p = 1.6$  MPa on the isolators, which was used in the lateral cyclic tests. Three earthquake excitations, i.e., Imperial Valley (1940, USA), Tabas (1978, Iran), and Saguenay (1988, Canada), were considered in the shake table experiments. These ground motions were scaled to satisfy dynamic similitude

requirements. The design spectral acceleration of NBCC [25] considers an earthquake with a 2% probability of exceedance in 50 years (with a return period of approximately 2500 years). This level of earthquake is specified as the maximum considered earthquake (MCE) in ASCE-7 [26]. In order to also investigate the behavior under the design basis earthquake (DBE) level, having 10% probability of exceedance in 50 years, in accordance with ASCE-7 [26] the amplitudes of the MCE-level earthquakes were reduced by 33%. Additional details on the shake table study can be found in [24]. Figure 4.7 shows the scaled MCE-level acceleration histories of the three ground motions. For each ground motion, the acceleration response spectrum is shown for 5, 10 and 15% damping ratios.

#### **4.5.2 Nonlinear Dynamic Analyses**

A series of nonlinear time history analyses were conducted on the isolated two-story steel moment frame structure considered in the shake table experiment. The analyses were carried out using SAP2000 [14]. From the free vibration tests conducted on the 1/4-scale fixed-base model building [24], the fundamental period was found to be 0.14 s with a corresponding damping ratio of 0.6%. The fundamental period of the fixed-base structure obtained from numerical modeling in SAP2000 was calculated to be 0.13 s, which is in agreement with the free vibration test results. The nonlinear dynamic time history analyses were carried out using the Hilber-Hughes-Taylor (HHT) [27] implicit integration method.

## 4.6 Results and Discussions

### 4.6.1 Evaluation of Model

Figure 4.8 compares the normalized isolation displacement response histories obtained from the shake table results and the time history analyses for MCE-level (left) and DBE- level (right) motions. In the Pivot-Elastic model, there is no source of energy dissipation for isolation displacements  $u \leq u_y$ . Thus, the predicted values for the isolation displacement deviates from the values obtained from shake table results for  $u \leq u_y$ . This deviation can be observed in the displacement time history corresponding to the Saguenay-DBE earthquake motion for  $t > 7.5$  s. However, the predicted peak isolation displacement values obtained from time history analyses are in good overall agreement with experimental values, with a maximum discrepancy of 11% for the Tabas-MCE earthquake motion.

Figure 4.9 compares the response histories of the normalized superstructure base shear obtained from the shake table tests and the time history analyses, for MCE- and DBE-level ground motions. The superstructure base shear is calculated by summing the product of the weight of the first and the second stories by their corresponding acceleration, and is normalized with respect to the total weight of the structure,  $W$ . At both MCE and DBE levels, the predictions of the time history analyses are in good overall agreement with the shake table test results. However, similar to the isolation displacement, the predictions of the time history analyses deviate from the shake table results in Saguenay-DBE earthquake for  $t > 7.5$  s. The peak values of the base shear of

the structure is predicted well by the analyses, with a maximum error of 15% in Saguenay-MCE earthquake.

Figure 4.10 compares the normalized hysteresis loops of the isolators obtained from the shake table tests and the time history analyses for MCE-level motions. As can be observed in Fig. 4.10, the peak values of the isolation force and isolation displacement are predicted with good accuracy using the time history analyses.

Table 4.4 compares the peak response values of the isolated structure obtained from the time history analyses carried out using the Pivot-Elastic model, normalized by the corresponding experimental values. Normalized values for the peak response of the isolated structure under MCE-level motions, predicted by the 10-parameter and the bilinear models [12], for both the first and final iterations are also listed in Table 4.4. Overall, the predicted response values from the proposed Pivot-Elastic model are in better agreement with the shake table results, compared to the other two methods. The average difference between the peak response values (isolation displacement and the superstructure base shear) obtained using the Pivot-Elastic model, the last iteration of the 10-parameter model, and last iteration of the bilinear model, with the shake table results for MCE-level motions are 8%, 12% and 11%, respectively. For DBE-level motions, the average error between the peak response values obtained from Pivot-Elastic model and shake table results is found to be less than 5%.

#### 4.6.2 Sensitivity of the Response to $K_{\text{eff}}$ and $\beta_{\text{eff}}$

According to ASCE7-10 [26], a variation of 15% in the effective stiffness of two isolator specimens of the same design is considered acceptable. In order to investigate the

sensitivity of the peak response values of the isolated structure to variations in the effective stiffness and damping ratio of the isolation, a series of analyses were carried out. For this purpose, the values of  $K_{\text{eff}}$  and  $\beta_{\text{eff}}$  obtained from lateral cyclic tests (Table 4.1), each separately were subjected to a change of  $\pm 15\%$  (when a change was considered for effective damping ratio, the values of the effective stiffness were not subjected to any change). Table 4.5 shows the model parameters for each case considered in this study. For each case, the parameters of the Pivot-Elastic model were determined following the procedure described earlier.

The change in the peak response values of the isolated structure for each case is shown in Table 4.6. It is generally expected that increasing the effective stiffness values of the bearings result in a decrease in the isolation displacement, and vice versa. However, the analysis results show that in some cases, increasing the effective stiffness of the FREI results in an increase in peak isolation displacement. This can be explained by considering the spectral displacement for each earthquake. Figure 4.11 shows the spectral displacement for Imperial Valley-MCE and Tabas-MCE earthquakes for 10% damping. For Imperial Valley-MCE, the peak isolation displacement is increased by 4% when the effective stiffness of the bearings is increased by 15%, while for Tabas-MCE, a 26% reduction in the peak isolation displacement is observed. According to the time history analysis results, the corresponding effective isolation period of the structure is  $T = 0.68$  s and  $T = 0.63$  s for Imperial Valley-MCE and Tabas-MCE, respectively. For Imperial Valley-MCE, a 15% increase in the effective stiffness of the isolators reduces the isolation period to  $T = 0.63$  s. For this earthquake and within a period range of

$0.62 < T < 0.68$  s, the spectral displacement values decrease with an increase in the period (Fig. 4.11). Thus, an increase in the peak isolation displacement can be expected by increasing the effective stiffness of the isolators by 15%. For Tabas-MCE earthquake, increasing the effective stiffness values of the isolators by 15% reduces the isolation period to  $T = 0.58$  s. For this earthquake and within a period range of  $0.52 < T < 0.63$ , increasing the period results in an increase in the spectral displacement values. Thus, a reduction in the peak isolation displacement is expected by increasing the effective stiffness of the isolators by 15%. Results of the time history analyses show that in most cases, the superstructure base shear increases with an increase in the effective stiffness of the bearings. The average change in the peak isolation displacement and the peak base shear of the structure due to 15% change (both increase and decrease) in the effective stiffness of the isolators is found to be 11% and 12%, respectively.

Results of the analyses carried out show that in most cases, increasing the damping ratio of the FREIs results in a decrease in the peak isolation displacement. In addition, the peak response values are found to be more sensitive to a change in effective stiffness than to a change in damping ratio. The average change in the peak isolation displacement and the peak base shear of the structure due to a 15% change in damping ratio of the isolators is found to be 4% for both cases.

### 4.6.3 Bonded Versus Unbonded FREI System

Toopchi-Nezhad et al. [2] conducted finite element analysis (FEA) on the FREIs considered in this study and compared their lateral response in both bonded and unbonded application. It was concluded that the isolation system composed of FREIs in unbonded application is not only potentially more cost effective but also more efficient in mitigating the seismic demand on the isolated structures, simply because of its lower effective stiffness compared with the isolation system composed of bonded FREIs.

Time history analyses are carried out to investigate the seismic response of the isolated structure considering FREIs in a bonded application and compare the results with those obtained for U-FREIs. Using the FEA results [2], the ratio of the effective stiffness values of the bonded FREI over the values for the U-FREI is calculated at different displacement amplitudes. The calculated ratios are then multiplied by the experimentally obtained effective stiffness values for the U-FREIs (Table 4.1) to estimate the effective stiffness values for the corresponding bonded isolators. Knowing the effective stiffness values for the bonded FREIs and matching the energy dissipation of the isolators with experimentally obtained values for U-FREIs, the values for the damping ratio of the bonded FREIs at different displacement amplitudes are calculated. Similar to U-FREIs, the Pivot-Elastic model is used to model the lateral response of bonded FREIs in the time history analyses. In determining the Pivot-Elastic model parameters for the bonded isolators, a linear load-displacement relationship is assumed for the elastic spring ( $a_2 = a_3 = 0$ ), since the softening and subsequent stiffening response observed in U-FREIs is not expected in bonded isolators. The parameters of the Pivot-Elastic model for

the bonded FREIs are listed in Table 4.7. Table 4.8 shows the predicted values for the effective stiffness and damping ratio for the bonded FREIs. As can be observed in Table 4.8, the effective stiffness values decrease as the lateral displacement increases. This reduction in the effective stiffness values of bonded isolators is in agreement with the test results conducted on bonded FREIs [28]. Figure 4.12 compares the normalized load-displacement relationship for the bonded and unbonded FREIs predicted by the Pivot-Elastic models.

Table 4.9 compares the time history analysis results for the normalized values of the peak isolation displacement and peak superstructure base shear for the isolated structure considering bonded FREIs for the isolation system. For each earthquake, the peak response values are normalized with respect to the peak response values obtained from time history analyses for the building isolated using U-FREIs. Using bonded FREIs instead of U-FREIs for the isolation system results in an average reduction of 4.5% in the peak isolation displacement. In all earthquake load cases, using bonded FREIs instead of U-FREIs for the isolation system results in an increase in the peak superstructure base shear. This increase in the superstructure base shear is more pronounced in earthquakes with higher peak isolation displacements. For Imperial Valley-MCE for example, using a bonded application for the isolation system results in 49% increase in the peak superstructure base shear. Figure 4.13 compares the normalized hysteresis loops of the bonded FREIs with U-FREIs obtained from the time history analyses for MCE-level ground motions. For Saguenay-MCE, the load-displacement obtained for bonded FREI is similar to the one obtained for the U-FREI. For Tabas-MCE, the peak isolation

displacement and peak isolation force shows 22.0% decrease and 12.0% increase, respectively, when bonded FREIs are used for the isolation system instead of U-FREI. For Imperial Valley-MCE, using bonded FREIs for the isolation system instead of U-FREIs results in 1.8% increase in the maximum and 33.0% decrease in the minimum isolation displacement values, while the peak (absolute) isolation force is increased by 63.5%.

#### **4.7 Summary and Conclusions**

This paper proposes the Pivot-Elastic model for the load-displacement relationship of U-FREIs. The Pivot-Elastic model is a combination of a bilinear Pivot hysteretic model and a nonlinear elastic model. This model is able to predict the variation in the values of effective stiffness and effective damping ratio of the U-FREI isolation system at different displacement amplitudes. Unlike existing models for U-FREIs [12,14,15], using the Pivot-Elastic model to conduct time history analyses does not require iteration, and the model can be implemented into commercially available general-purpose structural analysis software. Another benefit of the Pivot-Elastic model, compared with the existing U-FREIs models, is that determination of the model parameters does not require fitting over the entire hysteresis loops.

A previously tested square U-FREI was considered for the purpose of modeling. Results of the lateral cyclic tests carried out on the isolator were used to calculate the parameters of the Pivot-Elastic model. The model was subsequently used to conduct nonlinear time history analyses, and the results were compared with the results of a shake

table study conducted on a two story steel moment frame structure seismically isolated using four square U-FREIs [24]. A total of three earthquake ground motions, each at two hazard levels, DBE and MCE, were considered in the time history analyses. In terms of the peak values of the isolation displacement and superstructure base shear, the predictions of the model were in good agreement with the shake table results, with the maximum discrepancy observed being less than 15%.

In order to investigate the sensitivity of the peak response values to the variation in the properties of the isolators, a  $\pm 15\%$  change was considered for the values of the effective stiffness and damping ratio of the U-FREIs. Although it is generally expected that increasing the effective stiffness of the isolators results in a reduction in the peak isolation displacement and vice versa, an inverse response was observed for half of the earthquake load cases. The reason being that at certain period ranges, the values of the spectral displacement of each earthquake decrease with an increase in the period (unlike the overall trend of the spectral displacement). The peak response of the isolated structure was found to be less sensitive to variation in the damping ratio than in the effective stiffness.

In order to investigate the effect of different installation applications on the seismic response of the isolated structure, another series of analyses were carried out considering FREIs being employed in a bonded application. The proposed Pivot-Elastic model was used to model the load-displacement relationship of the bonded-FREIs. The properties of the bonded FREI were determined using a previous FEA study conducted on the isolators. In most cases, using FREIs in a bonded application resulted in a small reduction

in peak isolation displacement. Compared with the time history analysis results for the U-FREIs, it was observed that the peak superstructure base shear was increased when bonded FREIs were used for the isolation system. The increase in the base shear was more pronounced in earthquakes with higher peak isolation displacement.

#### **4.8 Acknowledgments**

This research was carried out as part of the mandate of the Centre for Effective Design of Structures (CEDs) at McMaster University and is partially funded by the Ontario Ministry of Economic Development and Innovation and by the Natural Sciences and Engineering Research Council of Canada (NSERC).

#### **4.9 References**

- [1] Toopchi-Nezhad H, Tait MJ, Drysdale RG. Lateral response evaluation of fiber-reinforced neoprene seismic isolators utilized in an unbonded application. *Journal of Structural Engineering* 2008; 134(10):1627-1637.
- [2] Toopchi-Nezhad H, Tait MJ, Drysdale RG. Bonded versus unbonded strip fiber reinforced elastomeric isolators: finite element analysis. *Composite Structures* 2011; 93(2):850-859.
- [3] Toopchi-Nezhad H, Tait MJ, Drysdale RG. Testing and modeling of square carbon fiber-reinforced elastomeric seismic isolators. *Structural Control and Health Monitoring* 2007; 15(6): 876-900.

- [4] Kelly JM. Seismic isolation systems for developing countries. *Earthquake Spectra* 2002; 18(3):385-406.
- [5] Russo G, Pauletta M, Cortesia A. A study on experimental shear behaviour of fiber-reinforced elastomeric isolators with various fiber layouts, elastomers and aging conditions. *Engineering Structures* 2013; 52:422-433.
- [6] Osgooei PM, Tait MJ, Konstantinidis D. Finite element analysis of unbonded square fiber-reinforced elastomeric isolators (FREIs) under lateral loading in different directions. *Composite Structures* 2014; 113:164-173.
- [7] Kelly JM, Konstantinidis D. Low-cost seismic isolators for housing in highly seismic developing countries. in *10th World conference on seismic isolation, energy dissipation and active vibrations control of structures, ASSISi*. Istanbul; 28–31 May 2007.
- [8] Konstantinidis D, Kelly JM, Makris N. Experimental investigations on the seismic response of bridge bearings. Report No. EERC-2008/02, Earthquake Engineering Research Center, University of California, Berkeley; 2008.
- [9] Van Engelen N, Tait MJ, Konstantinidis D. A model of the shear behaviour of unbonded fiber reinforced elastomeric isolators (FREIs) including rollover. *Journal of Structural Engineering*, 2014 (in press).
- [10] Peng TB, Zhang H, Li JZ, Li WX. Pilot study on the horizontal shear behaviour of FRP rubber isolators. *Journal of Vibration and Shock* 2009; 28(1):127–130. In Chinese.

- [11] Kelly JM, Konstantinidis D. *Mechanics of Rubber Bearings for Seismic and Vibration Isolation*, Wiley, Chichester, UK 2011.
- [12] Toopchi-Nezhad H, Tait MJ, Drysdale RG. Simplified analysis of a low-rise building seismically isolated with stable unbonded fiber reinforced elastomeric isolators. *Canadian Journal of Civil Engineering* 2009; 36:1182-1194.
- [13] Hwang JS, Wu JD, Pan TC, Yang G. A mathematical hysteretic model for elastomeric isolation bearings. *Earthquake Engineering & Structural Dynamics* 2002; 31(4):771–789.
- [14] Toopchi-Nezhad H, Tait MJ, Drysdale RG. A novel elastomeric base isolation system for seismic mitigation of low-rise buildings. in 14<sup>th</sup> world conference on earthquake engineering. Beijing, 12–18 October 2008.
- [15] Love JS, Tait MJ, Toopchi-Nezhad H. A hybrid structural control system using a tuned liquid damper to reduce the wind induced motion of a base isolated structure. *Engineering Structures* 2011; 33(3):738-746.
- [16] Computers and Structures Inc. SAP2000: Static and Dynamic Finite Element Analysis of Structures (Version 16.0.0) Analysis Reference Manual, Computers and Structures, Inc., Berkeley 2013.
- [17] Dowell RK, Seible F, Wilson EL. Pivot hysteretic model for reinforced concrete members. *ACI Structural Journal* 1998; 95:607-617.
- [18] AASHTO 1991. Guide specifications for seismic isolation design. American Association of State Highway and Transportation Officials, Washington, D.C.

- [19] Naeim F, Kelly JM. 1999. *Design of Seismic Isolated Structures*, John Wiley, New York.
- [20] Hwang JS, Sheng LH. Equivalent elastic seismic analysis of base-isolated bridges with lead-rubber bearings. *Engineering Structures* 1993; 16(3):201-209.
- [21] Hwang JS, Sheng LH. Effective stiffness and equivalent damping of base-isolated bridges. *Journal of Structural Engineering* 1994; 119(10):3094-3101.
- [22] Makris N, Kampas G. The engineering merit of the “effective period” of bilinear isolation systems. *Earthquakes and Structures* 2013; 4(4): 397-428.
- [23] Kelly JM. *Earthquake-resistant design with rubber*. 2nd ed. London: Springer-Verlag; 1997.
- [24] Toopchi-Nezhad H, Tait MJ, Drysdale RG. Shake table study on an ordinary low-rise building seismically isolated with SU-FREIs (stable unbonded-fiber reinforced elastomeric isolators). *Earthquake Engineering and Structural Dynamics* 2009; 38(11):1335-1357.
- [25] National Building Code of Canada. Institute for Research in Construction, National Research Council of Canada, Ottawa, 2010.
- [26] Minimum design loads for buildings and other structures. *ASCE/SEI 7-10*, American Society of Civil Engineers, ASCE, New York, 2010.
- [27] Hilber HM, Hughes TJR, Taylor RL. Improved numerical dissipation for time integration algorithms in structural dynamics. *Earthquake Engineering and Structural Dynamics* 1977; 5:283–292.

- [28] Ashkeari GD, Aghakouchak AA, Kokabi M. Design, manufacturing and evaluation of the performance of steel like fiber reinforced elastomeric seismic isolators. *Journal of Materials Processing Technology* 2008; 197:140-150.

Table 4.1. Equivalent linear properties of the U-FREIs obtained from cyclic tests

$u/t_r$	$K_{\text{eff}} \times (t_r/GA)$	$\beta_{\text{eff}} (\%)$
0.25	1.590	13.7
0.50	1.195	11.9
0.75	1.001	10.2
1.00	0.866	9.4
1.50	0.707	9.9
2.00	0.664	9.4

Table 4.2. Parameters of the Pivot-Elastic model

$K_1 \times (t_r/GA)$	$K_2 \times (t_r/GA)$	$u_y/t_r$	$a_1 \times (t_r/GA)$	$a_2 \times (t_r^3/GA)$	$a_3 \times (t_r^5/GA)$
2.139	0.193	0.075	7.642e-1	-2.374e-1	3.551e-2

Table 4.3. Effective stiffness and damping ratio values corresponding to the model

$u/t_r$	Damping ratio		Effective stiffness	
	$\beta_{\text{eff}} (\%)$	Error (%)	$K_{\text{eff}} \times (t_r/GA)$	Error (%)
0.25	13.7	0.2	1.526	4.0
0.50	11.9	2.3	1.192	0.3
0.75	10.2	1.2	1.030	2.8
1.00	9.4	4.3	0.902	4.2
1.50	9.9	0.0	0.701	0.8
2.00	9.4	2.6	0.648	2.4

Table 4.4. Comparison of peak response quantities predicted by different models. Quantities are expressed as ratios of predicted-to-experimentally measured values

Earthquake	Response	Non-iterative Pivot-Elastic	10-Parameter 1st iteration	10-Parameter last iteration	Bilinear 1st iteration	Bilinear last iteration
Imperial	$u_{\max}$	1.01	0.83	0.84	0.86	0.89
Valley-MCE	$V_b$	0.86	0.83	0.84	0.77	0.97
Imperial	$u_{\max}$	1.01	-	-	-	-
Valley-DBE	$V_b$	1.03	-	-	-	-
Tabas-MCE	$u_{\max}$	1.11	1.14	1.10	1.05	0.87
	$V_b$	0.99	0.97	1.04	1.00	1.09
Tabas-DBE	$u_{\max}$	0.98	-	-	-	-
	$V_b$	0.94	-	-	-	-
Saguenay- MCE	$u_{\max}$	0.97	0.92	0.92	0.94	0.93
	$V_b$	0.85	0.83	0.84	0.62	0.77
Saguenay- DBE	$u_{\max}$	0.94	-	-	-	-
	$V_b$	0.87	-	-	-	-

Table 4.5. Parameters of the Pivot-Elastic model considering the change in values of effective stiffness and effective damping ratio of the FREIs

	$K_1 \times (t_r/GA)$	$K_2 \times (t_r/GA)$	$u_y/t_r$	$a_1 \times (t_r/GA)$	$a_2 \times (t_r^3/GA)$	$a_3 \times (t_r^5/GA)$
$K_{\text{eff},+15\%}$	2.463	0.222	0.075	9.064e1	-7.761e-2	3.205e-5
$K_{\text{eff},-15\%}$	1.821	0.164	0.075	6.700e1	-5.736e-2	2.369e-5
$\beta_{\text{eff},+15\%}$	2.681	0.234	0.065	7.087e1	-6.191e-2	2.551e-5
$\beta_{\text{eff},-15\%}$	1.699	0.155	0.084	8.698e1	-7.382e-2	3.057e-5

Table 4.6. Normalized peak response values of the isolated structure for different cases

	Effective Stiffness				Effective Damping Ratio			
	Isolation Disp.		Base Shear		Isolation Disp.		Base Shear	
	+15%	-15%	+15%	-15%	+15%	-15%	+15%	-15%
Imperial Valley MCE	1.04	0.94	1.12	0.82	0.94	1.06	1.02	0.99
Imperial Valley DBE	0.99	0.98	0.98	0.73	0.94	1.06	0.83	0.88
Tabas MCE	0.74	1.26	1.10	1.05	0.96	1.03	1.00	1.01
Tabas DBE	0.90	1.36	1.02	0.90	1.01	1.08	1.07	1.02
Saguenay MCE	1.01	1.04	1.09	0.85	0.96	1.01	0.99	0.97
Saguenay DBE	1.04	0.92	1.19	0.88	0.95	0.97	1.02	1.01

Table 4.7. Parameters of the Pivot-Elastic model for the bonded FREI

$K_1 \times (t_r/GA)$	$K_2 \times (t_r/GA)$	$u_y/t_r$	$a_1 \times (t_r/GA)$
1.999	0.136	0.090	8.144e-1

Table 4.8. Predicted properties for the bonded FREI

$u/t_r$	$K_{\text{eff}} \times (t_r/GA)$	$\beta_{\text{eff}} (\%)$
0.25	1.590	13.2
0.50	1.282	11.3
0.75	1.179	9.3
1.00	1.128	8.0
1.50	1.076	6.4
2.00	1.051	5.5

Table 4.9. Peak response values of the isolated structure considering bonded FREIs normalized with respect to the corresponding peak response values for the U-FREIS

	Isolation Disp.	Base Shear
Imperial Valley MCE	1.04	1.49
Imperial Valley DBE	0.97	1.09
Tabas MCE	0.78	1.16
Tabas DB	0.94	1.09
Saguenay MCE	1.00	1.03
Saguenay DBE	1.04	1.08

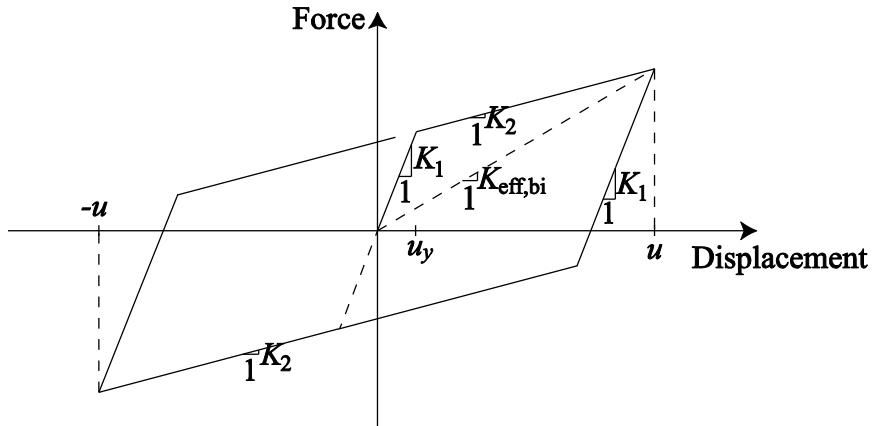


Figure 4.1. Bilinear model

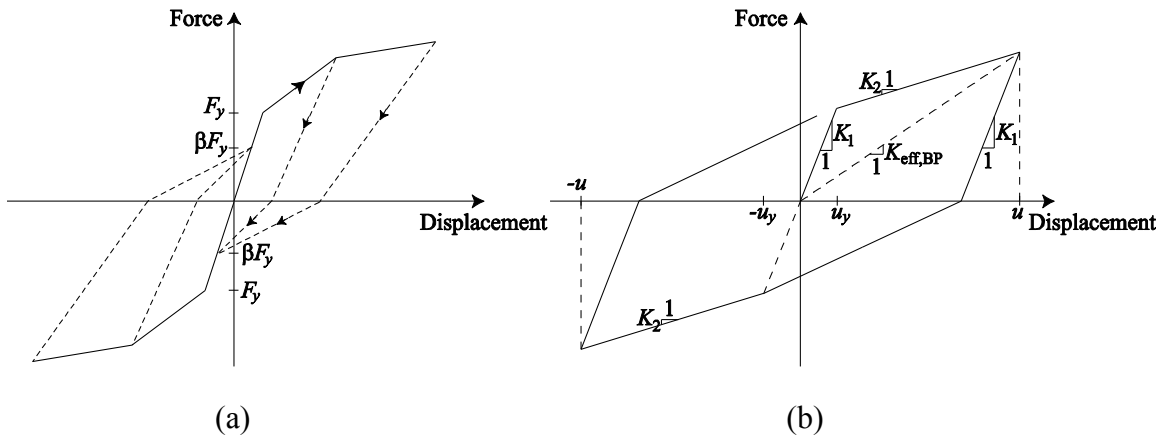


Figure 4.2. Pivot hysteresis models: (a) the general case, (b) the simplified bilinear Pivot case

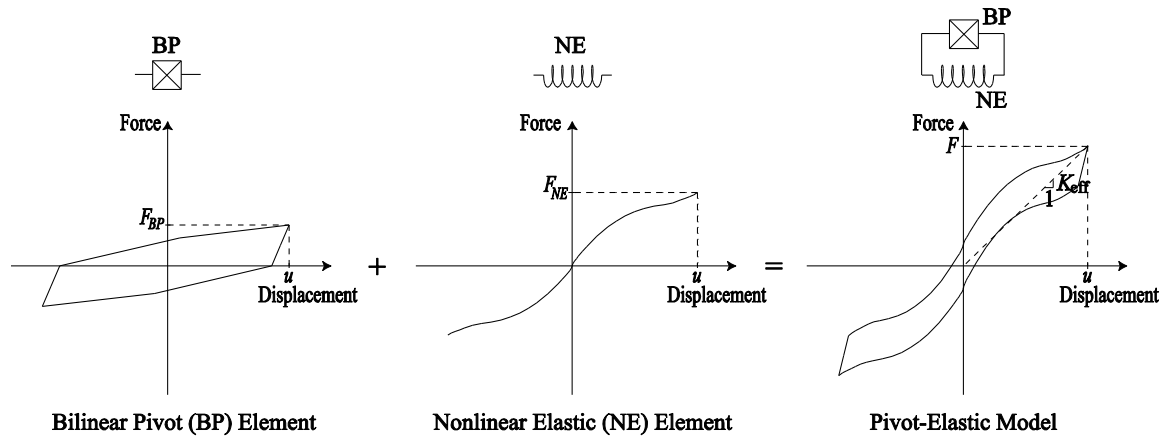


Figure 4.3. Definition of the Pivot-Elastic model

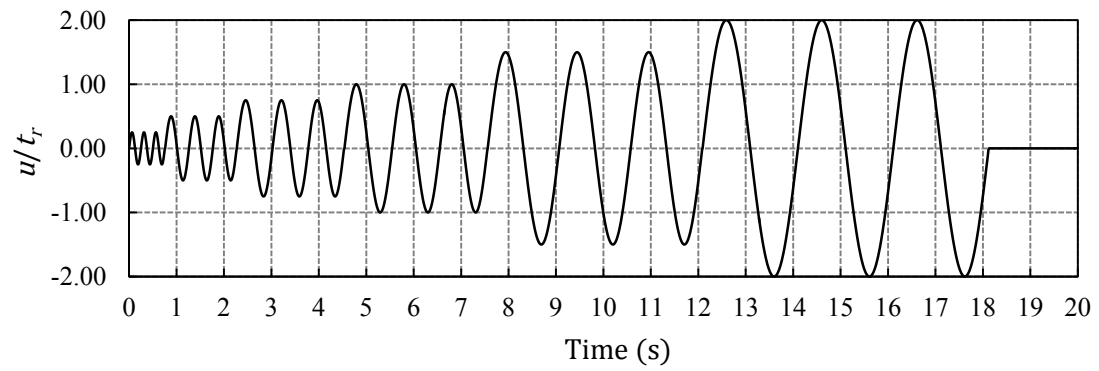


Figure 4.4. Time history of the input lateral displacement in the cyclic testing on U-FREIs

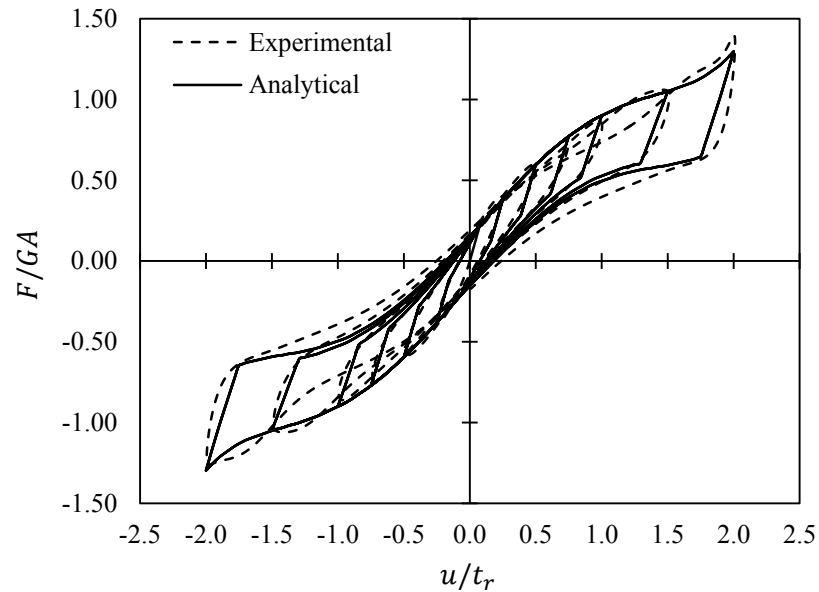


Figure 4.5. Comparison of the uncracked response of the FREIs with the prediction of the model

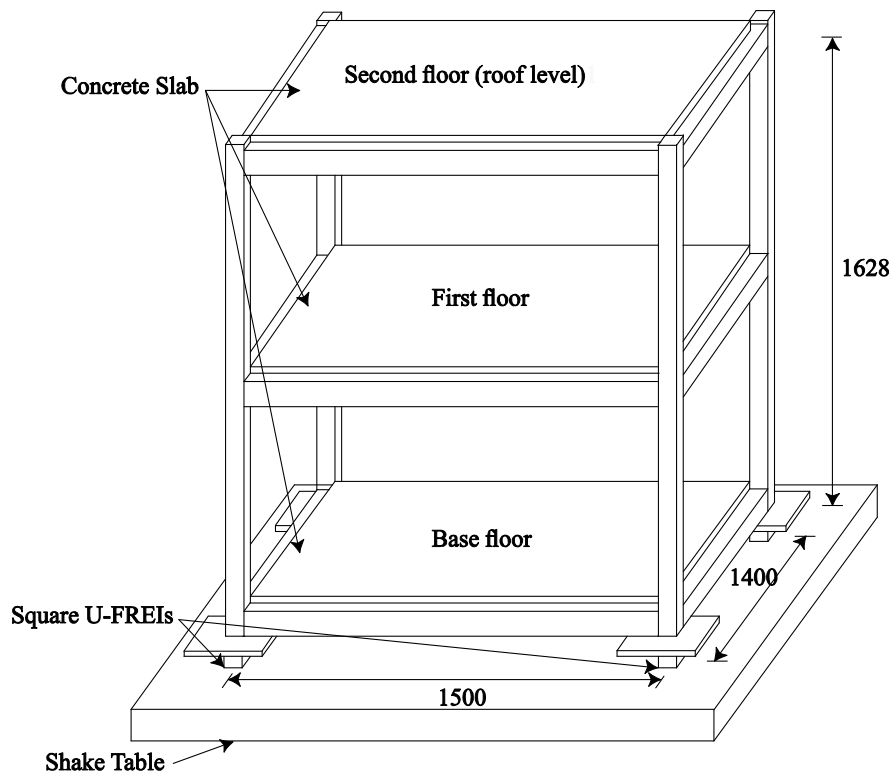


Figure 4.6. Schematic view of the base isolated structure considered in the shake table tests (all dimensions in mm)

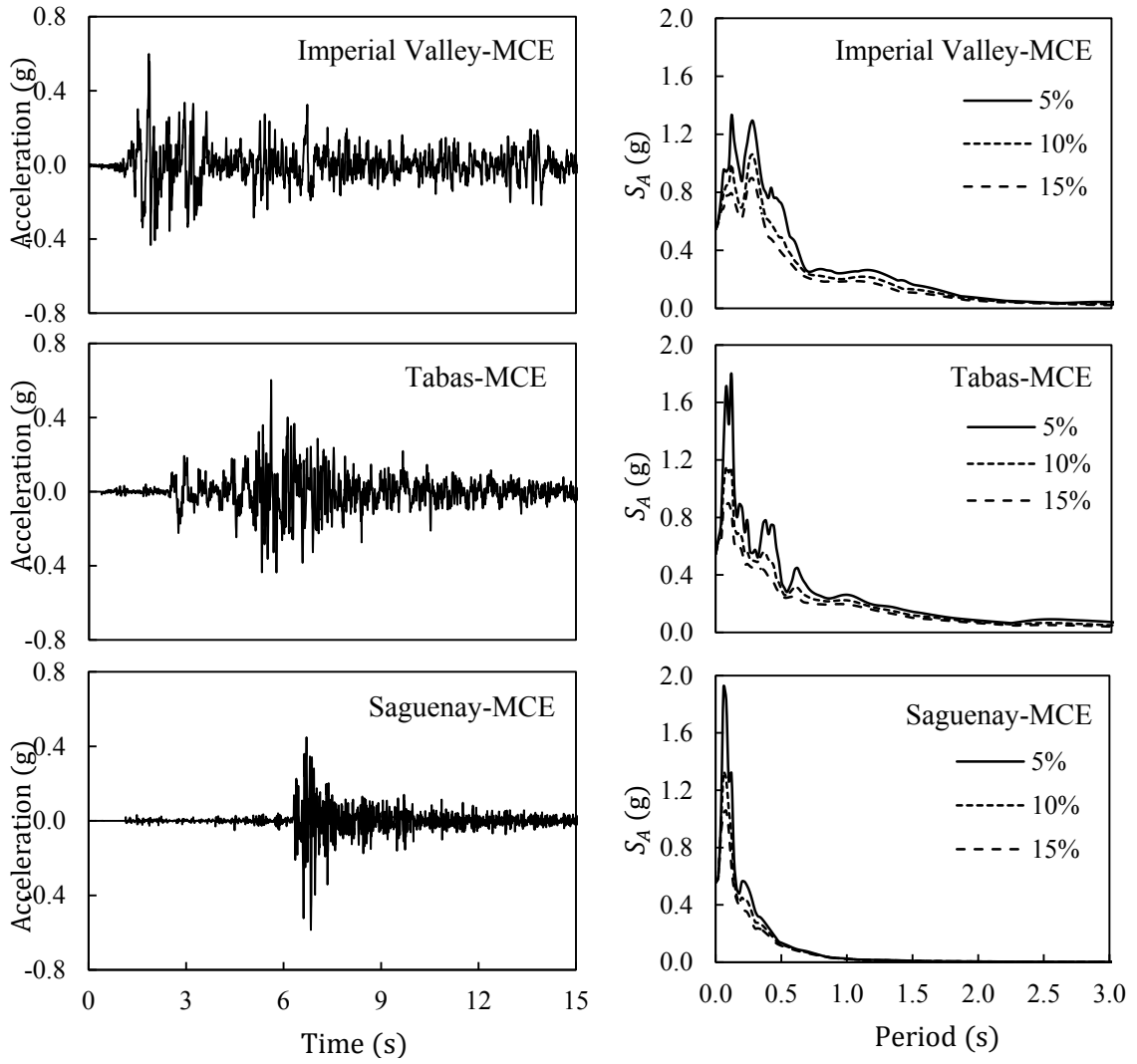


Figure 4.7. Acceleration time histories (left) and acceleration response spectra (right) of the MCE-level ground motions

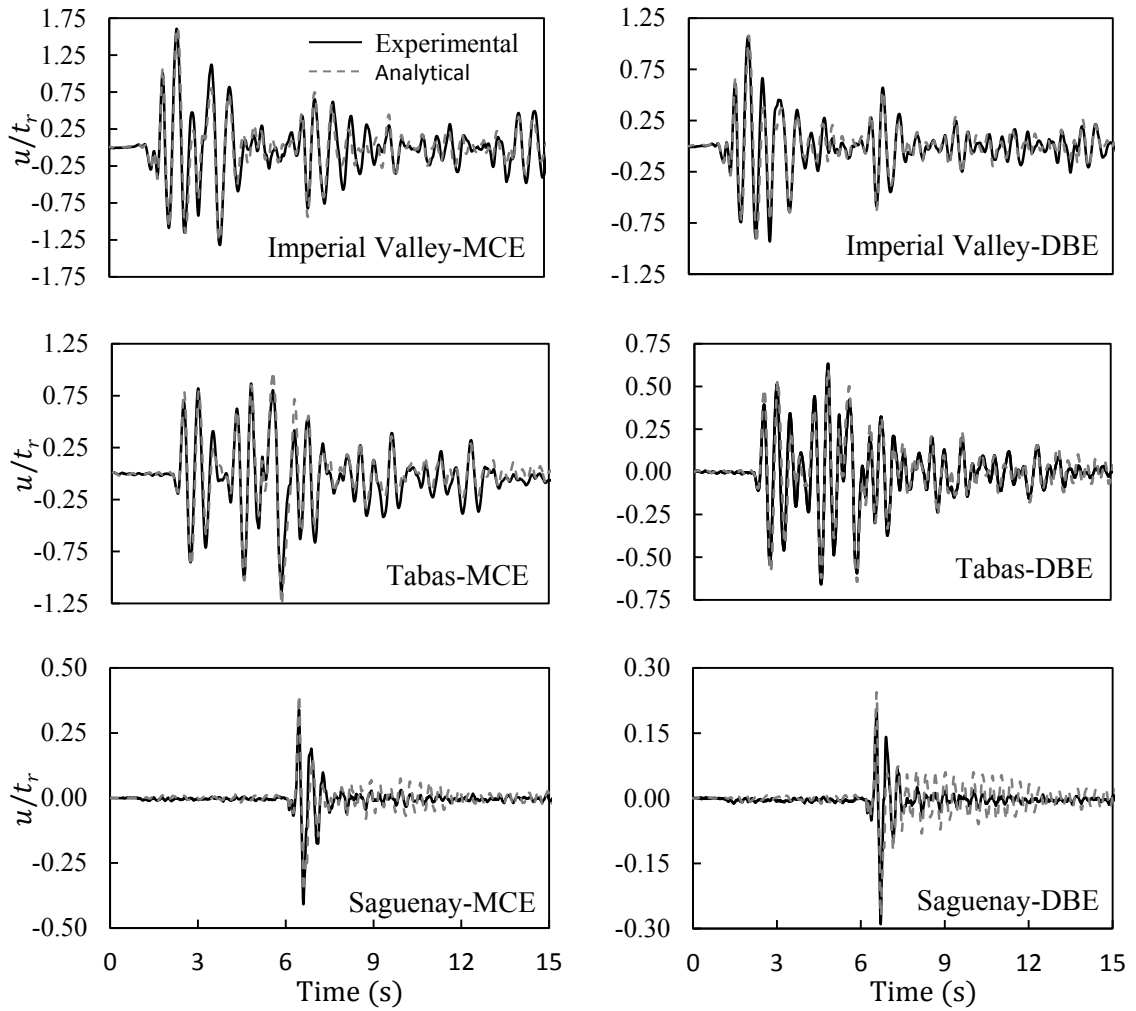


Figure 4.8. Comparison of the isolation displacement time histories obtained from shake table tests and time history analyses

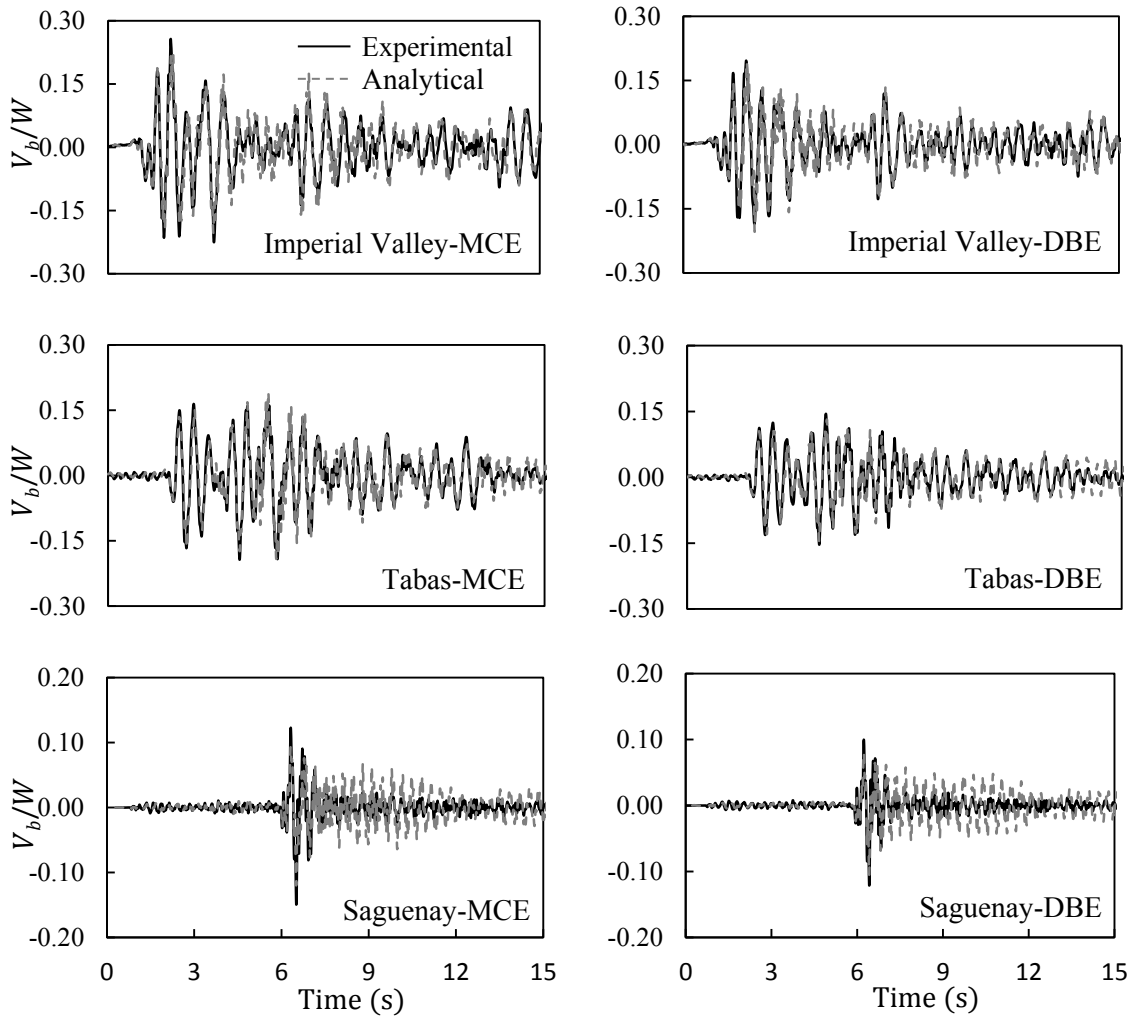


Figure 4.9. Comparison of the response histories of superstructure base shear obtained from shake table tests and the time history analyses for MCE-level ground motions

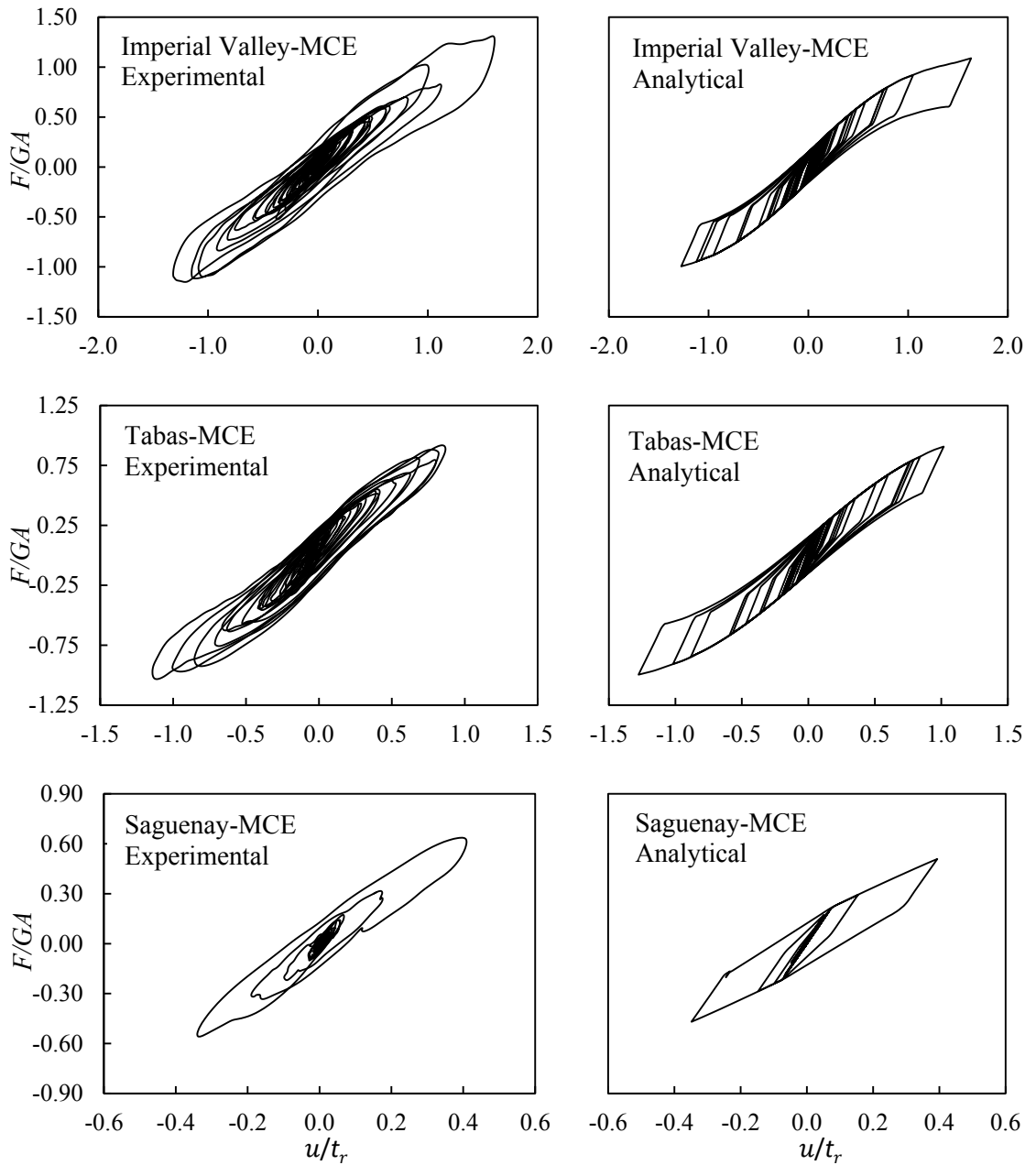


Figure 4.10. Comparison of the hysteresis loops of the U-FREIs obtained from shake table and time history analyses for MCE-level ground motions

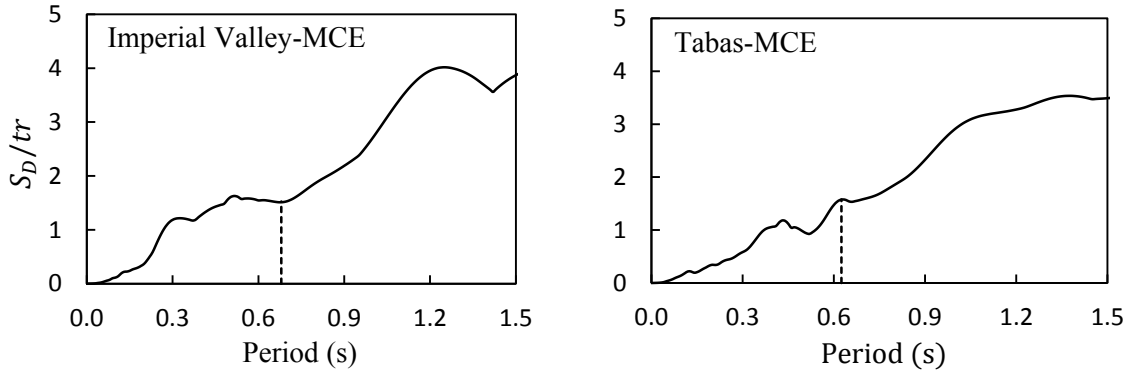


Figure 4.11. Normalized spectral displacement of Imperial Valley-MCE and Tabas-MCE earthquake motions for 10% damping

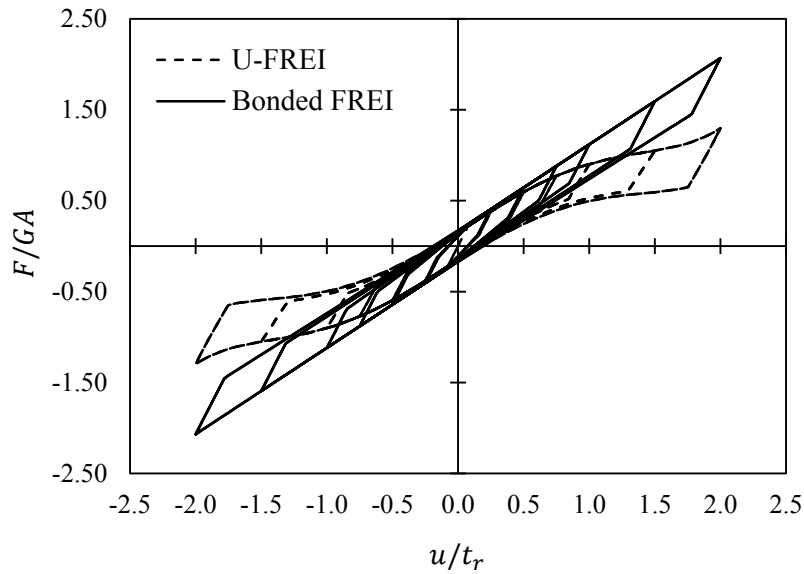


Figure 4.12. Force-displacement relationship of bonded FREI vs U-FREI

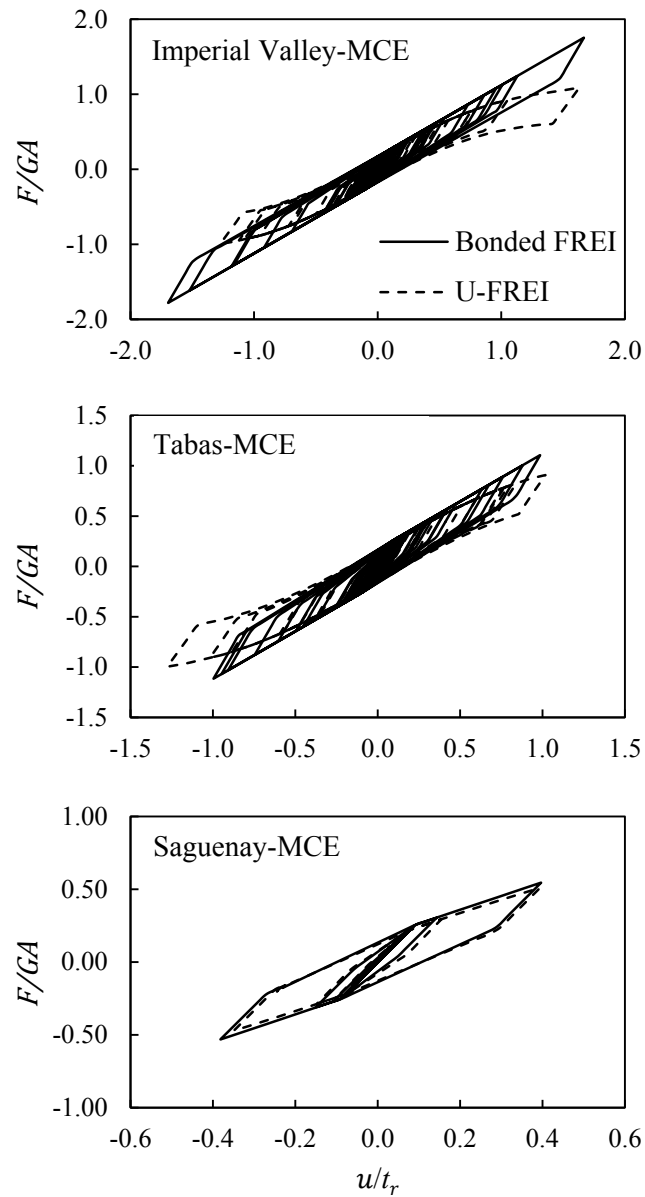


Figure 4.13. Comparison of the hysteresis loops of bonded FREIs and U-FREIs obtained from time history analyses for the MCE-level ground motions

## **Chapter 5: Experimental and Finite Element Study on the Lateral Response of Modified Rectangular Fiber-Reinforced Elastomeric Isolators (MR-FREIs)**

### **Abstract**

Fiber-reinforced elastomeric isolators (FREIs) have been shown to be viable and potentially inexpensive devices for seismic mitigation of low-rise buildings. FREIs utilize fiber material for the reinforcing layers resulting in lower weight and manufacturing costs compared to conventional steel-reinforced elastomeric isolators (SREIs). Experimental test results have shown that modifying FREIs, by cutting holes in the center portion of the isolators or removing sections from the sides, can enhance their lateral response characteristics. This study investigates the lateral response of modified rectangular FREIs (MR-FREIs) through experimental tests and 3D finite element analysis. Experimental test results of five FREIs with and without modifications are used to evaluate the 3D finite element models. These models are subsequently used to investigate the effect of modifications on the lateral behavior of the isolators, in addition to the stress and strain demands in the elastomer and fiber reinforcement layers.

### **5.1 Introduction**

The application of seismic isolation in North America is limited almost entirely to expensive or high-importance structures, or buildings housing sensitive equipment. This limited use is largely due to the high manufacturing and installation costs of seismic isolation devices, the most common type among them being the steel-reinforced

elastomeric isolator (SREI). Kelly [1] suggested that the weight and cost of elastomeric isolators can be reduced by replacing the steel reinforcing plates with fiber reinforcement. The fiber-reinforced elastomeric isolator (FREI) is a relatively new type of laminated rubber isolator that aims to reduce the high costs associated with conventional elastomeric isolators [1-7]. The introduction of cost-effective seismic isolation devices is necessary to make it economically feasible to use base isolation systems in ordinary residential and commercial buildings.

Previous studies [1-3, 8-13] have shown, through vertical compression and lateral cyclic tests, that FREIs achieve both adequate vertical stiffness and the required lateral flexibility to render them suitable for seismic isolation. In order to reduce the construction costs, FREIs can be installed without bonding or fastening the isolator to the contact supports (unbonded application). Due to the unbonded application in conjunction with the low flexural rigidity of the fiber reinforcement, these isolators undergo a unique rollover deformation, which has been shown [14] to increase the efficiency of the isolator by reducing its effective lateral stiffness. In unbonded FREIs, the shear force from the superstructure is transferred to the foundation through friction, which develops along the interfaces between the isolator and its supports [15]. Toopchi-Nezhad et al. [16] conducted shake table tests on a two-story steel structure seismically isolated using four square stable unbonded fiber-reinforced elastomeric isolators (SU-FREIs). Comparing the seismic response of the fixed-base and isolated structure at the maximum considered earthquake (MCE) level, it was observed that the base shear, roof acceleration and maximum inter-story drift were reduced on average by 81%, 75% and 68%, respectively,

in the isolated structure. A 2D finite element analysis (FEA) [14] comparing the lateral response of FREIs in bonded and unbonded applications showed that the stress demands on both the elastomer and fiber reinforcement layers are reduced in the unbonded application. This lower stress demand on the bond between the elastomer and reinforcement makes it possible to use a simpler manufacturing process [14].

In order to seismically isolate buildings with concrete or masonry structural walls, it has been proposed that using strip isolators could result in a more cost-effective isolation system compared to one that uses circular or square shaped isolators [1,2,4,5]. Figure 5.1 compares the application of base isolation on a masonry wall, using square and long rectangular (strip) isolators. When using square (or circular) isolators to seismically isolate buildings with structural walls, additional wall beams are needed to span between isolators in order to support the walls. By using rectangular isolators, a more uniform support can be provided along the walls, which results in a reduction in both the size and reinforcement requirement or potentially the complete elimination of the wall beams. One of the benefits of using fiber reinforcement in lieu of steel is the ability to manufacture large rectangular pads and subsequently cut individual isolators from the pads to the required shape and size [1].

The efficiency of the isolation system is a function of the ratio of the isolation period to the fundamental period of the fixed-base structure [17]. Using strip isolators increases the total plan area of the isolation system, and consequently increases the lateral stiffness of the isolation system, thereby reducing its efficiency. Although using an elastomer with a lower shear modulus can reduce the lateral stiffness of the isolators, the desired lateral

stiffness may not be achievable due to practical limitations in the shear modulus of elastomer compounds used for engineering applications. An alternative approach is to modify the geometry of strip FREIs to enhance their lateral response characteristics. Van Engelen et al. [18] showed that modifying rectangular FREIs by cutting holes in the center portions of the isolators reduces their effective lateral stiffness while increasing their energy dissipation characteristics. This reduction in the lateral stiffness and increase in the effective damping of the modified isolators results in a more efficient seismic isolation system.

The lateral response of unbonded FREIs is complex and few closed-form solutions [3, 5, 19-21] are available in the literature. FEA has been used by researchers [14, 22-27] to model and analyze their lateral response behavior. FEA has also been used by Van Engelen et al. [28] to study the influence of introducing holes and modifications on the vertical stiffness and compression modulus of modified rectangular FREIs (MR-FREIs).

In this study, the lateral response of MR-FREIs is investigated through an experimental test program and a parametric study utilizing 3D FEA. The experimental program included lateral cyclic tests of five MR-FREIs: one unmodified and four modified isolators with two modification configurations and two modification diameters. Experimental data are used to validate the finite element (FE) models. The FE models are subsequently used to perform a parametric study to investigate the effect of various modification characteristics on the lateral response of the isolators. Furthermore, the effect of these modifications on the stress and strain distributions in the elastomer and reinforcement layers are examined.

## 5.2 Experimental Testing

### 5.2.1 Isolator Design

The quarter-scale specimens considered in this study are the same as the specimens used to investigate the vertical behavior of MR-FREIs in Van Engelen et al. [28] with the addition of an *unmodified* rectangular FREI, designated as C1. The specimens were manufactured in large pads using seven layers of neoprene, with a specified hardness of 40 Durometer (Shore A), according to the design described in Foster [29]. The five interior layers of neoprene each had a thickness of  $t = 3.18$  mm, and the two exterior layers of neoprene were each half the thickness of the interior layers, i.e.,  $t = 1.59$  mm. The total height of the elastomeric layers,  $t_r$ , was 19.05 mm. Reinforcement was provided by bidirectional plain weave carbon fiber with a 0.25 mm thickness, which was bonded to the layers of neoprene using a cold vulcanizing agent. The subsequent fiber reinforcement matrix layer thickness was approximately 0.55 mm. The total height,  $h$ , of the isolators was 22.35 mm. The large pads were cut to the desired plan dimensions of width  $2a = 76$  mm and length  $2b = 52$  mm.

Two geometric configurations with two diameters were considered, as shown in Fig. 5.2. The circular modifications had a diameter,  $d$ , of 18 mm and 24 mm, which, when normalized by the length can be expressed as  $d/2b = 0.35$  and 0.46, respectively. The geometric characteristics of the specimens are summarized in Table 5.1. The modifications were interior, I, or exterior, E, and the specimens are designated with the percent normalized diameter and letter corresponding to the modification placement. For example, C2-46I refers to C2 with an interior modification with a diameter of  $d/2b =$

0.46. C2-46I and C3-35I were each modified with a circular hole placed at the geometric center of the isolator, referred to as an interior modification. Exterior modifications were made to C4-46E and C5-35E by removing a half-circle from the center of the 76 mm width on either side. Specimen C1 was left unmodified as the control specimen. The plan loaded area of the unmodified specimen,  $A_u$ , was reduced by 6.4% and 11.4% for  $d/2b = 0.35$  and 0.46 modifications, respectively. By considering both interior and exterior modifications, specimens of identical loaded area but different shape factor,  $S$ , (defined for a single elastomer layer as the ratio of loaded area to the area that is free to bulge) can be investigated.

### 5.2.2 Experimental Setup and Lateral Test Procedure

The experiment was conducted under vertical load control and lateral displacement control. Each isolator was placed unbonded between two level steel plates and loaded monotonically to a vertical load of 7.9 kN, corresponding to an average vertical compressive stress of 2.0 MPa based on the unmodified plan area. Each specimen was tested under the same compressive load to represent the application of the isolators to the same structure. Three fully reversed sinusoidal cycles along the  $x$  direction were conducted at seven displacement amplitudes (0.25, 0.50, 0.75, 1.00, 1.50, 2.00 and  $2.50 t_r$ ) at a constant rate of 76.2 mm/s. The specimens were monotonically unloaded after a total of 21 cycles were completed and visually inspected for damage. The experimental setup is illustrated in Fig. 5.3. The vertical load was applied with a vertical actuator and was measured using three load cells. The horizontal displacement was

measured with a single LVDT and the horizontal load was measured directly with a single load cell. The horizontal load was applied by a horizontal actuator which displaces the lower platen.

### 5.2.3 Experimental Results

#### 5.2.3.1 Effective Lateral Stiffness

The experimental hysteresis loops for the five test specimens are shown in Fig. 5.4. The lateral force,  $F$ , is normalized by  $GA_u$ , where  $G = 0.43$  MPa is the shear modulus of the neoprene obtained from a simple shear test conducted on a neoprene test specimen at 100% shear deformation. The lateral displacement,  $u$ , is normalized by  $t_r$ . It can be seen that all specimens exhibited the characteristic softening and subsequent stiffening response associated with FREIs and maintain horizontal stability over all cycles and the entire displacement range. In all cases, the stiffening initiates over the  $u/t_r = 2.00$  amplitude, which corresponds to the cycle at which the originally vertical faces of the isolator contact the loading surfaces (hereinafter referred as *full rollover*). A detailed description of full rollover (also referred as full contact) can be found in [23].

Figure 5.5 compares the first  $u/t_r = 2.50$  cycle of the modified specimens with the control specimen C1. Specimen C5-35E was found to have the highest effective lateral stiffness, whereas C2-46I was found to have the lowest stiffness in the intermediate displacement amplitudes from  $u/t_r = 0.50$  to  $u/t_r = 2.00$ . Specimen C4-46E and C5-35E decrease notably in normalized lateral force although the shape of the hysteresis loops is comparable to the control specimen. A significant change in the hysteretic

response was obtained by introducing an interior modification as shown for specimen C2-46I and C3-35I. The normalized lateral force, which maintains a positive slope, is nearly constant up to  $u/t_r = 1.50$ . At  $u/t_r = 2.00$ , the normalized lateral force increases substantially as a consequence of full rollover. Thus, two different stiffness regimes can be distinguished in the hysteresis loops of the isolators with interior modifications, while for the unmodified isolator and isolators with exterior modifications, three different stiffness regimes are observed.

Figure 5.6 shows the effective stiffness of the specimens normalized by the effective stiffness of the control specimen, i.e.,  $K_e/K_e^{C1}$ , as a function of  $u/t_r$  for the first cycle of loading. The figure highlights the improvement in the isolation efficiency of unbonded FREIs by the introduction of modifications. The interior and exterior modifications displayed similar trends in comparison to each other. The normalized effective stiffness for exterior modifications remains nearly constant, whereas for interior modifications it is largely dependent on the displacement. Average  $K_e/K_e^{C1}$  values of 0.78 and 0.88 over the first cycle were obtained for specimens C4-46E and C5-35E, respectively. In both cases, the decrease in effective lateral stiffness was larger than what can be related to the plan area removed by the modification alone. This can be attributed to an increase in the portion of the isolator that rolls over, with respect to the total volume, when a modification is introduced. Isolators with interior modification showed a stiffening behavior at  $u/t_r > 1.5$ , compared to the control specimen.

### 5.2.3.2 Energy Dissipation Characteristics

The equivalent viscous damping of the control specimen ranged between 12.9 % at  $u/t_r = 0.25$  and 7.5 % at  $u/t_r = 2.50$ . The damping was larger than the value expected from the inherent damping of the elastomer, with the additional damping being attributed to the inter-fiber movements of the fiber reinforcement during lateral displacement [1]. In all cases, the modification increased the equivalent viscous damping, although this is partially attributed to the decrease in effective lateral stiffness. Figure 5.7 compares the energy dissipation of the specimens normalized by the energy dissipation of the control specimen as a function of  $u/t_r$ . The interior modifications caused an increase in the area contained within the hysteresis loops over the entire displacement range, whereas the exterior modification resulted in a decrease. The magnitude of change in energy dissipated increases with increasing modification size. It is postulated that the interior modification, which causes greater disruption to the fiber reinforcement continuity, induced additional inter-fiber movement, thereby increasing the energy dissipation characteristics. The exterior modification reduced the area enclosed within the hysteresis loops by a maximum of 12 %, whereas the interior modification increased it by a maximum of 20 %.

## 5.3 Evaluation of Finite Element Models

Three dimensional FEA was used to investigate the lateral behavior of the five FREIs listed in Table 5.1. The analysis was carried out using MSC Marc [30], a general purpose FEA software. The ability to model nonlinear materials, complex contact

analysis under large deformations and large strains, together with integrated adaptive remeshing capabilities makes MSC Marc [30] well suited for the analysis of FREIs. Due to the nonlinear stress-strain relationship of elastomers, a hyperelastic constitutive model, based on the strain energy density function  $W$ , was used to model the neoprene. The *James-Green-Simpson* [31, 32] third-order strain energy function defined by

$$W = C_{10}(I_1 - 3) + C_{01}(I_2 - 3) + C_{11}(I_1 - 3)(I_2 - 3) + C_{20}(I_1 - 3)^2 + C_{30}(I_1 - 3)^3 \quad (5.1)$$

was employed in this study.  $I_1$  and  $I_2$  are the first and second invariants of the left Cauchy-Green strain tensor  $B_{ij}$  and  $C_{10}$ ,  $C_{01}$ ,  $C_{11}$ ,  $C_{20}$  and  $C_{30}$  are material constants. The Cauchy stress components  $\sigma_{ij}$  can be obtained from the strain energy function using [33]

$$\sigma_{ij} = -p\delta_{ij} + 2\frac{\partial W}{\partial I_1}B_{ij} - 2\frac{\partial W}{\partial I_2}B_{ij}^{-1} \quad (5.2)$$

where  $p$  is the hydrostatic pressure and  $\delta_{ij}$  is the Kronecker delta. The strain energy function in Eq. (5.1) reduces to the neo-Hookean hyperelastic model when  $C_{01} = C_{11} = C_{20} = C_{30} = 0$ . In this study, the *James-Green-Simpson* model constants are obtained using curve fitting of data from simple shear and biaxial extension tests and are listed in Table 5.2.

The fiber reinforced matrix was modeled using a linear elastic isotropic material, with an elastic modulus of  $E_f = 23$  GPa, based on uniaxial tensile tests results. In order to account for the negligible flexural stiffness of fiber reinforcement layers, four-node

membrane elements with zero flexural rigidity were used to model the reinforcement layers.

As in the experimental test program, a compression load of 7.9 kN (corresponding to an average vertical stress of 2.0 MPa based on the unmodified plan area) was applied to the isolators and was held constant while they were subjected to monotonically increasing lateral displacements. Modeling the rollover deformation of FREIs requires that the nodes of the elastomer layer elements detach from the top and bottom supports when the normal compression stress reaches zero. For this purpose, a touching contact [30] was defined between the elastomer elements and the support surfaces, which were modeled as rigid. The rubber material is modeled using eight-node linear full integration isoparametric hexahedron elements. Figure 8 shows the finite element model of isolator C2-46I.

Figure 5.9 compares the normalized lateral load-displacement relationships of the isolators obtained from FEA with the experimental test results. Good agreement was observed between the experimental and FEA results. The largest deviation was found to occur for C2-46I, for which the lateral force values predicted by the FEA is lower than the experimental results up to  $u/t_r = 1.00$ . The good agreement between FEA and the experimental results observed in this study as well as in [22, 23] provided confidence in the modeling assumptions made.

#### **5.4 Effect of Modification Characteristics**

A parametric study was performed in order to determine the influence of different modifications on the lateral response of MR-FREIs. Interior and exterior circular

modifications with diameters ranging from  $d/2b = 0.12$  to 0.58 were investigated. Table 5.3 shows the properties of the isolators considered in the parametric study.

#### 5.4.1 Load-Displacement Relationships

Figures 5.10 and 5.11 show the load-displacement relationships obtained from FEA for isolators with exterior and interior modifications, respectively. The curves show that as the modification diameter increases, the lateral stiffness of the isolator decreases. The rate of the decrease in the effective stiffness increases as the modification diameter increases. At  $u/t_r = 1.00$ , for example, the reduction in the effective lateral stiffness in comparison to the unmodified isolator is 5.1%, 13.3%, 24.5%, 39.8% and 60.9% in isolators 12I, 23I, 35I, 46I and 58I, respectively. Within the displacement range considered, all isolators showed a stiffening behavior at larger displacements. The displacement at which this stiffening occurs depends on the modification diameter. In the unmodified isolator, stiffening is observed to occur at  $u/t_r = 1.75$ , which changes to  $u/t_r = 1.74$  and  $u/t_r = 1.79$  for isolators 12E and 12I, while in isolators 58E and 58I, the lateral displacement at which the stiffening occurs is  $u/t_r = 1.58$  and  $u/t_r = 1.20$ , respectively. The reason for this change in the displacement at which stiffening is observed in the isolators modified with interior and exterior modifications is related to the change in the deformed shapes of the isolators and will be discussed later.

Figure 5.12 compares the load-displacement relationships for isolators modified with interior and exterior modifications. For a given  $d/2b$  value, the effective stiffness of isolators with interior modifications is lower than the effective stiffness of isolators with

exterior modifications. As the modification diameter increases, the difference between the effective stiffness values between interior and exterior modified isolators with the same  $d/2b$  value increases; the difference is observed to reduce at  $u/t_r > 0.95$ .

#### 5.4.2 Stress and Strain in Elastomer Layers

When loaded laterally, unbonded FREIs experience large displacements and rotations and thus defining local coordinates for the stresses and strains is important. Figure 5.13 shows the definition of the local stress in one elastomer element, before and after the lateral displacement is applied. Initially,  $\sigma_{11}$ ,  $\sigma_{22}$  and  $\sigma_{33}$  are parallel to the global directions of  $x$ ,  $y$  and  $z$ . As the lateral displacement increases, the local coordinates update with the displacements and rotations of the elements. In this study, the stress values in the elastomer and fiber reinforcement layers are normalized with respect to the average vertical stress ( $\bar{p} = 2$  MPa). For this purpose, the following normalized stresses are defined:  $S_{11} = \sigma_{11}/\bar{p}$ ,  $S_{22} = \sigma_{22}/\bar{p}$  and  $S_{33} = \sigma_{33}/\bar{p}$ .

Figure 5.14 shows the contours of  $S_{11}$  in the center elastomer layers in the unmodified isolator and modified isolators 12I, 35I, 35E, 58I and 58E, under pure compression. FEA results show that a small exterior modification has minor effect on the behavior of the modified isolator and the stress distribution is similar to that of the unmodified isolator. Therefore, isolator 12E has been excluded from the comparison. An extended discussion on the behavior of MR-FREIs under pure compression is offered in Van Engelen et al. [28].

Figures 5.15 and 5.16 show the contours of  $S_{11}$  in the center elastomer layers in the same isolators at  $u/t_r = 1.00$  and  $u/t_r = 1.75$ , respectively. The figures demonstrate that introducing an interior modification results in a reduction in the peak  $S_{11}$  values in the center elastomer layer. On the other hand, in isolators modified with exterior modifications, the peak absolute  $S_{11}$  increases. At  $u/t_r = 1.00$ , for example, the peak absolute value of  $S_{11}$  at mid-height of the center elastomer layer in the unmodified isolator is 2.12, while in isolators 58I and 58E the peak absolute values are 1.98 and 2.58, respectively. FEA results show that in isolators modified with interior modification, the location of the peak values of  $S_{11}$  changes as the lateral displacement increases. In isolator 58I under pure compression (Fig. 5.14), for example, the peak  $S_{11}$  values are observed to occur at the sides of the interior modification along the  $x$  axis. As the lateral displacement is increased, the locations of the peak  $S_{11}$  gradually shift, and at  $u/t_r = 1.75$  (Fig. 5.16), they are observed to occur above and below the modification along the  $y$  axis.

Figure 5.17 compares the distribution of  $S_{11}$ ,  $S_{22}$  and  $S_{33}$  at the mid-height of middle elastomer layer along  $x = 0$  and  $y = 0$  in the unmodified isolator and isolators 58I and 58E. Under pure compression, the distribution and the values of  $S_{11}$  and  $S_{22}$  in these three isolators are similar to each other. In the unmodified isolator at  $u/t_r = 1.00$  and  $u/t_r = 1.75$ , the values and distribution of  $S_{11}$  and  $S_{22}$  are similar, which is in agreement with the findings of Osgooei et al. [23] for square FREIs loaded in different directions. In isolators 58I and 58E, as the lateral displacement increases, the values of  $S_{11}$  slightly deviate from those of  $S_{22}$ . As expected, in the unmodified isolator, the peak values of  $S_{11}$

( $S_{22}$ ) and  $S_{33}$  in the center elastomer layer are observed at the center of the isolator ( $x = y = 0$ ). In isolator 58E under pure compression, the peak stress values are observed along  $y = 0$  with two peaks. As the lateral displacement of the isolator increases, the peak stress values increase and the distribution of the stresses changes, and at  $u/t_r = 1.75$  the peak values of  $S_{11}$ ,  $S_{22}$  and  $S_{33}$  are observed at the center of the isolator ( $x = y = 0$ ). In isolator 58I under pure compression, two peaks are observed along  $y = 0$ , while the peak stress values along  $x = 0$  are considerably lower. As discussed in [28], this implies that the response of the isolator is approaching the response of two individual isolators located at the left and right side of the interior modification. However, at  $u/t_r = 1.75$ , two stress peaks are observed along  $x = 0$ . This suggests that unlike in the pure compression case, as the lateral displacement increases, the contribution of the portions of the isolator located at the top and bottom of the interior modification in the lateral stiffness of the isolator becomes greater than the contribution of the portions located at the left and right side of the modification.

Figure 5.18 shows the contours of shear strain  $\gamma_{13}$  in the unmodified isolator and modified isolators 58I and 58E under different displacement amplitudes. For a better representation, the isolators are cut along the plane  $y = 0$  and both parts are shown. Under pure compression, the peak  $\gamma_{13}$  in the unmodified isolator is observed at the edge of the isolator  $x = \pm b$  along  $y = 0$ , with a value of 0.48. FEA results show that the peak  $\gamma_{13}$  values in the elastomer layers increase when a modification is introduced. In isolators 12E, 35E (not shown in Figure 18), and 58E, the peak shear strain values are 0.49, 0.59 and 0.79, respectively. In isolators with an interior modification, further increase in peak

$\gamma_{13}$  values is observed, with  $\gamma_{13} = 0.72, 0.87$  and  $1.02$  for isolators 12I, 35I and 58I, respectively. As expected, additional shear strains are induced in the elastomer layers as the isolators undergo lateral displacement. However, the rate of the increase in the peak shear strain values decreases as the lateral displacement increases. Similar to the pure compression case, introducing modifications results in an increase in the peak  $\gamma_{13}$  values. At  $u/t_r = 1.75$ , the peak  $\gamma_{13}$  value in the unmodified isolator is 1.34, which is increased to 1.57 and 1.77 in isolators 58I and 58E, respectively. The figures indicate that in the vicinity of the modification, large negative shear strains develop as a result of large localized deformation of the elastomer layers at those locations.

### 5.4.3 Deformed Shapes

The deformed shapes of the unmodified isolator and modified isolators 58I and 58E can be seen in Fig. 5.18. FEA results show that introducing a modification accelerates the full rollover in the isolators, which can be attributed to the reduction in the vertical stiffness of the modified isolators. In the unmodified isolator at  $u/t_r = 1.75$ , the originally vertical face of two interior elastomer layer (out of five total interior layers) are in contact with the supports, while in isolators 58E and 58I, the number of the interior elastomer layers in contact with the loading supports increase to four, suggesting that the full rollover occurs at a lower lateral displacement. This explains the variation in the lateral displacement amplitude at which stiffening in the lateral load-displacement is observed for different isolators (Figs 5.10 and 5.11).

#### 5.4.4 Stress in Fiber Reinforcement

Figure 5.19 compares the distribution of  $S_{11}$  in the center fiber reinforcement layer along  $y = 0$  and  $x = 0$  in the isolators with interior modifications. Under pure compression, the peak  $S_{11}$  in the unmodified isolator has a value of 3.99, which increases to 4.00 in isolator 12I and 4.89 in isolator 58I. FEA results show that as the lateral displacement of the isolators increases, large stresses develop in the vicinity of the modification along  $x = 0$ . Figure 5.20 compares the distribution of  $S_{11}$  in the center fiber reinforcement layer in the isolators modified with exterior modifications. Under pure compression, the peak tensile  $S_{11}$  increases along  $y = 0$  as the modification diameter increases. As the lateral displacement increases and similar to the isolators modified with interior modification, large tensile stresses develop in the vicinity of the exterior modification along  $x = 0$ . FEA results show a similar stress concentration in the vicinity of the modification for  $S_{22}$  in the fiber reinforcement layers and along  $y = 0$ . Figures 5.19 and 5.20 show that under lateral displacement, the peak  $S_{11}$  values in FREIs with interior modifications are significantly larger than in FREIs with exterior modifications.

#### 5.5 Conclusions

One of the most appealing aspects of a FREI is that it can be designed as a rectangular strip and placed underneath concrete or masonry walls, forgoing the requirement for costly wall beams used in conventional seismic isolation designs. The main disadvantage of the rectangular FREI is that the total plan area necessary to support the walls in the structure may be large, resulting in a horizontally stiff, and thus less

effective, isolation system. To ameliorate this potential shortcoming, the effective stiffness of the isolation system can be reduced by decreasing the shear area of the isolators through the introduction of modifications.

In this study, the lateral behavior of modified rectangular FREIs (MR-FREIs) was investigated. Experimental results of lateral test on five specimens were presented and used to evaluate three dimensional FE models. The FE models were subsequently used to investigate the influence of a wide range of modification configurations on the lateral response of FREIs. From the experimental and finite element analyses carried out, the following conclusions are drawn.

All the modified isolators exhibited the softening and subsequent stiffening behavior associated with unbonded FREIs. Introducing modifications resulted in a reduction in the effective lateral stiffness of the isolators and general improvement in the damping characteristics. Despite having the same area removed from isolators with interior and exterior modifications, the amount of reduction in the effective lateral stiffness was greater in isolators with interior modification. For both modification configurations, the amount of decrease in the effective stiffness was larger than what can be attributed to the plan area removed by the modification alone.

Comparing the lateral load-displacement relationships of the isolators showed that in modified isolators full rollover occurs at lower lateral displacements than in unmodified isolators. As the modification diameter increases, the lateral displacement at which full rollover occurs decreases. Consequently, the stiffening in the lateral load-displacement behavior is observed at lower lateral displacement in the modified isolators.

Comparing the stress values in the center elastomeric layers in the isolators showed that an exterior modification results in an increase in the peak absolute  $\sigma_{11}$ ,  $\sigma_{22}$  and  $\sigma_{33}$  values, while an interior modification results in decreased peak absolute stress values.

Modifying isolators results in an increase in the peak shear strain values in the elastomer layers. The increase is greater in isolators with interior modifications. In addition, large concentrated shear strain values are observed in the vicinity of the modification.

Introducing a modification (even with a small diameter) results in a large increase in the peak  $\sigma_{11}$  stress in the center fiber reinforcement layer. FEA results show a stress concentration of  $\sigma_{11}$  stress in the center fiber reinforcement layers in the vicinity of the modification. The peak stress values are higher in isolators with interior modifications.

The effect of introducing modifications to unbonded FREIs in an effort to reduce their effective lateral stiffness has been investigated in this study. These modifications can provide designers additional parameters to optimize their seismic isolation designs with unbonded FREIs.

## 5.6 Acknowledgments

This research was carried out as part of the mandate of the Centre for Effective Design of Structures (CEDs) at McMaster University and is partially funded by the Ontario Ministry of Economic Development and Innovation, Natural Sciences and Engineering Research Council of Canada (NSERC) and Early Researcher Awards (ERA). The authors also acknowledge MSC Software Corporation for their support.

## **5.7 References**

- [1] Kelly JM. Analysis of fiber-reinforced elastomeric isolators, *Journal of Seismology and Earthquake Engineering* 1999;2(1):19-34.
- [2] Kelly JM. Seismic isolation systems for developing countries, *Earthquake Spectra* 2002; 18(3):385-406.
- [3] Russo G, Pauletta M, Cortesia A. A study on experimental shear behaviour of fiber-reinforced elastomeric isolators with various fiber layouts, elastomers and aging conditions. *Engineering Structures* 2013;52:422-433.
- [4] Tsai HC, Kelly JM. Stiffness analysis of fiber-reinforced rectangular isolators, *Journal of Engineering Mechanics* 2002;128(4):462-470.
- [5] Kelly JM, Konstantinidis D. Low-cost seismic isolators for housing in highly-seismic developing countries. ASSISi 10th World Conference on Seismic Isolation, Energy Dissipation and Active Vibrations Control of Structures, Istanbul, 28-31 May 2007.
- [6] Das A, Dutta A, Deb SK. Modeling of fiber-reinforced elastomeric base isolators. *Proceeding of the 15<sup>th</sup> world conference on earthquake engineering*, Lisbon, Portugal 2012.
- [7] Peng T, Wang Z, Yu X. Influence of dimension parameters on the compression performance of FRP rubber bearings. *Advanced Materials Research* 2011; 255-260: 977-981.

- [8] Moon BY, Kang GJ, Kang BS, Kelly JM. Design and manufacturing of fiber-reinforced elastomeric isolator for seismic isolation, *Journal of Materials Processing Technology* 2002;130-131: 145-150.
- [9] Toopchi-Nezhad H, Tait MJ, Drysdale RG. Testing and modeling of square carbon fiber-reinforced elastomeric seismic isolators, *Structural Control and Health Monitoring* 2007;15(6):876-900.
- [10] Toopchi-Nezhad H, Tait MJ, Drysdale RG. Lateral response evaluation of fiber-reinforced neoprene seismic isolators utilized in an unbonded application, *Journal of Structural Engineering* 2008;134(10):1627-1637.
- [11] Russo G, Pauletta M, Cortesia A, Dal Binanco A. Experimental behavior of carbon fiber reinforced isolators. In: *Proc. 2008 Seismic Engineering International Conference Commemorating the 1908 Messina and Reggio Calabria Earthquake*, Reggio Calabria, Italy, 2008.
- [12] Kelly JM, Takhirov SM. Analytical and experimental study of fiber-reinforced elastomeric isolators. PEER Report 2001/11, Pacific Earthquake Engineering Research Center, University of California, Berkeley, 2001.
- [13] Kelly JM, Takhirov SM. Analytical and experimental study of fiber-reinforced strip isolators. PEER Report 2002/11, Pacific Earthquake Engineering Research Center, University of California, Berkeley, 2002.
- [14] Toopchi-Nezhad H, Tait MJ, Drysdale RG. Bonded versus unbonded strip fiber reinforced elastomeric isolators: finite element analysis, *Composite Structures* 2011;93(2):850-859.

- [15] Russo G, Pauletta M. Sliding instability of fiber-reinforced elastomeric isolators in unbonded applications. *Engineering Structures* 2013; 48:70-80.
- [16] Toopchi-Nezhad H, Tait MJ, Drysdale RG. Shake table study on an ordinary low-rise building seismically isolated with SU-FREIs (stable unbonded-fiber reinforced elastomeric isolators). *Earthquake Engineering and Structural Dynamics* 2009;38(11):1335-1357.
- [17] Naeim F, Kelly JM. *Design of Seismic Isolated Structures*. Wiley: New York, 1999.
- [18] Van Engelen NC, Tait MJ, Konstantinidis D. Horizontal behaviour of stable unbonded fiber reinforced elastomeric isolators (SU-FREI) with holes, 15<sup>th</sup> World Conference on Earthquake Engineering (15WCEE), Lisbon, 24-28 September 2012.
- [19] Kelly JM, Konstantinidis D. *Mechanics of rubber bearings for seismic and vibration isolation*. Wiley, Chichester, UK. 2011.
- [20] Konstantinidis D, Kelly JM, Makris N. Experimental investigations on the seismic response of bridge bearings. Report No. EERC-2008/02, Earthquake Engineering Research Center, University of California, Berkeley, 2008.
- [21] Peng TB, Zhang H, Li JZ, Li WX. Pilot study on the horizontal shear behavior of FRP rubber isolators. *Journal of Vibration and Shock* 2009;28:127-130. [in Chinese]
- [22] Osgooei PM, Tait MJ, Konstantinidis D. Three-dimensional finite element analysis of square fiber-reinforced elastomeric isolators (FREIs) under lateral loads. CSCE 2013 Annual Conference, Montréal, May 29 to June 1, 2013.

- [23] Osgooei PM, Tait MJ, Konstantinidis D. Finite element analysis of unbonded square fiber-reinforced elastomeric isolators (FREIs) under lateral loading in different directions. *Composite Structures*, 2014; 113:164-173.
- [24] Kelly JM, Marsico MR. Stability and post-buckling behavior in nonbolted elastomeric isolators. *Seismic Isolation and Protection Systems* 2010;1(1):41-54.
- [25] Kelly JM, Calabrese A. Mechanics of fiber reinforced bearings. PEER Report 2012/101, Pacific Earthquake Engineering Research Center, University of California, Berkeley, 2012.
- [26] Mordini A, Strauss A. An innovative earthquake isolation system using fibre reinforced rubber bearings. *Engineering Structures* 2008;30(10):2739-2751.
- [27] Gerhaher U, Strauss A, Bergmeister K. Numerical modeling of elastomeric bearings in structural engineering, *Advances in Materials Sciences* 2011;11(3):51-63.
- [28] Van Engelen NC, Osgooei PM, Tait MJ, Konstantinidis D. Experimental and finite element study on the compression properties of modified rectangular fiber reinforced elastomeric isolators (MR-FREIs). *Engineering Structures* 2014; 74:52-64.
- [29] Foster, BAD. Base isolation using stable unbonded fibre reinforced elastomeric isolators (SU-FREI). *Open Access Dissertations and Theses* 2012. Paper 6691.
- [30] MSC Marc. Theory and user information, vol. A. Santa Ana: MSC Software Corporation; 2013.
- [31] James AG, Green A, Simpson GM. Strain energy functions of rubber. I. Characterization of gum vulcanizates. *Journal of Applied Polymer Science* 1975;19:2033-2058.

- [32] James AG, Green A. Strain energy functions of rubber. II. The characterization of filled vulcanizates. *Journal of Applied Polymer Science* 1975;19:2319-2330.
- [33] Truesdell C, Noll W. *The non-linear field theories of mechanics*. 3rd ed. Springer 2004.

Table 5.1. Specimen Geometric Characteristics

Specimen	$d/2b$	Area (mm <sup>2</sup> )	$S$		Area Removed (%)
			Inner	Outer	
C1	-	3952	4.9	9.7	-
C2-46I	0.46	3500	3.3	6.7	11.4
C3-35I	0.35	3698	3.7	7.5	6.4
C4-46E	0.46	3500	3.9	7.8	11.4
C5-35E	0.35	3698	4.2	8.4	6.4

Table 5.2. Material constants for the third-order hyperelastic model (in MPa)

$C_{10}$	$C_{01}$	$C_{11}$	$C_{20}$	$C_{30}$
$2.352 \times 10^{-1}$	$9.819 \times 10^{-3}$	$-1.550 \times 10^{-3}$	$-1.817 \times 10^{-2}$	$2.489 \times 10^{-3}$

Table 5.3. MR-FREI geometric characteristics

Isolator	$d/2b$	Area (mm <sup>2</sup> )	$S$		Area Removed (%)
			Inner	Outer	
Unmodified	-	3952	4.9	9.7	-
12I	0.12	3924	4.5	9.0	0.7
12E	0.12	3924	4.7	9.4	0.7
23I	0.23	3839	4.1	8.2	2.9
23E	0.23	3839	4.5	9.0	2.9
35I	0.35	3698	3.7	7.5	6.4
35E	0.35	3698	4.2	8.4	6.4
46I	0.46	3500	3.3	6.7	11.4
46E	0.46	3500	3.9	7.8	11.4
58I	0.58	3245	2.9	5.8	17.9
58E	0.58	3245	3.5	7.0	17.9

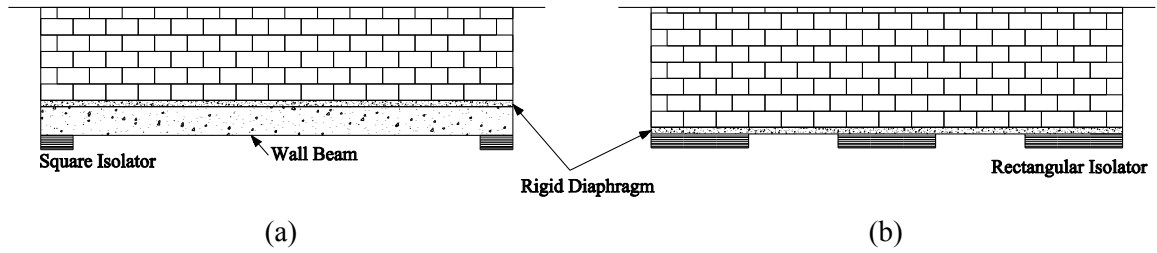


Figure 5.1. Isolation system under a masonry wall using (a) square isolators and (b) rectangular (strip) isolators

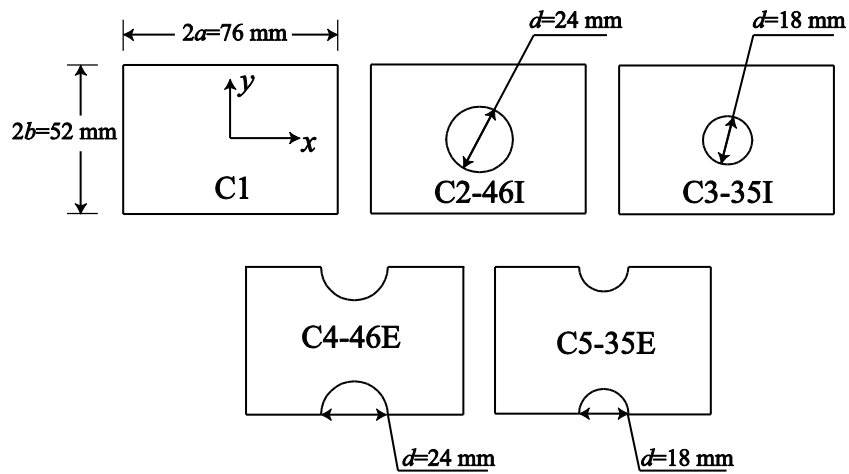


Figure 5.2. Plan view of the specimens

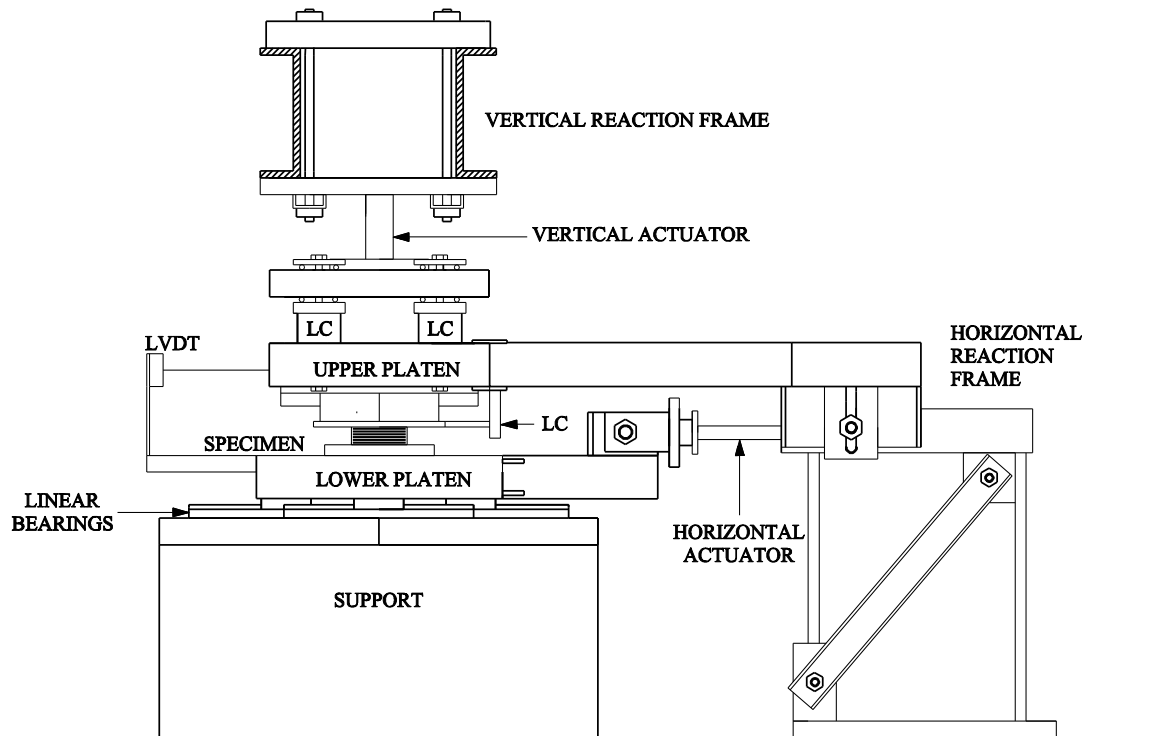


Figure 5.3. Schematic of the test apparatus.

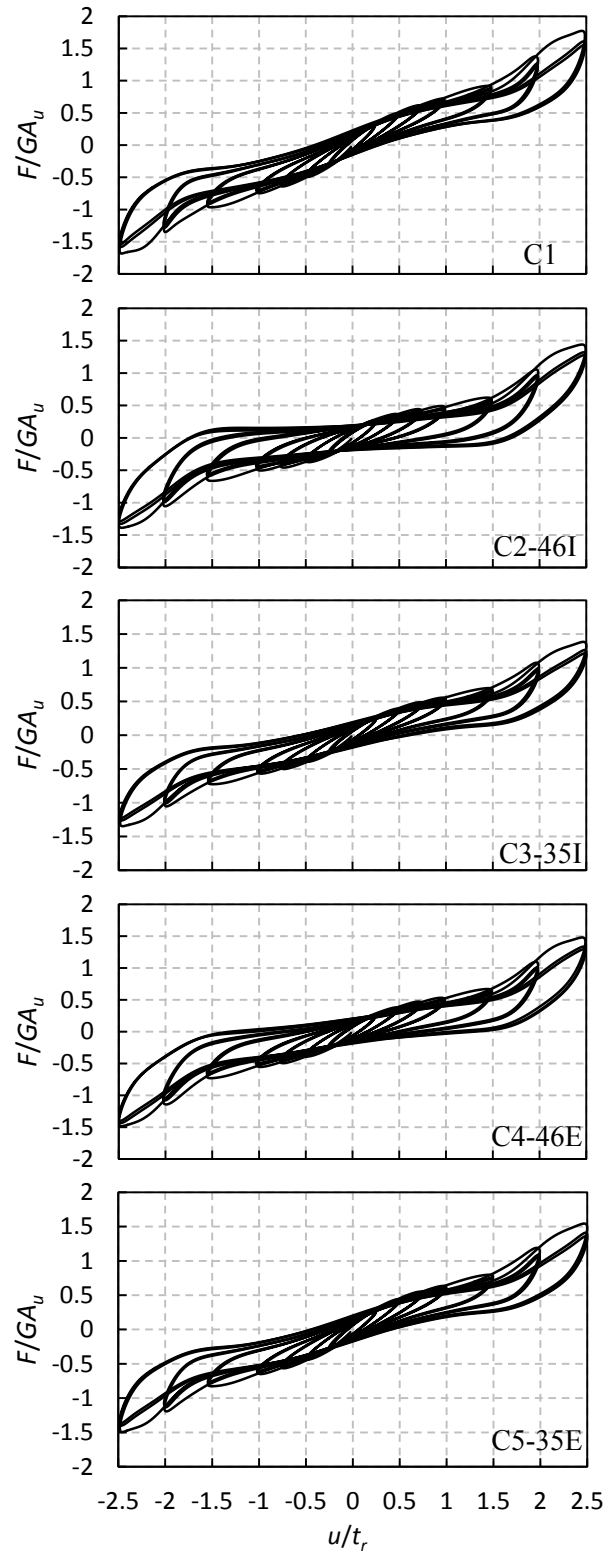


Figure 5.4. Experimental hysteresis loops for the isolators

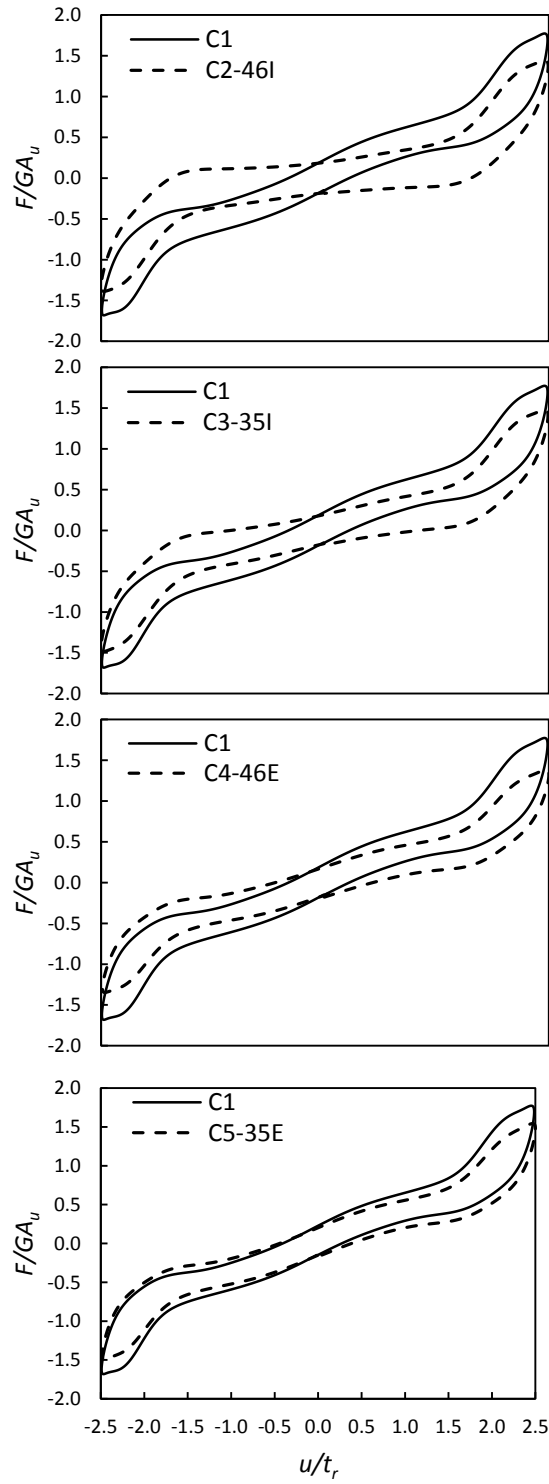


Figure 5.5. Comparison of the first cycle at  $u/t_r = 2.50$  from specimen C1 and respective modified specimens

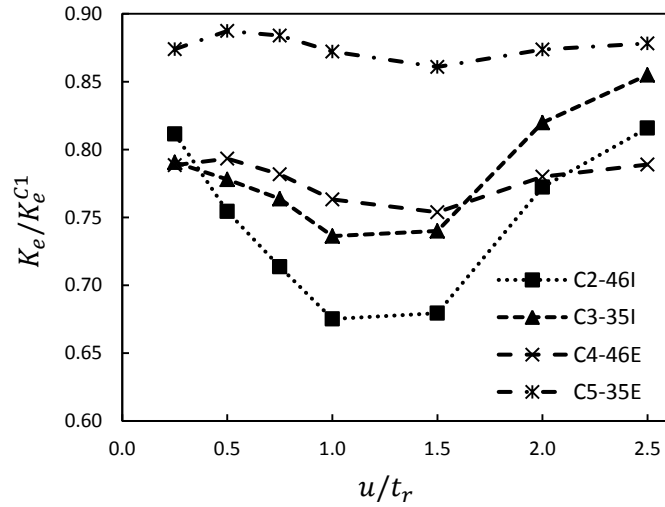


Figure 5.6. First cycle effective stiffness of the modified specimens normalized by the effective stiffness of the control specimen (C1)

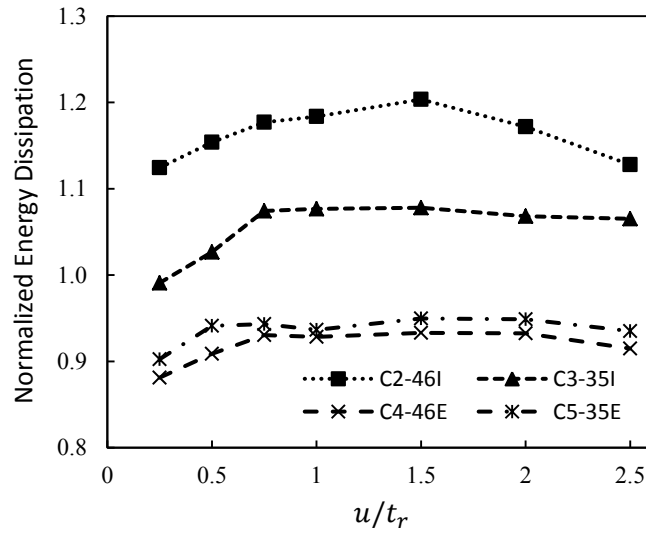


Figure 5.7. First cycle energy dissipation of the modified specimens normalized by the energy dissipation of the control specimen (C1)

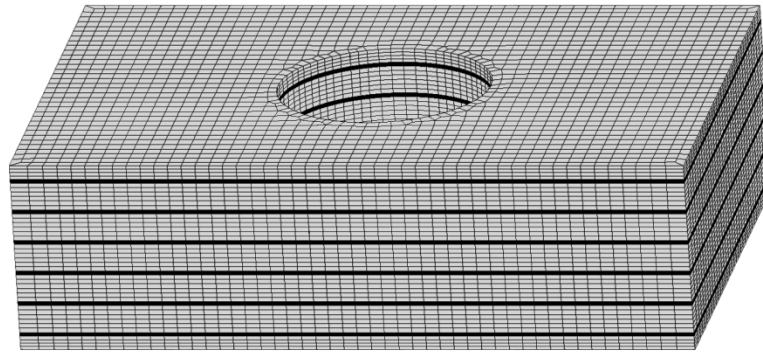


Figure 5.8. FE model of isolator C2-46I

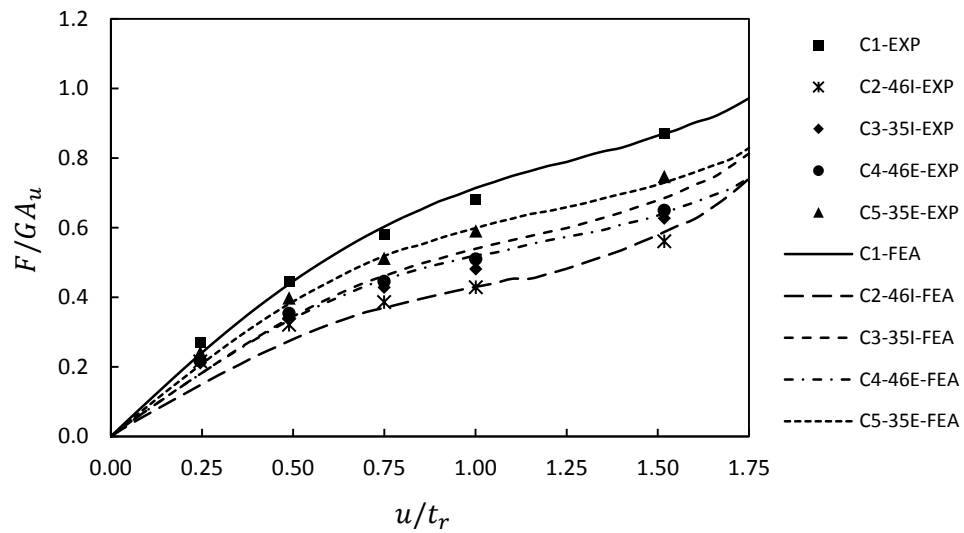


Figure 5.9. Comparison of the lateral load-displacement relationships of isolators obtained from FEA with experimental test results

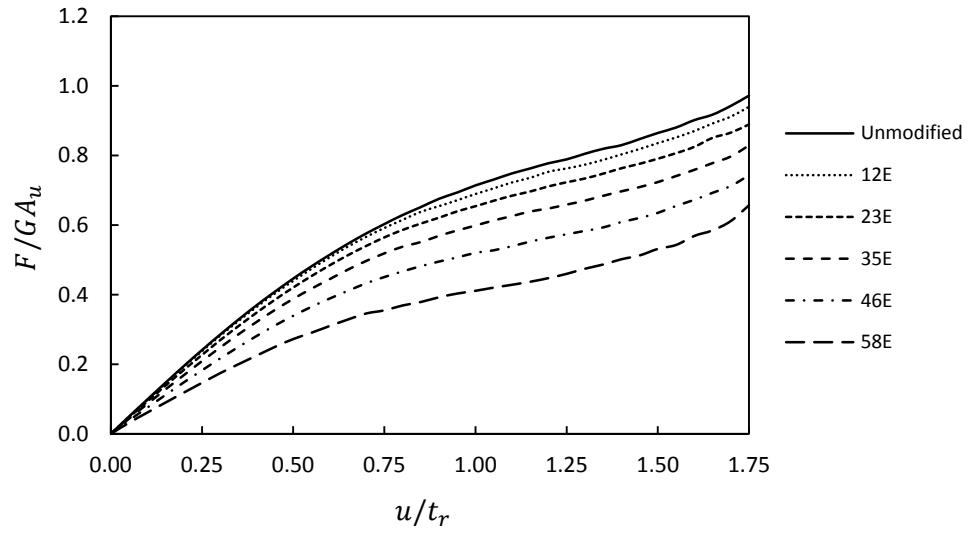


Figure 5.10. Lateral load-displacement relationships of isolators with exterior modification

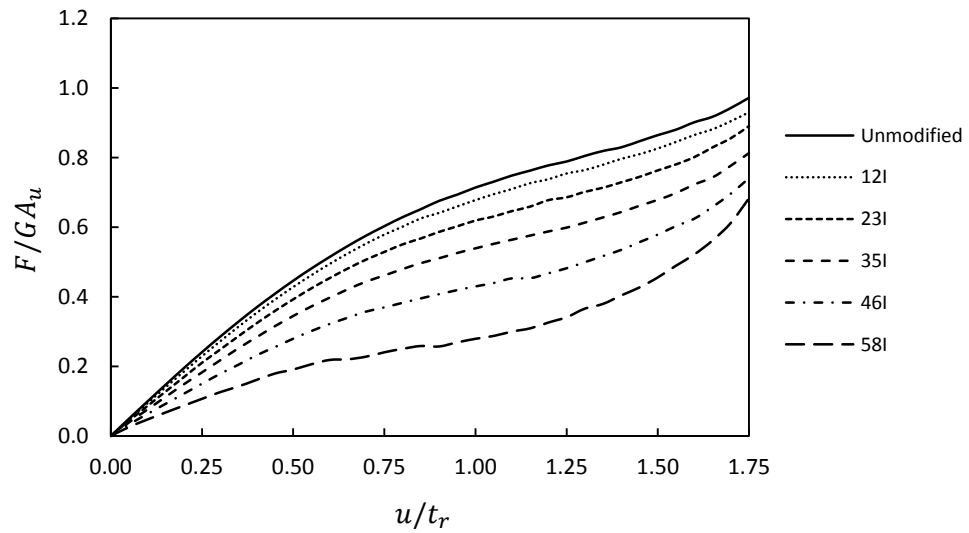


Figure 5.11. Lateral load-displacement relationships of isolators with interior modification

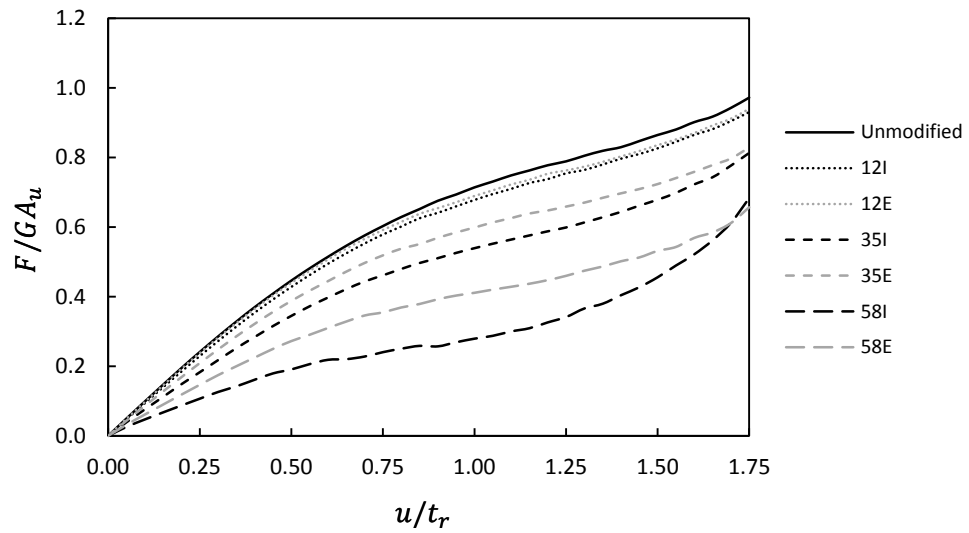


Figure 5.12. Lateral load-displacement relationships of selected isolators with modifications

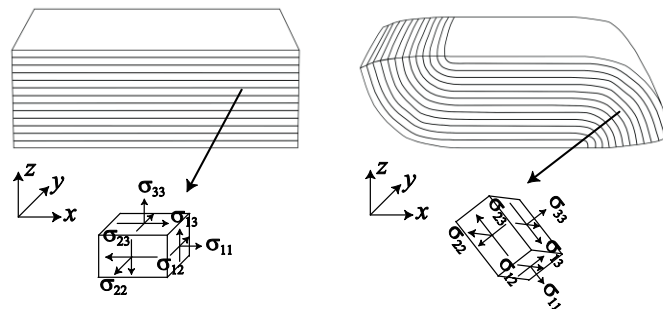


Figure 5.13. Local stresses in the undeformed (left) and deformed configuration (right)

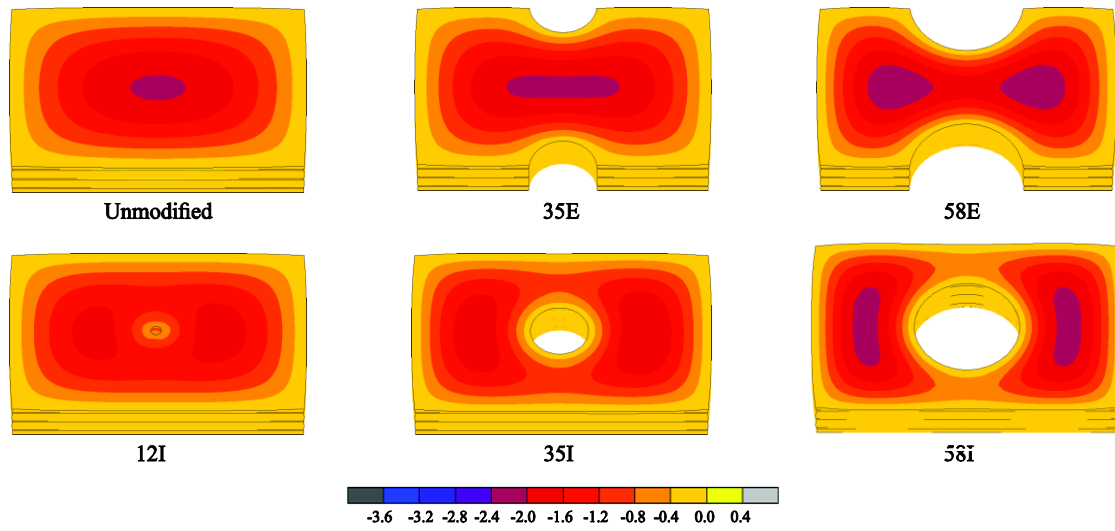


Figure 5.14. Contours of  $S_{11}$  in the center elastomer layer under pure compression

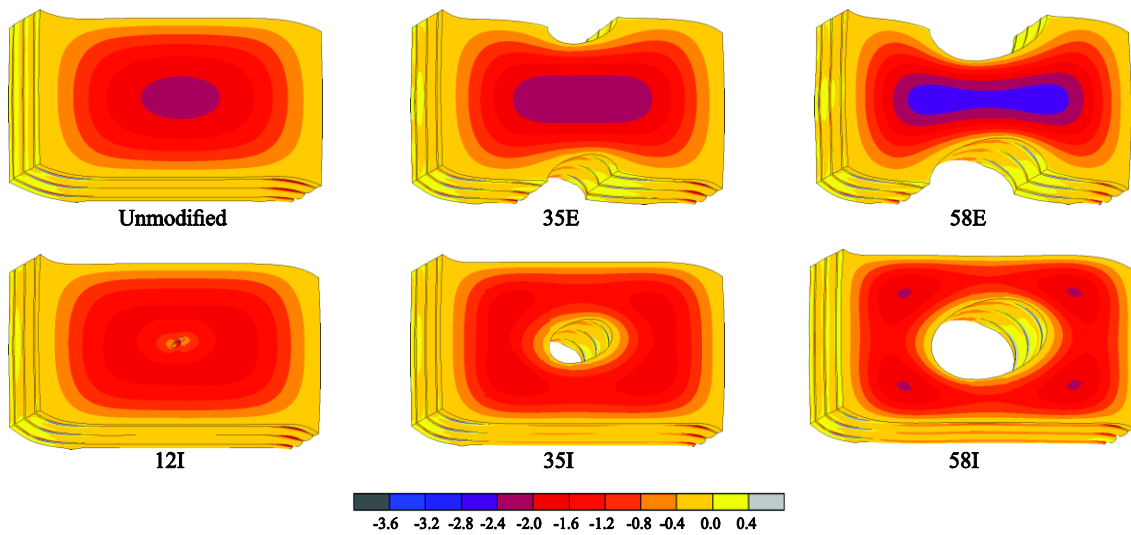


Figure 5.15. Contours of  $S_{11}$  in the center elastomer layer at  $u/t_r = 1.00$

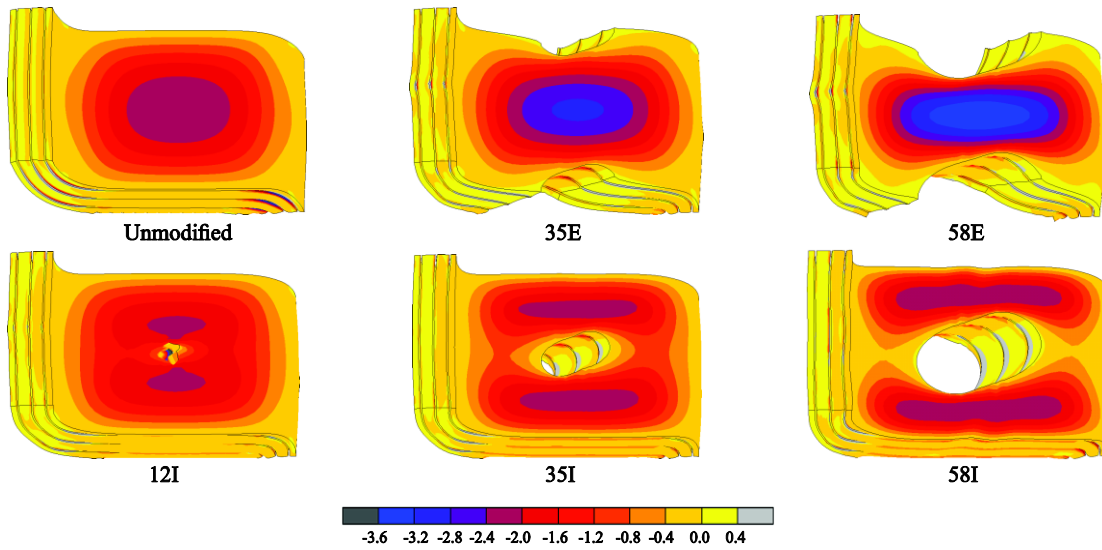


Figure 5.16. Contours of  $S_{11}$  in the center elastomer layer at  $u/t_r = 1.75$

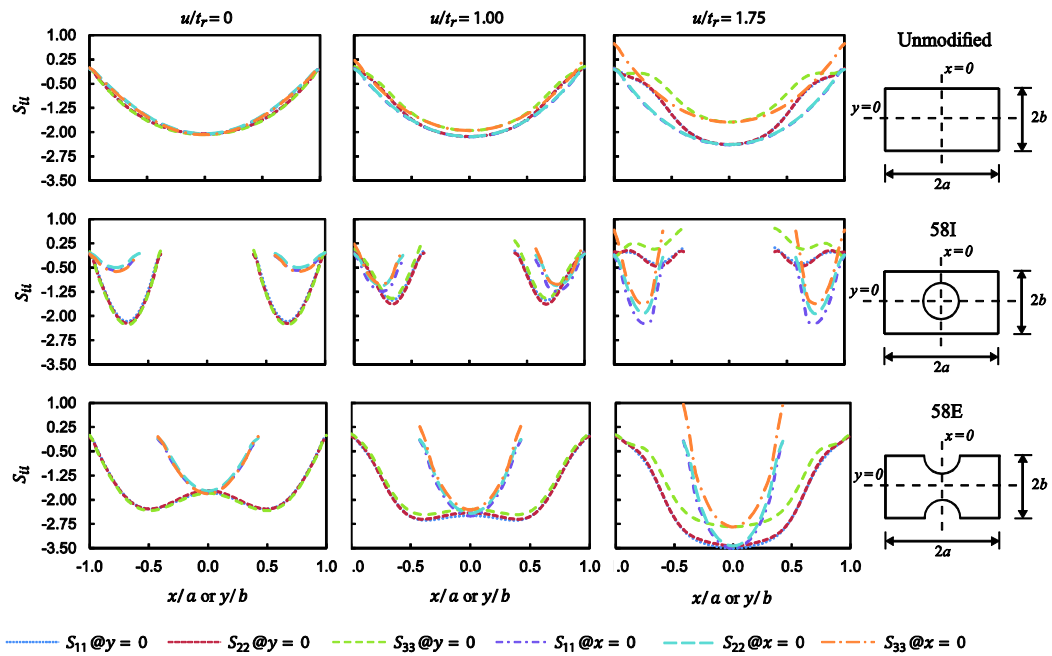


Figure 5.17. Variation of normalized stress profiles in the center elastomer layer along  $x = 0$  and  $y = 0$  in the unmodified isolator and isolators 58I and 58E

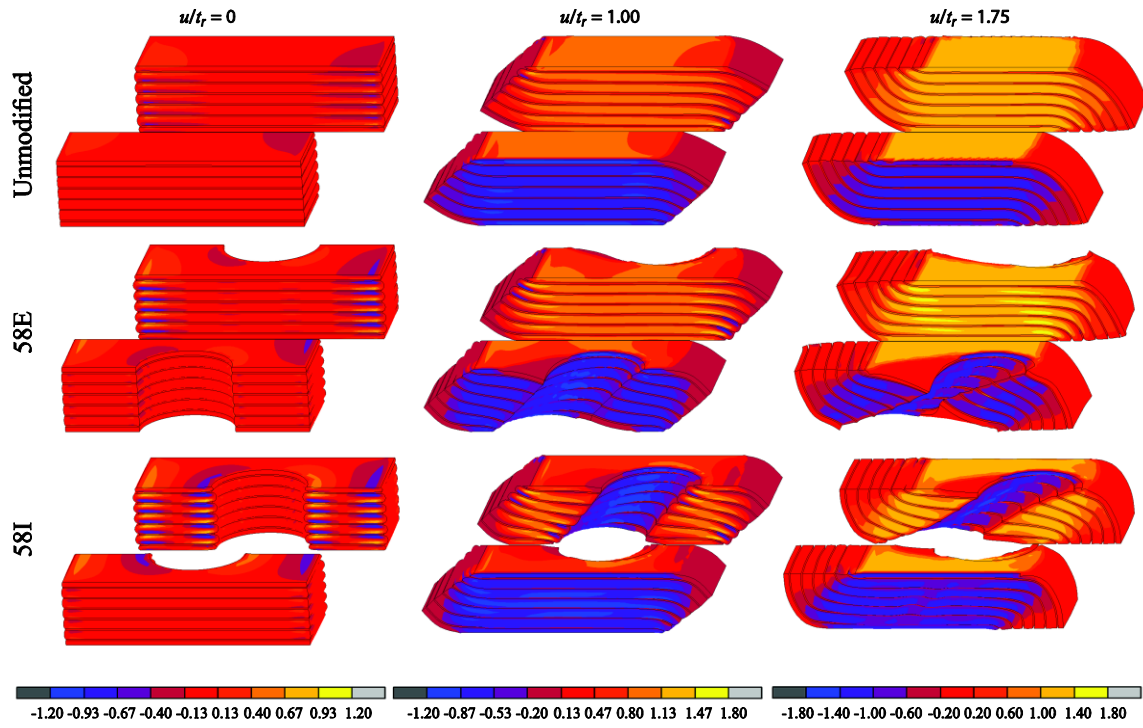


Figure 5.18. Contours of shear strain  $\gamma_{13}$  under pure compressions,  $u/t_r = 1.00$  and  $1.75$

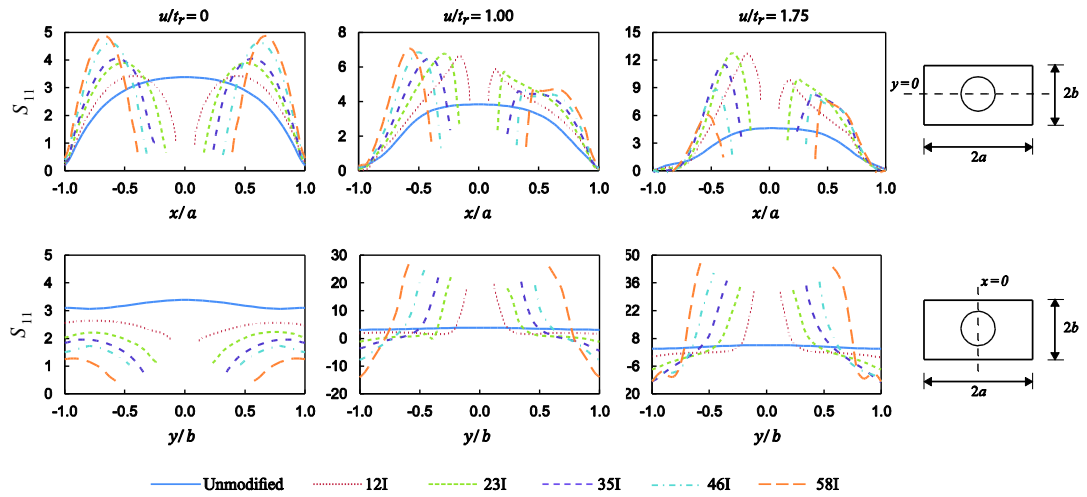


Figure 5.19. Distribution of  $S_{11}$  in the center fiber reinforcement layer in isolators modified with interior modifications along  $y = 0$  (top) and  $x = 0$  (bottom)

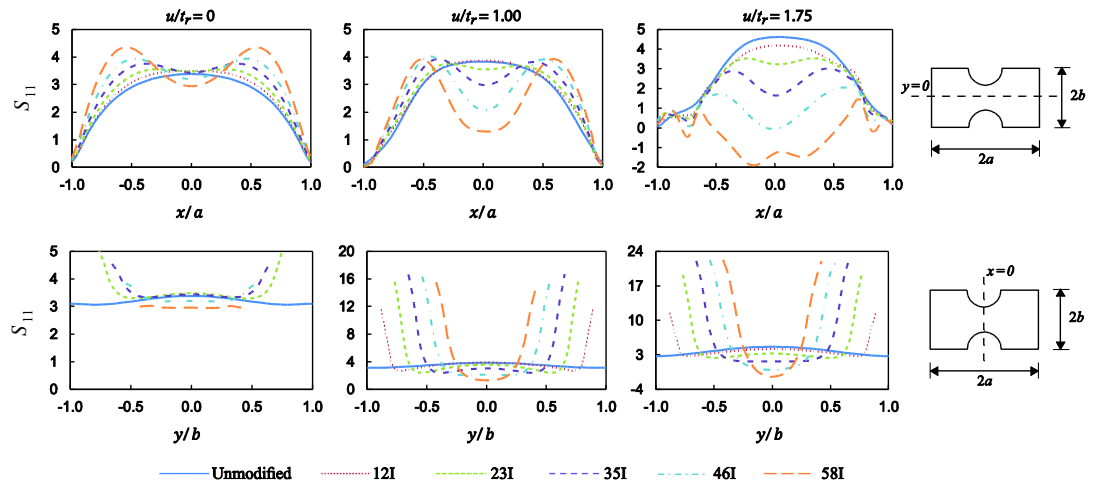


Figure 5.20. Distribution of  $S_{11}$  in the center fiber reinforcement layer in isolators modified with exterior modifications along  $y = 0$  (top) and  $x = 0$  (bottom)

## **Chapter 6: Seismic Isolation of a Shear Wall Structure using Rectangular Fiber-reinforced Elastomeric Isolators (FREIs)**

### **Abstract**

In this paper, the seismic response of a two-story reinforced concrete shear wall structure seismically isolated using unbonded rectangular fiber-reinforced elastomeric isolators (FREIs) is investigated. Employing isolators in the shape of long rectangular rather than the conventional square or circular shapes for buildings with masonry or reinforced concrete structural walls allows a more uniform distribution of the gravity loads and eliminates the requirement of additional wall beam elements. Time history analyses are conducted under fixed-base (FB) and base-isolated (BI) configurations using ten earthquake ground motions, selected to match the design response spectrum. The properties of the isolators are taken from lateral cyclic test results carried out on scale model FREIs. The Pivot-Elastic model is used to model the lateral response of isolators in the time history analyses. The peak response values of the BI structure are significantly reduced compared with the results for the FB structure. It is concluded that unbonded rectangular FREIs can be effectively designed and used to seismically isolate masonry or reinforced concrete shear wall structures.

### **6.1 Introduction**

Seismic isolation aims to mitigate the seismic demand on a structure by shifting the natural period of vibration of the isolated structure beyond the high energy period range

of earthquake ground motions. The isolator device needs to be flexible in the lateral direction while simultaneously being able to carry a large vertical load. The near incompressibility and low elastic modulus inherent in elastomers have made elastomeric isolators the most common type of seismic isolator in use. However, high manufacturing and installation costs associated with heavy conventional steel-reinforced elastomeric isolators (SREIs) have limited their application in North America to high importance or historical buildings. It is expected that reducing the cost and weight of elastomeric isolators will extend their usage to smaller structures and typical residential buildings [1].

Fiber-reinforced elastomeric isolators (FREIs) have been shown to be viable and potentially inexpensive seismic isolator devices [2, 3]. FREIs utilize fiber material for the reinforcing layers, which reduces both the weight and the manufacturing costs compared to SREIs. FREIs can be installed in an unbonded application where isolators are placed between the superstructure and the foundation with no bonding or fastening. Unbonded FREIs undergo a unique rollover deformation when subjected to lateral loading. Osgooei et al. [4] showed that compared with the bonded application, unbonded FREIs are more efficient in mitigating the seismic demand on the structures. Toopchi-Nezhad et al. [5] showed that the stress demand on both rubber and fiber reinforcement layers are reduced when an unbonded application is employed.

In seismic isolation projects, it is common practice to use rigid diaphragms just above and just below the isolation interface, and to install one isolator underneath each column between the two rigid diaphragms. For seismically isolating buildings with reinforced concrete or masonry structural walls, additional wall beams are needed to span

between isolators to support the superstructure. These additional beam elements increase construction costs. It has been proposed that using long rectangular isolators for isolating buildings with structural walls could result in a more cost-effective isolation system, as they provide a more uniform support condition along the walls [1, 6]. Thus, the size and the reinforcements of the wall beams could be reduced, or even eliminated altogether. Currently, nearly all isolators are manufactured in a circular or square shape. One of the benefits of FREIs is the ability of manufacturing large rectangular pads from which individual isolators can be cut to the required shape and size.

In this paper, the seismic response of a two-story reinforced concrete shear wall structure is investigated. Numerical analyses are carried out on both the fixed-base (FB) and base-isolated (BI) structure in order to determine the efficiency of the isolation system. The seismic isolation system is composed of 48 rectangular FREIs, with three FREIs installed underneath each shear wall. Results of lateral cyclic tests conducted on 1/4 scale rectangular FREIs are used to model the behavior of the isolators. The Pivot-Elastic model proposed by Osgooei et al. [4] is used to model the lateral response of the FREIs. The nonlinear behavior of the shear walls is modeled using multi-layer nonlinear shell elements with smeared reinforcement. A set of ten earthquake ground motions are considered, scaled at three hazard levels: service level earthquake (SLE), design base earthquake (DBE) and maximum considered earthquake (MCE). Time history analyses are carried out using SAP2000 [7]. Results from the time history analyses show a significant reduction in the peak response values of the BI structure using the proposed seismic isolation system. It is concluded that long rectangular shape FREIs could be

effectively used as a potential cost effective isolation system for reinforced concrete shear wall or masonry structures.

## **6.2 Rectangular Shape Isolators**

Figure 6.1-a shows a schematic view of a seismically isolated frame structure, where square shape isolators are placed underneath columns. Currently, circular or square isolators are the most common shapes in use, as an isotropic isolation system has traditionally been designed using individual isolators with symmetrical shapes [6]. Kelly [1,6] suggested that using long rectangular shape isolators could be beneficial for shear wall type structures. Figures 6.1-b and 6.1-c show the application of seismic isolation to a masonry structure, using square and rectangular shaped isolators, respectively. The long rectangular shape isolators provide a more uniform support for the walls and can potentially simplify the installation of seismic isolation in buildings with structural walls. Test results [8] and finite element analysis (FEA) [9] have shown that the aspect ratio (length along the loading direction to total height of the isolator) of unbonded FREIs plays an important role on their lateral response. Thus, different responses are expected from rectangular-shaped FREIs loaded along their length or their width. Kelly and Takhirov [10] observed that a FREI with a rectangular shape can be unstable when loaded along its width, while exhibiting stable lateral behavior along its length. In practice, since the rectangular shape isolators would be installed in directions perpendicular to each other, the global response of the isolation system (which is the combination of the responses of individual isolators along their length and their width)

must be considered for design and analysis. Thus, the isolation system, which is composed of rectangular FREIs, must exhibit a stable response, however individual isolators may have instability issues along their shorter direction.

Figure 6.2 shows schematic deformed shapes of a rectangular FREI along its longer (left) and shorter (right) directions. The length to width ratio of the isolator is defined as  $b/d = a$  ( $a \geq 1$ ). It can be shown that at each displacement amplitude of  $u$ , the roll over portion of the isolator loaded along its width ( $2A_r b$ ) is  $a$  times the roll over portion when the isolator is loaded along its length ( $2A_r d$ ), which explains the lower effective stiffness values obtained from rectangular FREIs loaded along their shorter direction. With the assumption that the roll over portion of the FREIs is stress-free, the effective stiffness of two perpendicular rectangular isolators shown in Fig. 6.2 at a lateral displacement of  $u$  loaded along their principal axes can be calculated

$$K_h = \frac{G}{t_r} [2A - ud(1 + a)] \quad (6.1)$$

where  $G$  is the shear modulus of rubber,  $t_r$  is the total rubber thickness and  $A = bd$  is the total plan area of the isolator. It can be observed from Eq. 6.1 that for a rectangular FREI with constant values of  $G$ ,  $t_r$  and  $A$ , at any given displacement amplitude, the maximum value of the effective stiffness is obtained for  $a = 1$ . In other words, the effective stiffness of an isolation system composed of rectangular FREIs with the same height and plan areas placed perpendicular to each other is maximum with square shape isolators. Thus, another benefit of using long rectangular FREIs, compared to square shape isolators, is the additional reduction in the lateral stiffness of the isolation system.

### 6.3 Shear Wall Structure

A two story reinforced concrete shear wall structure is employed in this study. The plan and elevation views of the structure are shown in Fig. 6.3. The structure is symmetric in plan and is composed of sixteen 1500 mm long  $\times$  150 mm wide reinforced concrete shear walls. Perfectly rigid diaphragms are assumed to connect the shear walls at each story. The total height,  $h$ , of the structure is 6 m. All the shear walls have the same thickness and reinforcement detailing, shown in Fig 6.4. The reinforcement ratio of the walls in both vertical and horizontal directions is 1.4%. The gravity loads are assumed to be distributed equally between the shear walls. The structure is designed according to the provisions of NBCC [11] and CSA-A23 [12] for a site in Vancouver, Canada. For the BI structure, a perfectly rigid diaphragm is assumed to connect the walls at the base level. The total weight of the fixed-base ( $w_{FB}$ ) and the base isolated structures ( $w_{BI}$ ) were 4046 kN and 6070 kN, respectively.

### 6.4 Seismic Isolation System

The seismic isolation system is composed of 48 rectangular FREIs, with three isolators installed under each wall (Fig. 6.5). The rectangular FREIs have plan dimensions of 304 mm  $\times$  206 mm with total height ( $h$ ) and total rubber thickness ( $t_r$ ) of 89.4 mm and 76.2 mm, respectively. The aspect ratio of the isolator along its length and its width is 3.4 and 2.3, respectively. The isolators are placed under the shear wall so that their longer direction is parallel with the length of the wall, as shown in Fig. 6.5. The lateral behavior of the isolators is obtained from an experimental test program previously

carried out on FREIs [13]. During the experimental program, an average vertical stress of 2 MPa was applied to the isolators while they were subjected to sinusoidal cycles of lateral displacements of  $u/t_r = 0.25, 0.50, 0.75, 1.00, 1.50, 2.00$  and  $2.50$ . Figure 6.6 shows the unscragged hysteresis loops for the isolators along the  $x$  (Fig. 6.6-a) and  $y$  (Fig. 6.6-b) directions. In Fig. 6.6, the force is normalized with respect to  $GA$ , ( $G = 0.44$  MPa is the shear modulus of the rubber obtained at 100% shear deformation). As can be observed from Fig. 6.6, the effective stiffness of the isolator reduces at first as the lateral displacement increases. At larger displacement amplitudes ( $u/t_r = 2.00$  and  $2.50$ ), the originally vertical faces of the isolators contact the loading surface, denoted as full rollover, which results in an increase in the effective stiffness.

Table 6.1 shows the values of the normalized effective stiffness and effective damping ratio of the isolators along the  $x$  and  $y$  directions. Due to different values of aspect ratio of the isolator along the  $x$  and  $y$  directions, different responses are observed along the two directions. As discussed earlier and due to the increase in the roll over portion, a lower effective stiffness is obtained when the isolator is loaded along the direction with lower aspect ratio ( $y$  direction). Changing the loading direction from  $x$  to  $y$  results in an increase in the values of the damping ratio of the isolator. At  $u/t_r = 1.50$  for example, the equivalent damping ratio increases by 42% as the loading direction changes from  $x$  to  $y$ . Table 6.2 lists the normalized values of the energy dissipation  $E_h$  (area under the hysteresis loops) along the  $x$  and  $y$  directions. It can be observed that the energy dissipation reduces by changing the loading direction from  $x$  to  $y$ , with a maximum value of 11.6%. It can be concluded that the increase in the damping ratio of the isolator along the  $y$  direction is due to the reduction in the effective stiffness values of the isolators.

## 6.5 Modeling U-FREIs

The Pivot-Elastic model, proposed by Osgooei et al. [4] is employed to model the lateral behavior of the isolators. This model is composed of a bilinear model with Pivot hysteresis connected in parallel to a nonlinear spring (Fig 6.7). The Pivot-Elastic model is capable of predicting the variation of the effective stiffness and damping ratio of the isolators, while its simple form allows it to be implemented in commercial codes such as SAP2000 [7]. In addition, and in contrast to other available FREI models [14-16], the time history analysis using the Pivot-Elastic model does not require iteration. In this paper, a seventh order polynomial is adopted for the nonlinear spring. The force of the nonlinear spring  $F_{NE}$  at the displacement  $u$  is expressed as

$$F_{NE} = a_1u + a_2u^3 + a_3u^5 + a_4u^7 \quad (6.2)$$

where  $a_i$  are the polynomial parameters. The effective stiffness of the model can be calculated by [4]

$$K_{\text{eff}} = \begin{cases} K_1 + a_1 + a_2u^2 + a_3u^4 + a_4u^6 & u < u_y \\ (K_1 - K_2) \frac{u_y}{u} + K_2 + a_1 + a_2u^2 + a_3u^4 + a_4u^6 & u \geq u_y \end{cases} \quad (6.3)$$

where  $K_1$ ,  $K_2$  and  $u_y$  are the parameters of the bilinear pivot model, defined in Fig 6.7.

The effective damping of the model for  $u \geq u_y$  is given by [4]

$$\beta_{\text{eff}} = \frac{(3K_1u_y + K_2u - K_2u_y)(K_1 - K_2)(u - u_y)}{2\pi K_{\text{eff}}K_1u^2} \quad (6.4)$$

The model parameters are determined by minimizing the error between the values of the effective stiffness and damping ratio predicted by the model (Eqs. 6.3 and 6.4,

respectively) with those obtained from experimental test results (Table 6.1) at the displacement amplitudes considered in the tests. Table 6.3 lists the calculated values for the parameters of the Pivot-Elastic model for the isolator along the  $x$  and  $y$  directions. The ratio of the effective stiffness and damping ratio values predicted by the Pivot-Elastic model over the experimentally obtained values are listed in Table 6.4. Figure 6.8 compares the normalized hysteresis loops of the isolator predicted by the Pivot-Elastic model and the experimental test results. It can be observed from Fig 6.8 that the predicted response for the FREI is in good agreement with the experimental results.

### 6.6 Modeling Shear Wall Structure

The nonlinear behavior of the shear walls is modeled using multi-layer shell elements (Fig. 6.9). These elements can simulate the in-plane and out-of-plane bending, as well as the coupled in-plane bending-shear behavior of the shear walls. The element consists of a number of layers, each with different thickness and material properties. The reinforcement in the shear wall is smeared into layers along two perpendicular directions (Fig. 6.9). In this study, three layers are defined for the shear walls: the reinforcement steel layer at the center, covered by two concrete layers of equal thicknesses. The stress-strain relationship proposed by Popovics [17] is used for the concrete:

$$f_c = \frac{nf'_c \left( \frac{\varepsilon_c}{\varepsilon_{co}} \right)}{(n-1) + \left( \frac{\varepsilon_c}{\varepsilon_{co}} \right)^n} \quad (6.5)$$

where  $f_c$  is the compressive stress,  $f'_c$  is the nominal compressive strength,  $\varepsilon_c$  is the compressive strain,  $\varepsilon_{co}$  is the corresponding strain at  $f'_c$  and  $n$  is defined by [17] as

$$n = 5.8 \times 10^{-2} f'_c (\text{MPa}) + 1 \quad (6.6)$$

Assuming  $f'_c = 30$  MPa and  $\varepsilon_{co} = 0.002$ , the stress-strain relationship shown in Fig. 6.10 is obtained for the concrete. The tensile strength of the concrete is neglected in the analysis. The hysteresis behavior of the concrete is modeled using Takeda hysteresis model [18]. The grade of the reinforcement steel is assumed ST-420 with a kinematic hardening and an ultimate strength of  $F_u = 650$  MPa (Fig. 6.10).

### 6.7 Earthquake Ground Motions

Three earthquake hazard levels are considered for the time history analyses: Maximum Considered Earthquake (MCE), representing earthquakes with 2% probability of exceedance in 50 years (2475 year return period); Design Basis Earthquake (DBE), corresponding to earthquakes with 10% probability of exceedance in 50 years (475 year return period); and Service Level Earthquake (SLE) representing earthquakes with 50% probability of exceedance in 50 years (75 year return period). Considering a site in Vancouver, Canada with a soil type C, the NBCC [11] design response spectrum is obtained. Since in NBCC [11], the design spectrum is given for earthquakes with 2% probability of exceedance in 50 years, which corresponds to MCE hazard level according to the provisions of ASCE-7 [19], the calculated spectrum is multiplied by 2/3 to simulate a design response spectrum that matches the DBE hazard level. The standardized sets of ground motions provided by Baker et al. [20] (set #1A, broad-band ground motions with

a magnitude of  $M=7$  for a soil site) were used to select ten ground motions. One set of ten ground motions was randomly selected among a total of 80 different ground motions and for each set, the difference between the values of pseudo acceleration obtained from the mean response spectrum of the set with those of the design spectrum over two period ranges (0.26 s to 0.37 s for the FB and 1.25 s to 1.75 s for the BI structure) was calculated. The FB period range is obtained from finite element model of the structure and will be discussed later. The BI period range is calculated considering the total mass of the BI structure ( $w_{BI}/g$ ) and the minimum and maximum values of the effective stiffness of the isolation system. This procedure was repeated until the average error over the considered period ranges was found to be less than a pre-selected value. Table 6.5 lists properties of the selected ground motions. Figure 6.11 shows the 5% damped response spectra of the selected ground motions. In Fig. 6.12, the mean response spectrum is compared with the design spectrum. In the process of selecting the ground motions, actual recorded motions are selected to match with the DBE design spectrum without the application of any scaling factor. For MCE and SLE hazard levels, the amplitude of the selected ground motions was multiplied by 3/2 and 2/3, respectively, according to the provisions of ASCE-7 [19].

### **6.8 Time History Analyses**

The nonlinear time history analyses on the FB and BI structures under the selected set of ground motions at SLE, DBE and MCE hazard levels are carried out using SAP2000 [7]. The natural periods of vibration of the FB structure were calculated using

the finite element model created in SAP2000 [7]. Based on the provisions of CSA-A23 [12], the moment of inertia of the gross shear wall sections was reduced by 30% and 65% for the un-cracked and cracked sections, respectively. Figure 6.13 shows the first two modes with highest mass participation ratio (MPR) values along the direction of ground motion. The values of the periods for both un-cracked ( $T_{\text{uncr}}$ ) and cracked sections ( $T_{\text{cr}}$ ) are shown for each mode.

## 6.9 Results and Discussions

The mean values of the ratio of peak (absolute) floor acceleration (PFA) to peak ground acceleration (PGA) for the three earthquake hazard levels considered in the time history analyses are compared in Figure 6.14. As expected, for the FB structure, the peak floor accelerations are amplified with respect to the PGA. The mean values of the amplification factor for the roof level are 2.60, 2.48 and 2.06 for SLE, DBE and MCE levels, respectively. The reduction in amplification factor with increasing earthquake hazard level is due to the yielding that occurs in the superstructure. For the BI structure, PFA is reduced with respect to the PGA, and the mean values of the amplification factor for SLE, DBE and MCE level earthquakes are 0.65, 0.53 and 0.57, respectively.

Figures 6.15 and 6.16 compare the mean values of the story shear (normalized with respect to  $w_{FB}$ ) and overturning moment (normalized with respect to  $hw_{FB}$ ) for the FB and BI structures. Compared to the FB structure, a significant reduction in the mean peak response values is observed in the BI structure. Both for mean peak story shear and mean peak overturning moment, the highest reduction in the peak response values is obtained

for the DBE hazard level. For the mean peak superstructure base shear (story shear at the first floor) for example, the reduction in the BI structure compared to the FB structure is 67%, 73% and 66% for SLE, DBE and ME hazard levels, respectively.

Figure 6.17 compares the mean values of the peak inter-story drift ratio (IDR) for the FB and BI structures. It should be noted that the majority of the relative displacement between the first and second floors is due to the rotation of the shear walls at the base level, and thus the larger inter-story drift ratios observed in the second story compared to the values in the first story do not indicate larger demands on the walls. The reduction in the mean values of the inter-story drift ratio in the first story for the BI structure compared with the FB structure is 84%, 87% and 82% for SLE, DBE and MCE hazard levels, respectively. Analysis on the stresses in the multi-layer shell elements show that yielding of the reinforcements initiates at an inter-story drift ratio of 0.204% in the first story. According to the mean values of the peak inter-story drift ratio in the first story obtained for the BI structure for SLE, DBE and MCE hazard levels (0.024%, 0.035% and 0.084%, respectively), no yielding in the steel reinforcement is expected to occur. However, in one ground motion (FP-4) and at MCE level, yielding is observed in the BI structure. For the FB structure, yielding of steel reinforcement was observed for 2, 8 and 9 earthquake ground motions at the SLE, DBE and MCE hazard levels, respectively.

The mean floor acceleration spectra for the FB and BI structures calculated at 2% damping are shown in Figure 6.18. The floor spectrum is an important tool for assessing seismic demands on attached equipment. For the FB structure, prominent peaks in the floor spectra appear near the fundamental frequency of the structure. A slight leftward in

the frequency at which the spectral peak occurs is noted in going from the SLE spectra to the DBE spectra, indicating softening. Notable peaks also appear in the floor spectra of the FB structure at the second mode frequency. The floor spectra for the BI structure exhibit peaks at the fundamental frequency of the isolated structure just slightly below 1 Hz. Within the frequency range important for attached equipment, say  $1 \text{ Hz} < f < 100 \text{ Hz}$ , the floor spectral demands in the BI structure are, on average, substantially lower than in the FB structure.

Figure 6.19 shows the values of the peak isolation displacement for each ground motion. The mean values of the peak isolation displacement, which are shown with dashed lines in the figure, are  $u/t_r = 0.47$ ,  $0.78$  and  $1.29$  for SLE, DBE and MCE hazard levels, respectively. The mean values of the peak isolation displacement obtained at different hazard levels shows that the peak isolation displacement increases almost linearly with the ground motion amplitude, which is in agreement with the provisions of ASCE-7 [17] for calculation of maximum isolation displacement. The minimum and maximum values for the peak isolation displacement considering the three hazard levels considered in the time history analyses are obtained  $u/t_r = 0.17$  and  $u/t_r = 2.49$ , respectively.

Table 6.6 lists the values of the maximum, minimum, mean and standard deviation for the roof acceleration, total inter-story drift ratio (defined as the roof displacement divided by the total height of the structure) and the superstructure base shear for the three hazard levels. As can be observed from the values in the table, the maximum reduction in the mean peak response values in the BI structure is obtained at DBE hazard level. For

the BI structure, the values of the standard deviation of the peak response values for SLE and DBE hazard levels are close to each other. However, a large increase in the standard deviation is observed for the MCE hazard level, which implies larger nonlinearity in the superstructure at this hazard level.

## **6.10 Summary and Conclusions**

In this paper, time history analyses were carried out on a two-story reinforced concrete shear wall structure. The seismic response of the structure was investigated using ten earthquake ground motions selected to match the corresponding DBE level response spectrum of NBCC [11]. Three earthquake hazard levels of SLE, DBE and MCE were considered for the analyses. The seismic response of the structure in a base isolated configuration was investigated. The isolation system was composed of 48 rectangular FREIs, with three isolators installed under each wall in order to provide a uniform distribution of gravity loads.

The properties of the FREIs were taken from the lateral cyclic test results conducted on 1/4 scale model isolators. The lateral response of the rectangular isolators was modeled in the time history analyses using the Pivot-Elastic model. This model, proposed by Osgooei et al. [4], is able to predict variation in the effective stiffness and damping ratio of the FREIs and could be implemented in general purpose structural analysis programs. Analyses were carried out using SAP2000 [7]. The nonlinear response of shear walls was modeled using multi-layer shell elements which accounts for the nonlinear material behaviors.

In order to investigate the efficiency of the seismic isolation system, the mean of the peak response values of the FB and BI structures obtained from the time history analyses were compared with each other. In terms of the superstructure base shear, 67%, 74% and 66% reduction was obtained for SLE, DBE and MCE hazard levels, respectively. The reduction obtained for the mean peak total inter-story drift ratio was 86%, 88% and 81% for SLE, DBE and MCE hazard levels, respectively. Analyses results showed that the peak values of the accelerations in the BI structure were significantly reduced. The reduction in the values of the mean peak roof acceleration was 75%, 77% and 70% for SLE, DBE and MCE hazard levels, respectively. It was observed that the yielding in the steel reinforcement occurred only in one earthquake ground motion for the BI structure, whereas for the FB structure, yielding of steel reinforcement was observed for a total of 19 earthquake ground motions, considering all three hazard levels.

This study demonstrates that the seismic isolation of buildings with structural walls using rectangular FREIs is a viable option for reducing seismic demands on the structure and its contents. FREIs are low weight and potentially low cost isolator devices and are suitable for low-rise buildings. The isolation system composed of rectangular FREIs could potentially reduce the installation costs and extend the application of seismic isolation to ordinary and residential masonry structures.

## **6.10 Acknowledgments**

This research was carried out as part of the mandate of the Centre for Effective Design of Structures (CEDs) at McMaster University and is partially funded by the Ontario Ministry

of Economic Development and Innovation and by the Natural Sciences and Engineering Research Council of Canada (NSERC).

### **6.11 References**

- [1] Kelly JM. Seismic isolation systems for developing countries. *Earthquake Spectra* 2002;18(3):385–406.
- [2] Toopchi-Nezhad H, Tait MJ, Drysdale RG. Lateral response evaluation of fiber-reinforced neoprene seismic isolators utilized in an unbonded application. *Journal of Structural Engineering* 2008;134(10):1627-1637.
- [3] Toopchi-Nezhad H, Tait MJ, Drysdale RG. Shake table study on an ordinary low-rise building seismically isolated with SU-FREIs (stable unbonded-fiber reinforced elastomeric isolators). *Earthquake Engineering and Structural Dynamics* 2009; 38(11):1335-1357.
- [4] Osgooei PM, Tait MJ, Konstantinidis D. Computational model for unbonded fiber-reinforced elastomeric isolators (U-FREIs). *Earthquake Engineering and Structural Dynamics*. Submitted Manuscript.
- [5] Toopchi-Nezhad H, Tait MJ, Drysdale RG. Bonded versus unbonded strip fiber reinforced elastomeric isolators: finite element analysis. *Composite Structures* 2011;93(2):850-859.
- [6] Kelly JM. Analysis of fiber-reinforced elastomeric isolators. *J Seismol Earthq Eng* 1999;2(1):19–34.

- [7] Computers and Structures Inc. (2013). SAP2000: Static and Dynamic Finite Element Analysis of Structures (Version 16.0.0) Analysis Reference Manual, Computers and Structures, Inc., Berkeley.
- [8] Toopchi-Nezhad H, Tait MJ, Drysdale RG. Testing and modeling of square carbon fiber-reinforced elastomeric seismic isolators. *Structural Control and Health Monitoring* 2007;15(6): 876-900.
- [9] Osgooei PM, Tait MJ, Konstantinidis D. Finite Element analysis of unbonded square fiber-reinforced elastomeric isolators (FREIs) under lateral loading in different directions. *Composite Structures* 2014, 113:164-173.
- [10] Kelly JM, Takhirov SM. Analytical and experimental study of fiber-reinforced strip isolators. PEER Report 2002/11, Pacific Earthquake Engineering Research Center, University of California, Berkeley, 2002.
- [11] National Building Code of Canada. Institute for Research in Construction, National Research Council of Canada, Ottawa, 2010.
- [12] Design of concrete structures, Canadian Standards Association, CSA-A23.3. 2004.
- [13] Osgooei PM, Van Engelen NC, Konstantinidis D, Tait MJ. Experimental and finite element study on the lateral response of modified rectangular fiber-reinforced elastomeric isolators (MR-FREIs). *Engineering Structures*, Submitted Manuscript. Ref. No. ENGSTRUCT-S-14-00976.
- [14] Toopchi-Nezhad H, Tait MJ, Drysdale RG. Simplified analysis of a low-rise building seismically isolated with stable unbonded fiber reinforced elastomeric isolators. *Canadian Journal of Civil Engineering* 2009;36:1182-1194.

- [15] Toopchi-Nezhad H, Tait MJ, Drysdale RG. A novel elastomeric base isolation system for seismic mitigation of low-rise buildings. In: Proceedings of the 14<sup>th</sup> world conference on earthquake engineering. Beijing, 12–18 October 2008.
- [16] Love JS, Tait MJ, Toopchi-Nezhad H. A hybrid structural control system using a tuned liquid damper to reduce the wind induced motion of a base isolated structure. *Engineering Structures* 2011;33(3):738-746.
- [17] Popovics S. A numerical approach to the complete stress-strain curve of concrete. *Cement and Concrete Res.* 1974; 3(5):583-599.
- [18] Takeda T, Sozen MA, Nielsen NN. Reinforced concrete response to simulated earthquakes. *J. Struct. Div., ASCE* 1970; 96(12):2557-2573.
- [19] Minimum design loads for buildings and other structures. *ASCE/SEI 7-10*, American Society of Civil Engineers, ASCE, New York, 2010.
- [20] Baker JW, Lin T, Shahi SK. New ground motion selection procedures and selected motions for the PEER transportation research program. PEER Report 2011/03, Pacific Earthquake Engineering Research Center, University of California, Berkeley; 2011.

Table 6.1. Effective stiffness and damping ratio of the rectangular FREIs.

$u/t_r$	$K_{\text{eff}} \times (t_r/GA)$		$\beta_{\text{eff}} (\%)$	
	x-direction	y-direction	x-direction	y-direction
0.25	0.989	0.853	12.0	13.2
0.50	0.792	0.651	11.9	14.0
0.75	0.662	0.510	10.9	13.6
1.00	0.578	0.416	10.3	13.7
1.50	0.490	0.310	10.4	14.8
2.00	0.537	0.350	8.6	11.8
2.50	0.547	0.374	8.6	11.1

Table 6.2. Energy dissipation of FREIs along the  $x$  and  $y$  directions.

$u/t_r$	$E_h/(GA t_r)$	
	x-direction	y-direction
0.25	0.057	0.054
0.50	0.182	0.177
0.75	0.314	0.302
1.00	0.463	0.442
1.50	0.884	0.801
2.00	1.430	1.285
2.50	2.270	2.007

Table 6.3. Parameters of the Pivot-Elastic model.

Direction	$K_1$ $\times (t_r$ $/GA)$	$K_2$ $\times (t_r$ $/GA)$	$u_y/t_r$	$a_1$ $\times (t_r$ $/GA)$	$a_2$ $\times (t_r^3$ $/GA)$	$a_3$ $\times (t_r^5$ $/GA)$	$a_4$ $\times (t_r^7$ $/GA)$
$x$	1.265	0.249	0.080	4.269e-1	-2.511e-1	7.946e-2	-6.956e-3
$y$	1.000	0.128	0.125	3.507e-1	-2.431e-1	7.495e-2	-6.383e-3

Table 6.4. The ratio of the predicted response values of the FREIs using Pivot-Elastic model over the experimentally observed values.

$u/t_r$	$K_{\text{eff}}^{\text{model}}/K_{\text{eff}}^{\text{exp}}$		$\beta_{\text{eff}}^{\text{model}}/\beta_{\text{eff}}^{\text{exp}}$	
	x-direction	y-direction	x-direction	y-direction
0.25	1.00	1.05	1.02	0.92
0.50	0.99	0.98	0.95	0.98
0.75	1.01	1.00	0.98	1.01
1.00	1.00	0.99	1.05	1.04
1.50	1.00	1.00	1.05	1.01
2.00	1.00	1.00	1.04	0.97
2.50	1.00	1.00	0.96	0.92

Table 6.5. The selected ground motions.

Record	Earthquake	Year	Station	Magnitude	Distance (km)
FN-6	Imperial Valley-06	1979	Calipatria Fire Station	6.5	24.6
FN-8	Chi-Chi, Taiwan	1999	NST	7.6	38.4
FN-13	Chi-Chi, Taiwan	1999	TCU060	7.6	8.5
FN-23	San Fernando	1971	LA – Hollywood Stor FF	6.6	22.8
FP-4	Imperial Valley-06	1979	Delta	6.5	22.0
FP-8	Chi-Chi, Taiwan	1999	NST	7.6	38.4
FP-15	Loma Prieta	1989	Fremont – Emerson Court	6.9	39.9
FP-23	San Fernando	1971	LA – Hollywood Stor FF	6.6	22.8
FP-25	Loma Prieta	1989	Hollister – South & Pine	6.9	27.9
FP-32	Loma Prieta	1989	Saratoga – Aloha Ave	6.9	8.5

Table 6.6. Summary of peak response values for the FB and BI structures.

		Roof Acceleration (g)				Total IDR (%)				Normalized Base Shear			
		Min	Max	Mean	SD	Min	Max	Mean	SD	Min	Max	Mean	SD
MCE	FB	0.49	0.90	0.76	0.12	0.28	1.26	0.62	0.28	0.31	0.76	0.58	0.12
	BI	0.10	0.47	0.23	0.14	0.03	0.31	0.12	0.11	0.09	0.38	0.20	0.11
	Red. (%)			70				81				66	
DBE	FB	0.39	0.76	0.62	0.12	0.21	0.57	0.40	0.11	0.26	0.59	0.46	0.10
	BI	0.08	0.19	0.14	0.04	0.02	0.08	0.05	0.02	0.07	0.17	0.12	0.03
	Red. (%)			77				88				74	
SLE	FB	0.28	0.59	0.41	0.09	0.12	0.33	0.22	0.07	0.21	0.40	0.29	0.06
	BI	0.06	0.14	0.10	0.03	0.01	0.05	0.03	0.01	0.05	0.13	0.10	0.03
	Red. (%)			75				86				67	

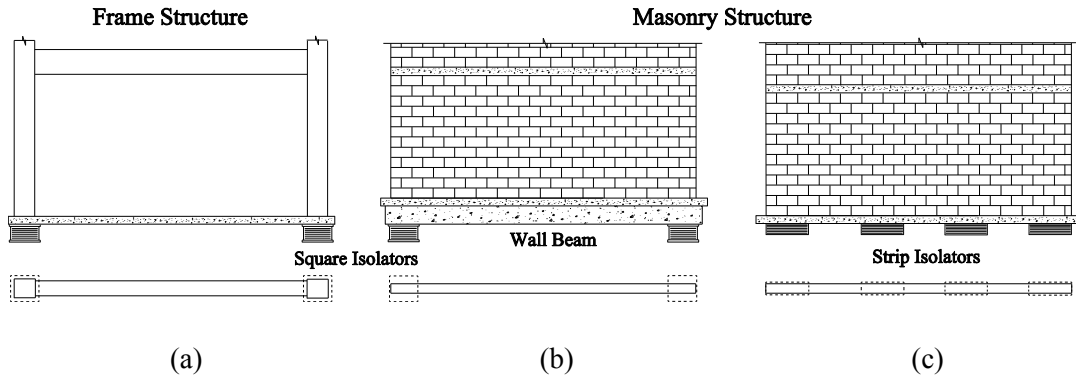


Figure 6.1. Schematic view of seismic isolation of a (a) frame structure; (b) masonry structure using circular/square isolators and (c) masonry structure using rectangular strip isolators

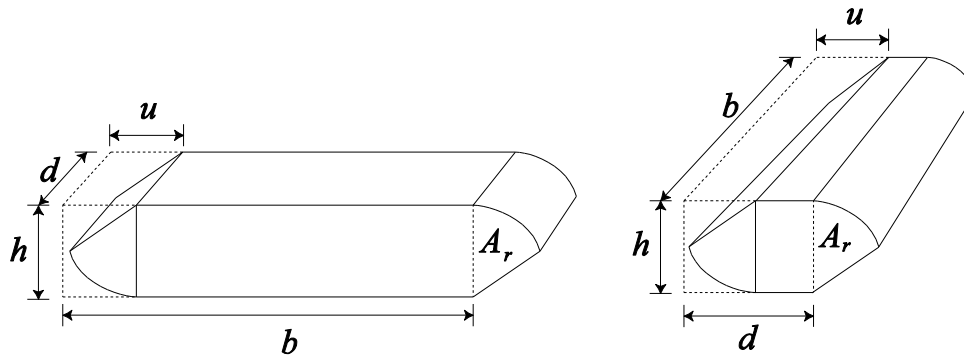


Figure 6.2. Schematic deformed shapes of a rectangular FREI along its longer (left) and shorter (right) directions

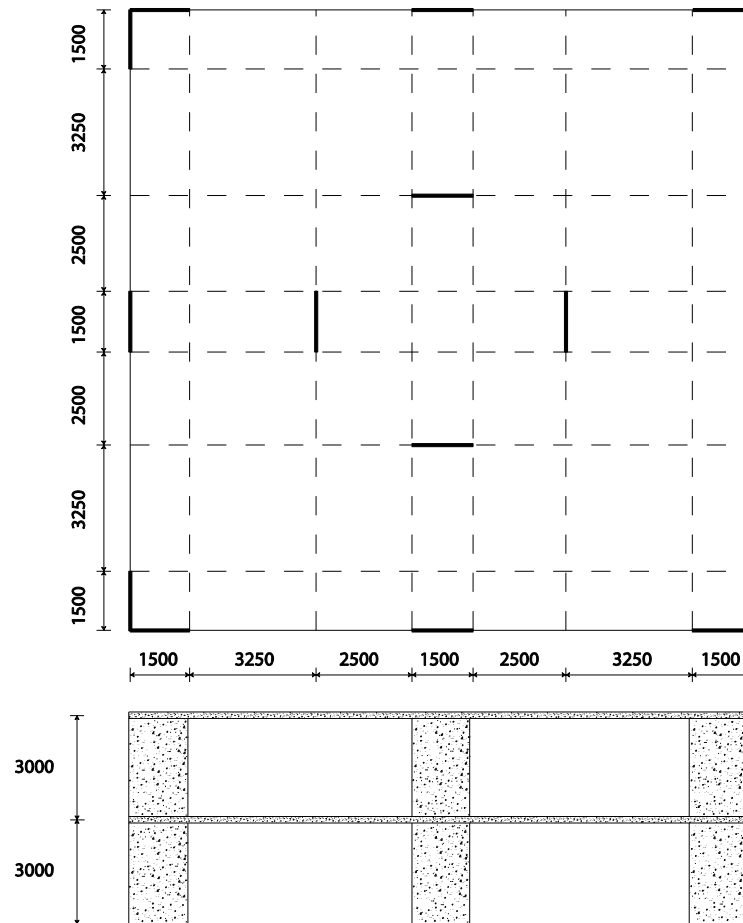


Figure 6.3. Plan and elevation views of the shear wall structure (all dimensions shown are in mm)

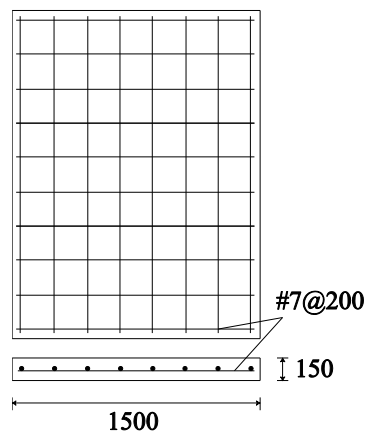


Figure 6.4. Reinforcement detailing of shear walls

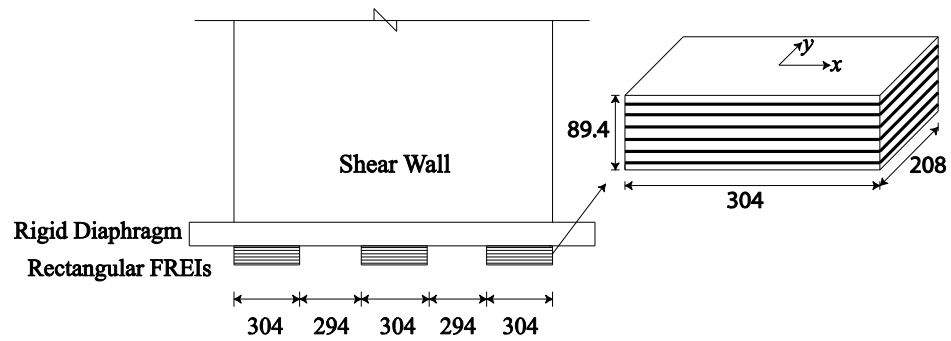


Figure 6.5. Distribution of the isolators under shear walls

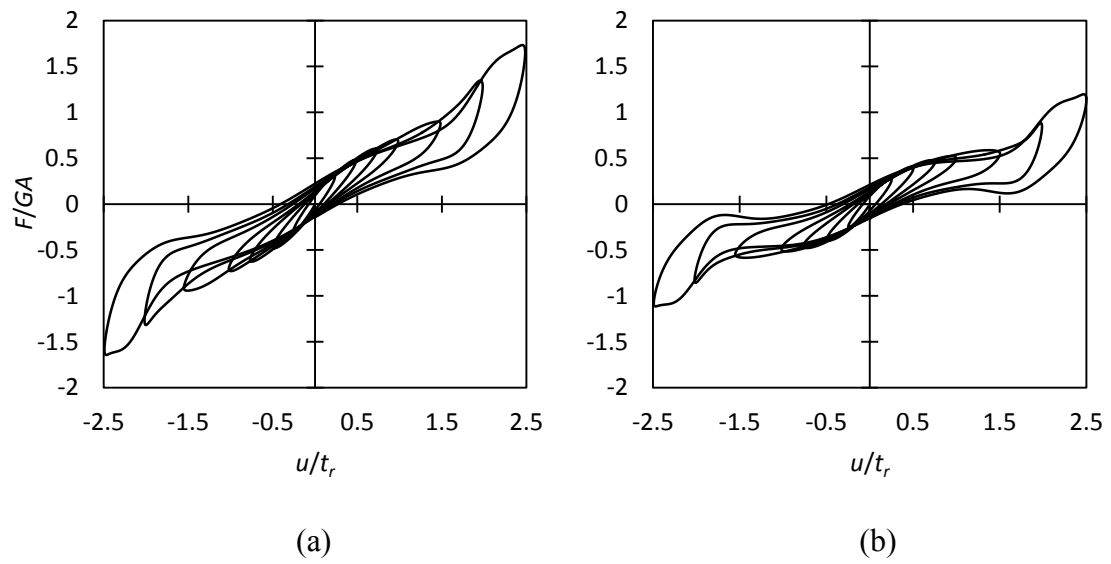


Figure 6.6. Lateral hysteresis loops of the rectangular FREI along (a) x-axis and (b) y-axis

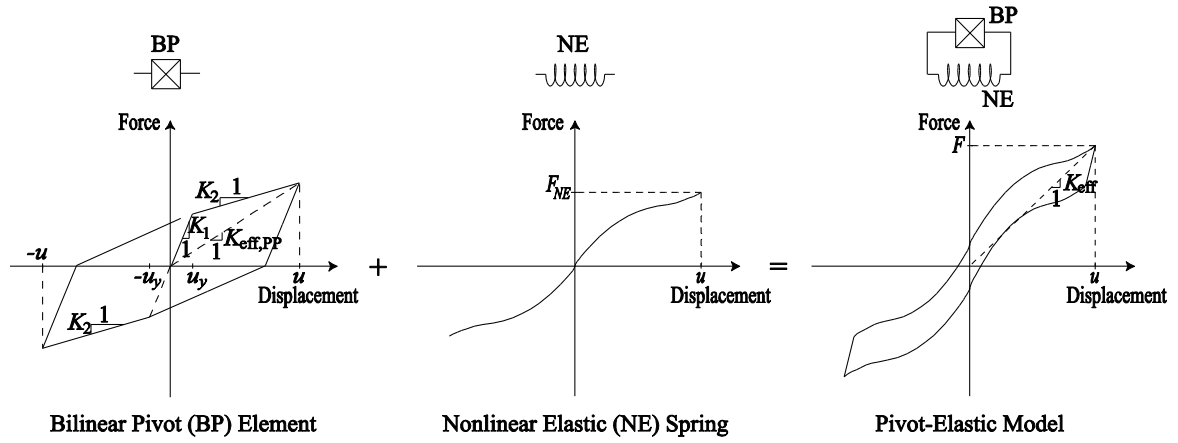


Figure 6.7. Definition of the Pivot-Elastic model

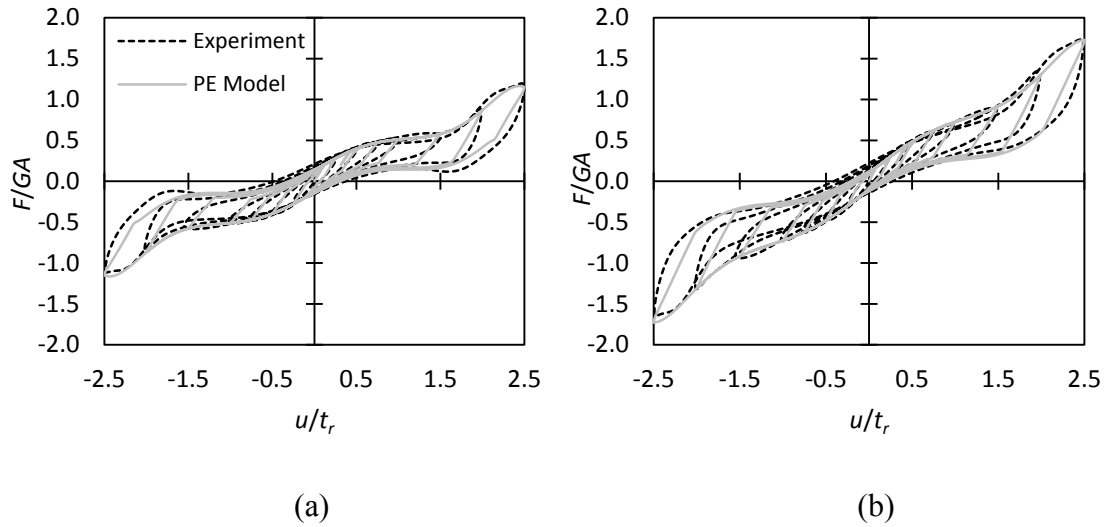


Figure 6.8. Comparison of the experimentally obtained response of the FREIs with the prediction of the Pivot-Elastic model along the (a) x-axis and (b) y-axis

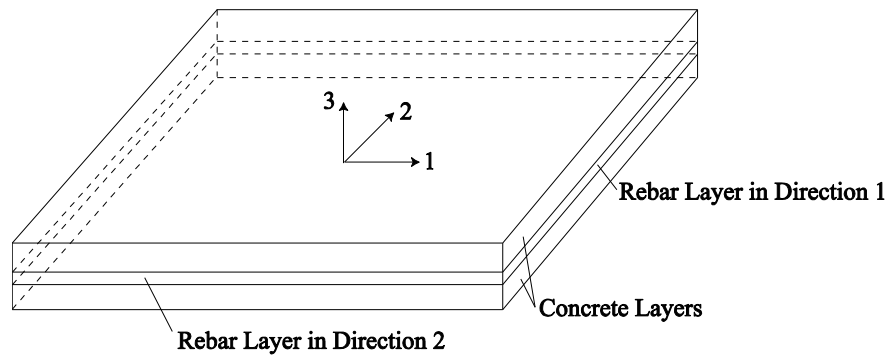


Figure 6.9. Multilayer shell elements

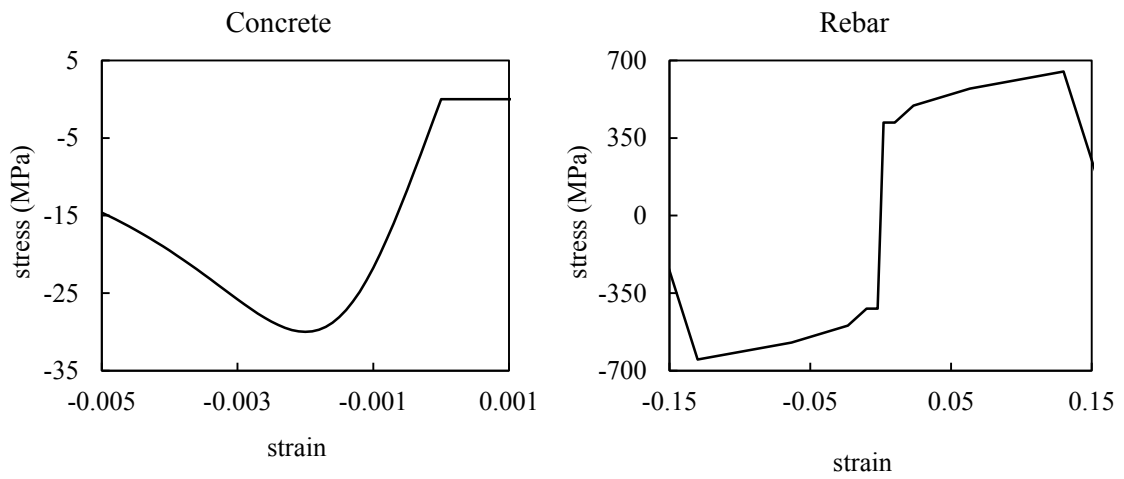


Figure 6.10. Stress-strain relationship of concrete and reinforcement

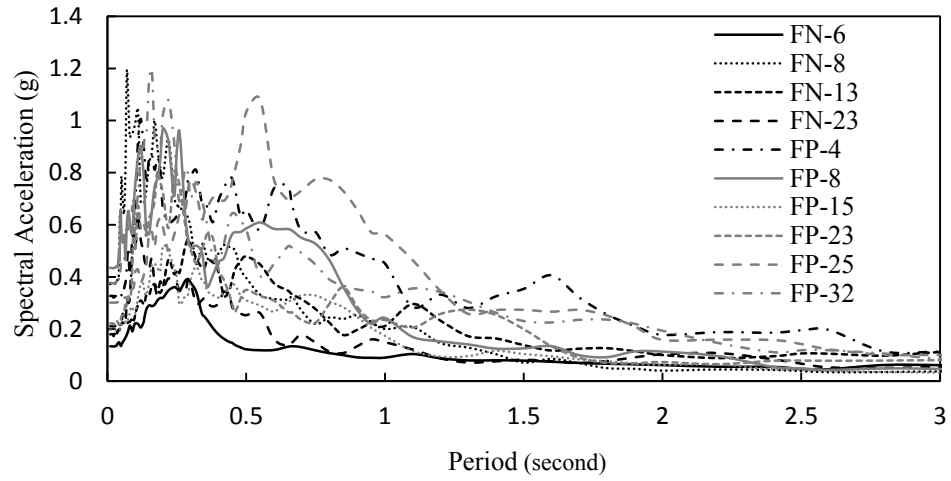


Figure 6.11. Acceleration response spectrum of the selected ground motions at 5% damping

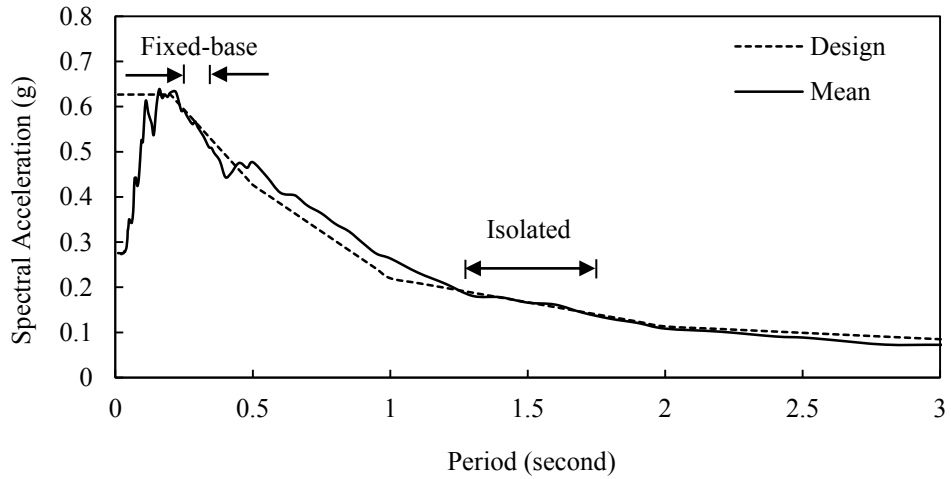


Figure 6.12. Comparison of the mean acceleration response spectrum of the selected ground motions with the design spectrum

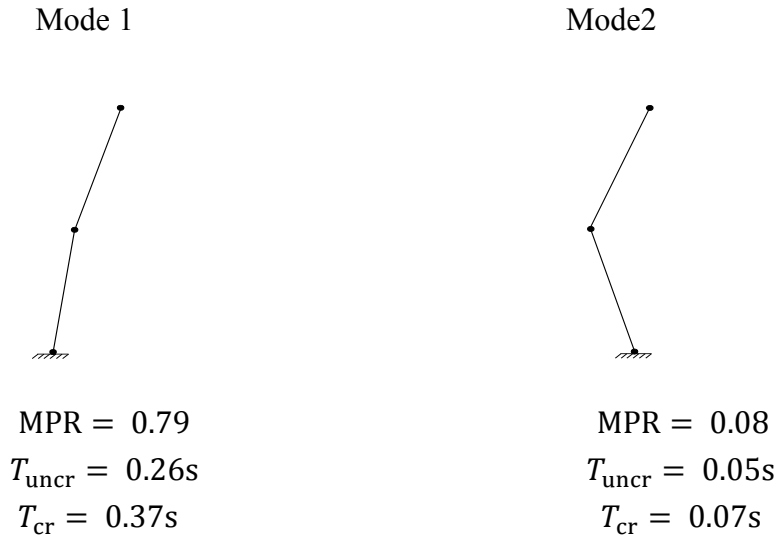


Figure 6.13. First two modes with highest MPR along the direction of ground motions

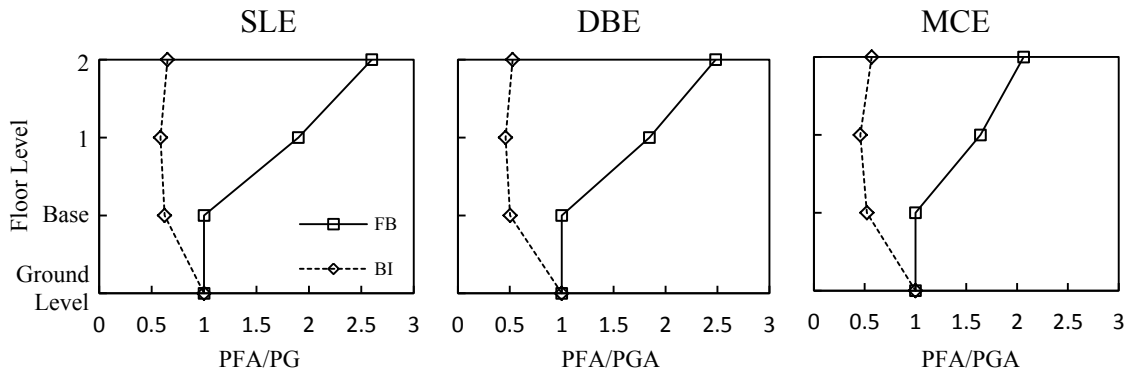


Figure 6.14. Comparison of the mean values of the peak floor accelerations over PGA

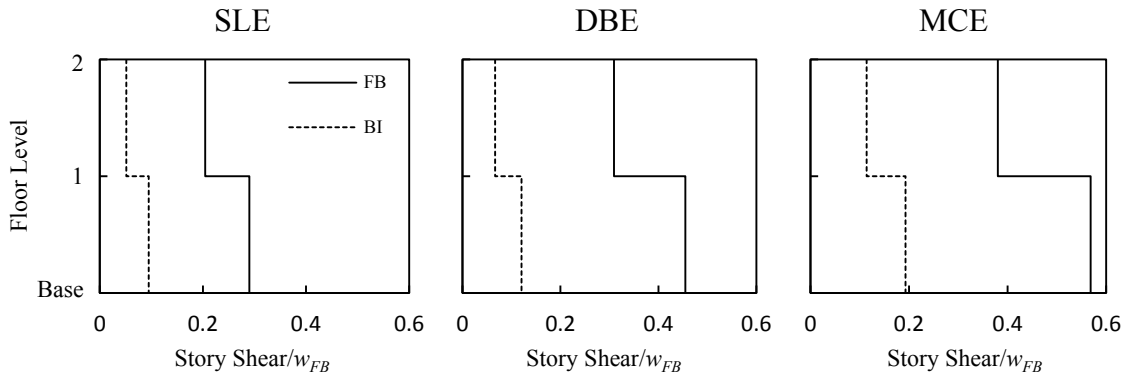


Figure 6.15. Comparison of the mean values of the peak story shear in the FB and BI structures

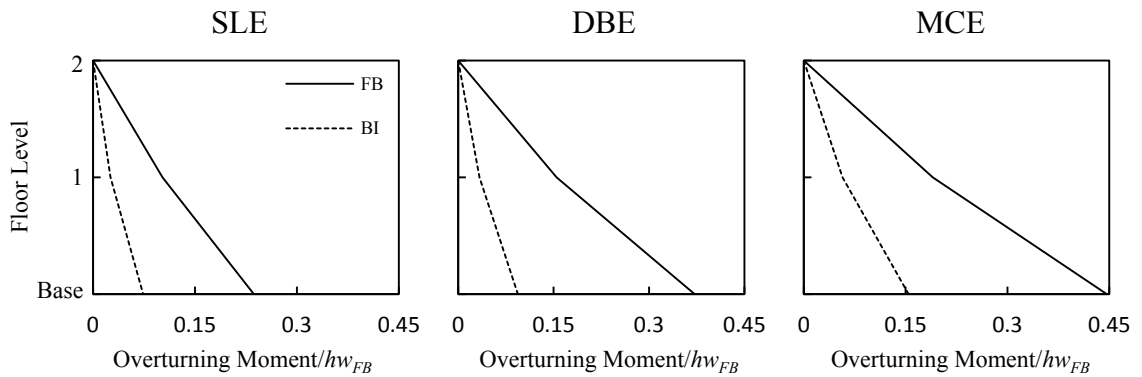


Figure 6.16. Comparison of the mean values of the normalized peak overturning moment in the FB and BI structures

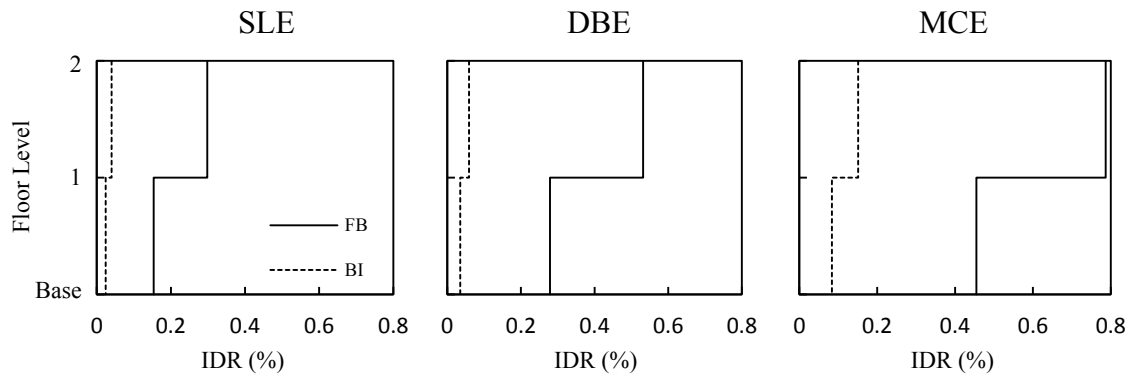


Figure 6.17. Comparison of the mean values of inter-story drift ratios (IDR) in the FB and BI structures

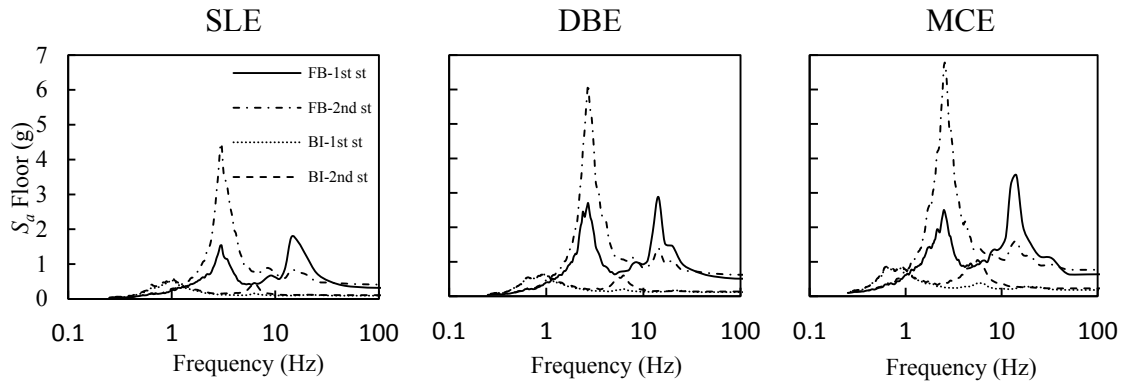


Figure 6.18. Mean floor spectra for the SLE, DBE and MCE hazard levels

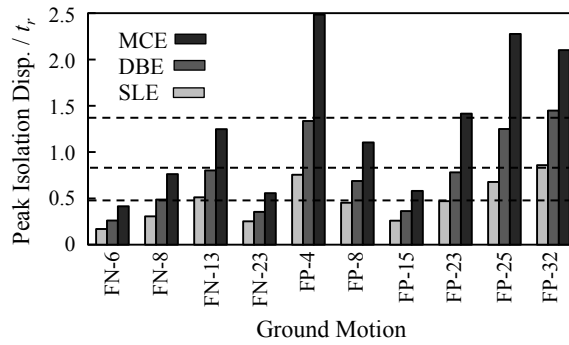


Figure 6.19. Peak isolation displacement obtained at each ground motion

## **Chapter 7: Conclusions and Recommendations**

### **7.1 Summary and Conclusions**

Fiber-reinforced elastomeric isolators (FREIs) are low-weight and potentially low-cost elastomeric bearings that can extend the application of seismic isolation technology into ordinary importance residential or commercial buildings, particularly in developing countries. The feasibility of FREIs has been investigated through a number of experimental studies [1-6] and shown to be effective in reducing the seismic demand on structures [7]. However, more research is required to i) better understand the behaviour of FREIs, and ii) simplify the existing complex design and analysis procedure of these isolators. In this research, numerical analyses were carried out to investigate the vertical and lateral response behaviour of FREIs. In addition, a computational model was proposed to enhance the analysis of structures seismically isolated using FREIs. The proposed model was evaluated using the results of an experimental shake table test program, and was used to conduct a series of time history analyses.

#### **7.1.1 FEA on Vertical Response of FREIs**

3D FEA was carried out to investigate the effect of flexibility of fiber reinforcement layers on the compressive behaviour of FREIs with various shape factor values ( $S$ , defined as the total loaded area of one elastomer layer to the load free area). The values for the in-plane stiffness of fiber reinforcement layers were selected to represent a large variety of applicable materials. The results of FEA were compared with the predictions

of two analytical closed-form solutions: the pressure solution (PS) and the pressure approach (PA). Using FEA results, the simplifying assumptions used in the analytical solutions were evaluated. In addition, the effect of end boundary condition and the magnitude of applied compression load, which are usually neglected in the derivations of closed-form solutions, on the response of isolators were studied. The following conclusions were drawn:

- In overall, both analytical methods predicted the compression stiffness of FREIs with acceptable accuracy. The most accurate predictions came from the PA method considering the end boundary condition.
- The two kinematic assumptions used in the PS and PA methods were found to be valid for FREIs with various reinforcing materials.
- For FREIs with a reinforcing material with relatively high in-plane stiffness, ignoring the end boundary condition has negligible effect on the compression behaviour. As the in-plane stiffness of reinforcing material decreases, the sensitivity of the response to the effect of end boundary increases.
- The compression behaviour of FREIs with  $S \geq 20$  was found to have negligible sensitivity to an increase in the vertical compression load, while isolators with  $S = 5$  and  $S = 10$  showed a stiffening behaviour with an increase in the compression load.

### 7.1.2 FEA on Lateral Response of FREIs

The lateral response of FREIs is complex and in the absence of sophisticated closed-form solutions, FEA can be employed to predict the lateral response of this type of isolators with various geometric shapes and under different loading conditions. 3D FEA was carried out on square FREIs with different height-to-width ratios. The finite element (FE) models were evaluated using the experimental test results. The FE models were subsequently used to investigate the lateral response of the isolators under loading direction angles of  $0^\circ$ ,  $15^\circ$ ,  $30^\circ$  and  $45^\circ$  with the direction of the isolator. The major findings of this study were:

- In general, the effective stiffness of the FREIs increases as the loading directions changes from  $0^\circ$  to  $45^\circ$ .
- As the loading direction changes from  $0^\circ$  to  $45^\circ$ , the displacement at which the hardening behaviour of FREIs occurs increases.
- As the width-to-height ratio of the isolators decreases, the sensitivity of the response of isolators to the loading direction decreases.
- An isolator with a width-to-height ratio of 1.9 showed an unstable response along  $0^\circ$  and  $15^\circ$  directions, while at  $30^\circ$  and  $45^\circ$  a stable response was observed.
- The stress distribution in the elastomer layers along the height of the isolators is affected by the change in the loading direction. Changing the loading direction from  $0^\circ$  to  $45^\circ$  results in an increase in the peak absolute values of normal stresses in the center elastomer layer, and a decrease in the

peak absolute values of normal stresses in the top and bottom elastomer layers.

### **7.1.3 Computational Model for FREIs**

The Pivot-Elastic, a new computational model is developed for the lateral response of FREIs to enhance the design and analysis of isolation systems composed of this type of isolators. In contrast to the existing models, conducting time history analysis of structures seismically isolated with FREIs using the proposed model does not require a customized developed code and is not iterative. In addition, effective stiffness values predicted using closed-form solutions or FEA can be used to determine the parameters of the proposed model, which makes it suitable for preliminary design purposes. The proposed model was used to conduct time history analyses and the accuracy of the results was evaluated using the results of a previous shake table study. The major conclusions are:

- The Pivot-Elastic model can capture the variation of in the values of the effective stiffness and damping ratio of FREIs.
- The model can be used to predict the lateral response of isolators employed in both bonded and unbonded applications.
- The proposed model simplifies the analysis of structures seismically isolated with FREIs and provides accurate predictions.

#### **7.1.4 Experimental and FEA studies on Rectangular FREIs**

The lateral response of rectangular shaped FREIs is investigated through experimental testing and 3D FEA. The concept of introducing geometric modifications to increase the efficiency of FREIs is studied. The FE models were evaluated using experimental test results and were employed to conduct a parametric study considering a wide range of modification configurations. The long rectangular shape of isolators can provide a more uniform distribution of gravity loads. In addition, modifications can be introduced into the isolators to overcome the potential short-coming of increasing the effective stiffness of the isolation system due to the increase in the number and length of individual isolators. Major findings include:

- The modified FREIs exhibit the softening and subsequent stiffening response associated with FREIs.
- Introducing a modification results in a reduction in the effective stiffness values of the isolator. The larger the modification diameter, higher reduction in the stiffness values.
- Despite having the same area removed from the isolator, FREIs with interior modifications had lower effective stiffness values. An interior modification with 11.4% reduction in the total plan area results in almost a 40% reduction in effective stiffness.

#### **7.1.5 Seismic Isolation of a Shear Wall Building with FREIs**

The results of the experimental test program carried out on rectangular FREIs (Chapter 5) along with the proposed Pivot-Elastic model (Chapter 4) were used to

conduct a series of time history analyses on a two storey reinforced concrete shear wall building. The seismic response of the structure was investigated under a set of ten earthquake ground motions, and at three hazard levels. The isolation system was composed of 48 rectangular FREIs, where three isolators were placed underneath each shear wall. Comparing the seismic response of the fixed-base and base-isolated structures showed that using FREIs significantly reduced the seismic demand on the structure. The major findings of this study are:

- The Pivot-Elastic model can be used to predict the lateral response of rectangular FREIs both along the length and the width of the isolators.
- Long rectangular-shaped FREIs can be used as a potential cost-effective and easy to apply seismic isolation system for concrete or masonry shear wall structures.
- The superstructure base shear and the total inter-storey drift ratio of the fixed-base structure were decreased in average by 74% and 88% in the isolated structure for the design-based earthquake level.

## **7.2 Recommendations for Future Study**

- In the experimental tests carried out in Chapter 5, the effect of lateral displacement on the compression behaviour of FREIs has been neglected. However, a reduction in the compression modulus of FREIs is expected under lateral displacements due to the rollover deformation. Further study on

the effect of lateral displacement on the compression behaviour of FREIs is required.

- An experimental study on the corresponding full-scale FREIs of the tested 1/4 rectangular isolators would provide useful information on the effect of scaling on the response of FREIs.
- In this study, the response of FREIs was obtained from one-directional cyclic testing. Conducting bi-directional testing on the isolators is recommended as it provides a better understanding of the response of FREIs under real-time earthquake events.
- The existing analytical closed-form solutions for the lateral response of FREIs [8-10] neglect the effects of the direction of loading and the magnitude of vertical compression load on the lateral response of isolators. However, in Chapter 3 it was observed that the lateral response of FREIs depends on the loading direction. Previous test results [11] confirm the sensitivity of the lateral response of FREIs to the magnitude of vertical load. An analytical closed-form solution that takes into account the loading direction and considers the effect of vertical compression load should be developed.
- In Chapter 6, the efficiency of rectangular FREIs as a potential cost-effective seismic isolation system for a concrete or masonry shear wall structure was investigated through numerical analysis. A shake table experimental study on a shear wall structure seismically isolated using rectangular FREIs is required to better show the feasibility and viability of this type of isolators.

### **7.3 References**

- [1] Kelly JM. Seismic isolation systems for developing countries. *Earthquake Spectra* 2002; 18(3):385–406.
- [2] Moon BY, Kang GJ, Kang BS, Kim GS, Kelly JM. Mechanical properties of seismic isolation system with fiber-reinforced bearing of strip type. *International Applied Mechanics* 2003; 39(10):1231–9.
- [3] Toopchi-Nezhad H, Tait MJ, Drysdale RG. Testing and modeling of square carbon fiber-reinforced elastomeric seismic isolators. *Structural Control and Health Monitoring* 2007;15(6):876–900.
- [4] Mordini A, Strauss A. An innovative earthquake isolation system using fibre reinforced rubber bearings. *Journal of Engineering Structures* 2008; 30(10):2739–51.
- [5] Toopchi-Nezhad H, Tait MJ, Drysdale RG. Lateral response evaluation of fiber-reinforced neoprene seismic isolators utilized in an unbonded application. *Journal of Structural Engineering* 2008; 134(10):1627–37.
- [6] Russo G, Pauletta M, Cortesia A. A study on experimental shear behavior of fiber reinforced elastomeric isolators with various fiber layouts, elastomers and aging condition. *Engineering Structures* 2013; 52:422-433.
- [7] Toopchi-Nezhad H, Tait MJ, Drysdale RG. Shake table study on an ordinary low-rise building seismically isolated with SU-FREIs (stable unbonded fiber reinforced elastomeric isolators). *Earthquake Engineering and Structural Dynamics* 2009; 38:1335–57.

- [8] Van Engelen N, Tait MJ, Konstantinidis D. A model of the shear behaviour of unbonded fiber reinforced elastomeric isolators (FREIs) including rollover. *Journal of Structural Engineering* 2014; (in press).
- [9] Peng TB, Zhang H, Li JZ, Li WX. Pilot study on the horizontal shear behaviour of FRP rubber isolators. *Journal of Vibration and Shock* 2009; 28(1):127–130. In Chinese.
- [10] Toopchi-Nezhad H. Horizontal stiffness solutions for unbonded fiber reinforced elastomeric bearings. *Structural Engineering and Mechanics* 2014; 49(3):395-410.
- [11] De Raaf MGP, Tait MJ, Toopchi-Nezhad H. Stability of fiber-reinforced elastomeric bearings in an unbonded application. *Journal of Composite Materials* 2011; 45(18):1873-1884.